

# Optimisation of a Testbeam Setup and Background Estimates for Detectors at the ILC using Monte Carlo Simulations

Diplomarbeit  
zur Erlangung des akademischen Grades  
Diplom-Physiker

eingereicht von  
Ringo Sebastian Schmidt  
geboren am 5. Dezember 1977 in Finsterwalde

**Brandenburgische Technische Universität Cottbus**

Fakultät 1: Mathematik, Naturwissenschaften und Informatik  
Institut für Physik und Chemie

Gutachter: Prof. Dr. Jürgen Reif  
Dr. Wolfgang Lohmann

Zeuthen den 7. August 2007

# Selbständigkeitserklärung

Hiermit erkläre ich, die vorliegende Arbeit selbständig und nur unter Verwendung der angegebenen Quellen und Hilfsmittel angefertigt zu haben.

Die dem Verfahren zugrunde liegende Prüfungsordnung für den Studiengang Physik an der Fakultät I – Mathematik, Naturwissenschaften und Informatik der Brandenburgischen Technischen Universität Cottbus habe ich gelesen.

Zeuthen, den 07.08.2007

Ringo Schmidt

# Contents

Abbreviations	v
Symbols	vii
<b>1 Introduction</b>	<b>1</b>
<b>2 ILC Physics and Detector</b>	<b>5</b>
2.1 Physics Case of the ILC	5
2.1.1 Higgs Boson Production	5
2.1.2 Supersymmetry	6
2.1.3 More Physics beyond the Standard Model	7
2.2 Technical Challenges for the ILC	7
2.2.1 The Accelerator	7
2.2.2 ILC Luminosity	8
2.2.3 Pinch Effect	9
2.2.4 Beamstrahlung Pairs	10
2.3 A Detector for the ILC	11
2.3.1 Complex Detectors for High Energy Physics	11
2.3.2 The Large Detector Concept	12
2.3.3 Vertex Detector and Tracker System	13
2.3.4 Calorimeters	14
2.3.5 Forward Calorimeters	15
2.4 Machine Detector Interface	18
2.4.1 Beamstrahlung-induced Background	18
2.4.2 LDC Geometry and Beam Options	19
<b>3 Testbeam Studies</b>	<b>23</b>
3.1 Testbeam Setup and Simulation	23
3.2 Optimisation of the Geometry	25
3.3 Measurement Accuracy	28
3.4 Energy Deposition	31
3.4.1 pCVD Diamonds	31
3.4.2 Silicon	32

3.5	Results of the Testbeam . . . . .	32
<b>4</b>	<b>Background in the Silicon Tracking Detectors of the LDC</b>	<b>33</b>
4.1	Simulation of the Pair Background . . . . .	33
4.1.1	Simulation of Bunch Crossings – GUINEA-PIG . . . . .	33
4.1.2	Full Detector Simulation – MOKKA . . . . .	34
4.1.3	Analysis and Reconstruction – MARLIN . . . . .	34
4.2	Analysis of the Simulated Event Samples . . . . .	34
4.2.1	The Vertex Detector . . . . .	35
4.2.2	The Silicon Intermediate Tracker . . . . .	42
4.2.3	The Forward Tracking Discs . . . . .	48
<b>5</b>	<b>Comparison of Different Options and Optimisation of the Design</b>	<b>55</b>
5.1	Beam Crossing Angle and Magnetic Field . . . . .	56
5.1.1	Background in the VXD and the SIT . . . . .	56
5.1.2	Background in the FTD . . . . .	60
5.2	Beam Parameter Sets . . . . .	60
5.2.1	Background in the VXD and the SIT . . . . .	60
5.2.2	Background in the FTD . . . . .	65
5.3	Design of the Mask and the Graphite Absorber . . . . .	65
<b>6</b>	<b>Conclusions</b>	<b>69</b>
	<b>References</b>	<b>71</b>

# Abbreviations

anti-DID	Anti-DID option – Magnetic field lines are aligned with the outgoing beams.
BDS	Beam Delivery System
BeamCal	Beam Calorimeter
BH	Bethe-Heitler process, $\gamma e \rightarrow ee^+e^-$
BW	Breit-Wheeler process, $\gamma\gamma \rightarrow e^+e^-$
BX	Bunch crossing
CERN	Conseil Européen pour la Recherche Nucléaire – European Organisation for Nuclear Research.
CPC	Coherent Pair Creation
CVD	Chemical Vapour Deposition
DALINAC	Darmstadt Linear Accelerator
DESY	Deutsches Elektronen-Synchrotron
DID	Detector-integrated Dipole – The DID option modifies the solenoidal magnetic field aligning the field lines with the incoming beams.
ECAL	Electromagnetic Calorimeter
ECFA	European Committee for Future Accelerators
EUROTeV	European Design Study Towards a Global TeV Linear Collider
FTD	Forward Tracking Discs
GEANT	Geometry and Tracking
GEM	Gaseous Electron Multiplier
GUT	Grand Unified Theory
HCAL	Hadronic Calorimeter
HERA	Hadron-Elektron-Ring-Anlage
ICFA	International Committee for Future Accelerators
IEEE	Institute of Electrical and Electronics Engineers, Inc.
ILC	International Linear Collider
IP	Interaction Point
IPC	Incoherent Pair Creation
JLC	Japan Linear Collider
KEK	High Energy Accelerator Research Organization, Japan
LC	Linear Collider
LCIO	Linear Collider Input/Output

LDC	Large Detector Concept
LEP	Large Electron Positron Collider
LHC	Large Hadron Collider
LL	Landau-Lifshitz process, $ee \rightarrow eee^+e^-$
<i>Low P</i>	Low Power beam parameter set for the ILC
LumiCal	Luminosity Calorimeter
MARLIN	Modular Analysis and Reconstruction for the Linear Collider
MDI	Machine Detector Interface
MIP	Minimal Ionising Particle
NLC	Next Linear Collider
pCVD	Polycrystalline CVD
QUAD	Final focussing quadrupole magnet of the beam delivery system
PFA	Particle Flow Analysis
R&D	Research and Development
RPC	Resistive Plate Chamber
SiPM	Silicon Photo-Multiplier
SIT	Silicon Intermediate Tracker
SQL	Structured Query Language
TESLA	Tera-Electronvolts Superconducting Linear Accelerator
TPC	Time Projection Chamber
TU	Technical University
VXD	Vertex Detector
WWS	Worldwide Study

# Symbols

$A$	Area, $\text{m}^2$
$c$	Speed of light, $c = 299792458 \text{ m s}^{-1}$
$D$	Absorbed radiation dose, Gy
$d$	Distance in general, m
$E$	Energy, eV
$E_{\text{CM}}$	Center-of-mass energy, eV
$E_{\text{dep}}$	Energy deposit, eV
$e^-, e^+$	Electron and positron, respectively
$f, \bar{f}$	Fermion and antifermion, respectively
$f_{\text{b}}$	Number of bunch crossings per time interval, $\text{s}^{-1}$
$f_{\text{rep}}$	Repetition rate for trains (pulses) at the ILC, Hz
$H$	Higgs boson
$H_{\text{D}}$	Luminosity enhancement factor
$i$	Running index
$K$	Scaling factor for spectra of energies deposited in silicon with enhanced mass density
$\mathcal{L}$	Luminosity, $\text{cm}^{-2} \text{ s}^{-1}$
$L$	Time-integrated luminosity, $\text{b}^{-1}$
$l$	Length in general, m
$L^*$	Focal length of the final quadrupole magnet, $L^* = 4.05 \text{ m}$
$m$	Mass in general, kg
$N$	Number of events (for a certain process)
$n$	Number of particles in a bunch
$n_{\text{b}}$	Number of electron/positron bunches per train at the ILC
$p_{\text{t}}$	Component of the momentum transverse to the beam direction, $\text{eV}/c$
$Q$	Electric charge (number of generated charges for both signs), As
$R$	Correction factor for the Faraday cup current, accounts for scattering effects
$r$	Cylindrical coordinate in the LDC detector, defined as $r = \sqrt{x^2 + y^2}$ , m
$s$	Squared center-of-mass energy, $\sqrt{s} = E_{\text{CM}}$
$t$	Time in general, s
$u$	Circumference of components in the LDC detector, $u = 2\pi r$ , m
$V$	Volume in general, $\text{m}^3$
$W$	Charged heavy gauge boson

$x$	Cartesian coordinate in the LDC detector, m
$X_0$	Radiation length of a material, m
$y$	Cartesian coordinate in the LDC detector, m
$Z$	Neutral heavy gauge boson
$z$	Cartesian and cylindrical coordinate, respectively, in the LDC detector, m

### Greek letters

$\beta$	Velocity measured in units of the speed of light, $c$
$\gamma$	Photon (particle); Relativistic factor, defined as $\gamma = \frac{1}{\sqrt{1-\beta^2}}$
$\delta$	Charge collection distance, m
$\theta$	Polar angle in the LDC detector with respect to the outgoing beam, rad
$\vartheta$	Polar angle (codeclination) in the LDC detector with respect to the detector's $z$ axis, rad
$\theta_x$	Crossing angle of the beams, rad
$\mu^-, \mu^+$	Muon and antimuon, respectively
$\nu$	Neutrino
$\rho$	Mass density, $\text{g cm}^{-3}$
$\sigma$	Interaction cross section, $1 \text{ barn} = 1 \text{ b} = 10^{-28} \text{ m}^2$
$\sigma_{x,y,z}$	$x$ , $y$ and $z$ dimensions of the electron and positron bunches, m
$\Upsilon$	Beamstrahlung parameter
$\varphi$	Azimuth angle in cylindrical coordinates of the LDC detector, defined as $\varphi = \arctan \frac{y}{x}$ , taking into account the sign according to the quadrant, rad

# Chapter 1

## Introduction

Science is not only the search for answers but also a search for questions. The demand on scientists, requiring a certain knowledge, is to come into the ability to reveal such questions. Once formulated, they will guide us to possible answers—may it be performing experiments or devising theoretical structures. Most probably this will result in new questions. However, this is the course, and raising a challenging problem, after all, is a sign of having a slight clue of the embracing complexity that is ready to be investigated.

These days, there are such fundamental questions in physics unfold. Why are there, for example, three generations of elementary particles, covering a range of masses from below electron volt for neutrinos up to 175 GeV for the top quark? What is the nature of dark matter and dark energy? Why do we see only matter but no antimatter?

To explore the microscopic world of the fundamental particles at space-time scales far away from daily experience, we need macroscopic detectors. Large particle accelerators have been built, generating high energy particle beams, for example in order to create new particles and understand their interactions. Many experiments have been done in the past, and there has been strong progress in developing detector techniques. In the beginning relative simple devices such as cloud chambers were used. Following the request of physics, large multi-purpose detectors were built, which became more and more complex.

Physics in general is based on the interplay of theory and experiment. Starting from accidental observations and presumptions, scientists were trying to develop model descriptions. At this place, I would like to quote Dürrenmatt, who wrote: “It is not a scientist’s task to explain nature but to describe it.” There is no need to demonstrate how an electron looks like in terms of our macroscopic world, because an electron does not look like anything. It owns an energy and a momentum—and since those are not independent of each other they are even components of one physical tag—and due to this microscopic scope, which cannot be treated disregarding quantum mechanics, its entity can only be specified by quantum numbers. For ensembles of several particles, not necessarily interacting with each other, the probability as an additional feature can be found, entering the mathematical field of statistics and leading to properties such as life time or cross section. These efforts should allow to condense empiric experiences to regularities that make the observed phenomena computable. For that purpose the describing model has to be refined unless it

is falsified by experimental results.

At this time we have a theory of particle physics called Standard Model, supported by many precision measurements. However, the Higgs boson, which is responsible for the generation of masses of the fundamental particles, has not been seen yet. Furthermore, the Standard Model cannot explain *all* the effects observed in experiments, e. g. the non-zero neutrino masses or the mechanism of gravity. Hence the Standard Model seems not to be a fundamental theory but needs an extension. The most favourable theoretical proposals predict solutions to many shortcomings to be found in the TeV energy range. Answers from the experiment are expected from the new energy scale accelerators: the Large Hadron Collider (LHC) at CERN and the International Linear Collider. The latter, ILC, is a venture based on the technical preparations of the previous linear collider projects TESLA [1], Next Linear Collider [2], and Japan Linear Collider [3].

The simple access to this new energy range might not suffice. The events of certain processes may have low rates, so that we need a high luminosity in order to determine the properties of new particles and to measure their parameters with high precision. Accelerators and detectors must be conceived, dimensioned and instrumented properly. The accelerators have to deliver beams of the necessary quality and energy. The detectors must be able to register the final state particles and measure and identify them. For that purpose, complex systems are developed, consisting of different types of sub-detectors. New technologies are in consideration for the ILC to cope with the demands of new physics expected.

In addition also background processes have to be considered, because they can disturb the detection of particles and the measurement of their properties. Bending magnets, collimators and the final focus system may lead to background generation. The huge magnetic fields during bunch crossing induce so-called beamstrahlung, a phenomenon becoming important at the ILC due to the small bunch sizes. This background is estimated in advance using Monte Carlo simulations. On the basis of these estimates the detectors will be optimised in their geometry to minimise the amount of background depositions. Furthermore, the level of the remaining background determines the benchmarks to be set on detector parameters such as the readout frequency, the granularity and the radiation hardness.

The work at hand addresses two important aspects of the detector design. First, a testbeam setup has been optimised for the study of the radiation hardness of sensors needed for special sub-detectors in the very forward region of the ILC detector. Monte Carlo simulations have been performed to estimate the depositions in the sensors under test for several setup geometries. Systematic effects in the determination of the absorbed dose caused by scattering effects in the setup material have been evaluated.

Second, for a given design of the ILC, the machine-induced background in the inner tracking detectors originating from beamstrahlung is estimated. These studies have been done for several beam parameter sets and magnetic field configurations under discussion.

Two quantities are of interest for the design of the silicon detectors. The first is the number of hits created by the background per area and time, referred to as occupancy. For an efficient track reconstruction the number of background hits must be kept low. The unpreventable occupancy determines the granularity and the readout frequency of the

detectors.

The second quantity is the radiation dose the silicon sensors absorb due to the background hits. The estimate of this dose for a reasonable operation time of several years determines the required radiation hardness on the sensors and the readout electronics.



# Chapter 2

## ILC Physics and Detector

### 2.1 Physics Case of the ILC

The International Linear Collider is a design proposal for a next generation electron-positron collider with an energy of 500 GeV in the center-of-mass system. In a second phase it will be possible to upgrade it to an energy of 1 TeV. The predecessor, LEP, a circular  $e^+e^-$  collider at CERN, reached a center-of-mass energy of  $E_{\text{CM}} \sim 200$  GeV. Because of the synchrotron radiation the energy of this storage ring was restricted. To tackle the completion and to understand the limits of the Standard Model, for instance the fundamental question of mass generation, higher energies are needed. A linear collider with an energy of  $E_{\text{CM}} \approx 500$  GeV will allow to test many conceivable theories and Standard Model extensions as discussed extensively in the Technical Design Report for TESLA [4]. The major physics challenges are listed below.

The ILC will be complementary to the LHC at CERN, which will collide protons at  $E_{\text{CM}} = 14$  TeV. They can be accelerated circularly to much higher energies than electrons. However, baryons are composed states, with partons carrying only a fraction of the proton energy. Therefore the initial conditions of a process will have high uncertainties. A diversity of particles will be produced in the final state, leading to very complex signatures and a large background. In contrast, the advantage of the ILC is the well-defined underlying initial state of point-like leptons. Interesting quantities such as particle properties can be measured much more precisely from possibly rare but clear events.

#### 2.1.1 Higgs Boson Production

The most dissatisfactory imperfection in the current structure of the Standard Model is the lack of any experimental confirmation for a mechanism that appears to be responsible for the electroweak symmetry breaking. In the theory a scalar field with non-zero vacuum expectation value is introduced, following the proposal of Higgs [5]. Massive particles acquire their masses through interaction with this field. The Higgs boson as an excitation of the gauge field is expected to have a mass in the range of  $114 \text{ GeV} \leq m_H \lesssim 182 \text{ GeV}$ . The lower limit is obtained from the direct searches at LEP [6], which could not detect

the Higgs boson at the highest possible energies. The upper limit is derived from the electroweak radiative contributions to several observables measured precisely at LEP and Tevatron [7].

The center-of-mass energy that is necessary to generate the Higgs boson in  $e^+e^-$  collisions in practice is larger than its mass. For example, in the Higgs-strahlung process,  $e^+e^- \rightarrow ZH$ , a virtual intermediate  $Z$  boson is created, which transfers into a real  $Z$  emitting a neutral Higgs boson, as depicted in Figure 2.1(a). The cross section for Higgs-strahlung is proportional to  $1/s$ , where  $s = E_{\text{CM}}^2$ , and dominates at lower energies. The  $Z$  subsequently decays into fermions, the momenta of which allow the reconstruction of the Higgs boson in the recoil mass in a model-independent way. A final state consisting of a pair of charged leptons, either  $e^+e^-$  or  $\mu^+\mu^-$ , is especially interesting because of its clear signature. However, the branching fraction of the  $Z$  in electrons and muons is about 6%, while most of the decays lead to quark-antiquark states. These are much more difficult to reconstruct as the quarks form jets when hadronising. Also the  $H$  most likely generates jets, hence we will have to reconstruct multi-jet events.

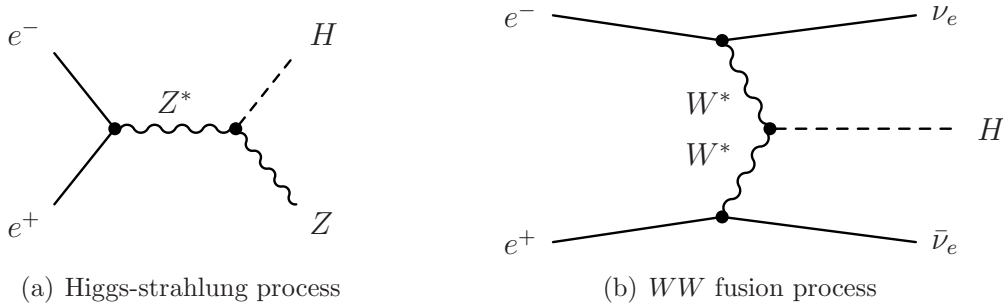


**Figure 2.1:** Main production processes of the Standard Model Higgs boson in electron-positron collisions.

The  $WW$  fusion process in Figure 2.1(b) is more relevant at higher energies as the cross section rises with  $\log(s/m_H^2)$ .

### 2.1.2 Supersymmetry

Other questions are the relationship of the four fundamental forces and dark matter particles, for which strong hints exist. Supersymmetry is a possible approach to address these questions, as described for example by Martin [8]. This model predicts the unification of the electroweak and strong forces at the scale of the Grand Unified Theory. This idea is based on the symmetry principle of gauge invariance with which the unification of the weak and electromagnetic interactions was accomplished. A full set of supersymmetric partners must be introduced for both fermions and bosons, different in spin by  $\frac{1}{2}$ . As a result, e.g. radiative corrections to the Higgs mass cancel in a natural way solving the so-called hierarchy problem of the Standard Model. The lightest supersymmetric particle might be neutral and stable and therefore is a good candidate for the dark matter.

Supersymmetry incorporates a Higgs model, which in the minimum supersymmetric extension of the Standard Model consists of two doublets resulting in three neutral and two charged physical Higgs bosons. If supersymmetric particles will be generated at the ILC, one will be able to discover them and to measure their quantum numbers.

### 2.1.3 More Physics beyond the Standard Model

The ILC will be sensitive to effects of many other theoretical proposals such as contact interactions, additional gauge bosons or even extra dimensions. It will allow measurements with much higher precision than the LHC and enable us to detect deviations from the Standard Model in simple processes like  $e^+e^- \rightarrow f\bar{f}$ , with  $f$  denoting a fermion. The mentioned new phenomena will contribute to the cross sections and angular distributions of these processes already at energies far below, e.g. the masses of the new particles, due to interference of their amplitudes with the Standard Model amplitude. In this manner, the capabilities of the ILC go far beyond its direct energy reach.

## 2.2 Technical Challenges for the ILC

### 2.2.1 The Accelerator

Higher beam energies than at the circular LEP can be reached with a linear accelerator. To obtain a collider the electrons and positrons are accelerated separately in opposite directions towards each other. They are brought into collision at the interaction point (IP) in the middle of this approximately 35 km long facility. In Figure 2.2 the layout of the ILC accelerator is shown schematically.

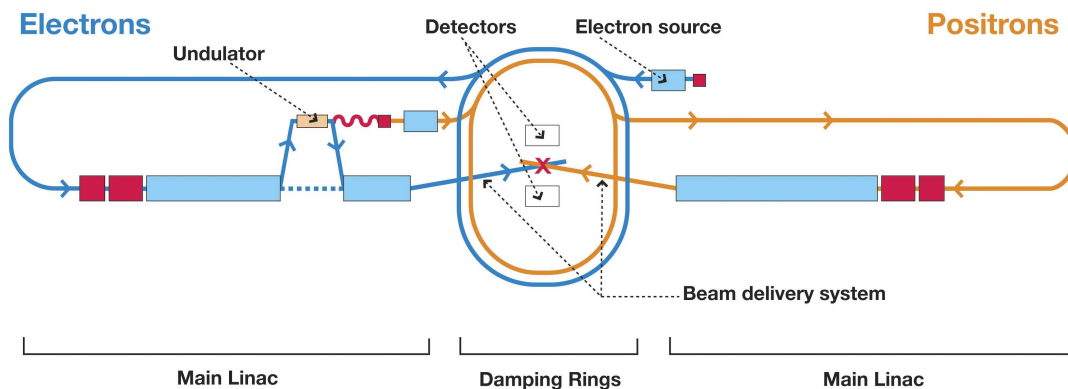


**Figure 2.2:** Layout of the International Linear Collider. Bunches of electrons and positrons are shaped in the damping rings and then accelerated in the main linacs towards the interaction region. The beam delivery system leads the beams into the detector and performs the final focussing.

The beams do not consist of a continuous particle flux but are structured. Bunches of  $\sim 10^{10}$  particles are shaped in the damping rings to have low emittance and to allow a

nanometer beam spot in the final focus. Orders of  $10^3$  bunches are extracted to form a train, which is accelerated in superconducting niobium cavities in the main linac along the  $z$ -axis. In one second five trains, also called pulses, arrive at the IP. There, the alignment of the beams must be realised with nanometer precision.

After passing the IP, the spent bunches must be extracted from the path of the beam coming from the opposite direction. Otherwise they would interact with the oncoming bunches already before the IP and affect the initial conditions. This can be done by means of special cavities in the beam delivery system. Another possibility is to cross the beams with a small angle, the beam crossing angle  $\theta_{\times}$ .

## 2.2.2 ILC Luminosity

The event rate of a process is proportional to its interaction cross section  $\sigma$ , given by nature, and to the luminosity  $\mathcal{L}$ , which is a machine parameter,

$$\frac{dN}{dt} = \mathcal{L}\sigma . \quad (2.1)$$

The luminosity for colliding beams consisting of bunches with particle numbers  $n_1, n_2$  and the geometric cross section  $A$  is

$$\mathcal{L} = \frac{n_1 n_2 f_b}{A} . \quad (2.2)$$

There,  $f_b$  is the number of bunch crossings (BX) per time interval. In the special case of ILC this frequency is the product of the repetition rate for trains,  $f_{\text{rep}}$ , and the number of bunches per train,  $n_b$ . Assuming a Gaussian charge distribution in the bunches, the area  $A$  can be replaced with the product of the transverse bunch dimensions  $\sigma_{x,y}$ . The geometric luminosity at the ILC, where  $n_1 = n_2 = n$ , in first order reads then [9]:

$$\mathcal{L} = \frac{n^2 f_{\text{rep}} n_b}{4\pi\sigma_x\sigma_y} . \quad (2.3)$$

The interaction cross sections of several interesting processes are predicted to be of the order of around 100 fb, as can be seen in Figure 2.3. For example, for the Higgs-strahlung process (red curve that is labelled 'Zh' in the figure), it is  $\sigma(e^+e^- \rightarrow ZH) \approx 60$  fb at  $\sqrt{s} = 500$  GeV, assuming a mass of  $m_H = 120$  GeV for the Higgs boson. In order to obtain a reasonable amount of events, the anticipated luminosity is  $\mathcal{L} \geq 2 \cdot 10^{34} \text{ cm}^{-2} \text{ s}^{-1}$ . The result will be a Higgs-strahlung rate of about 37 000 events per year.

According to Equation (2.1), the luminosity determines the event rate for a certain process. Thus the time-integrated luminosity,  $L$ , gives a measure for the accumulated statistics:

$$L = \int \mathcal{L} dt = \frac{N}{\sigma} . \quad (2.4)$$

The ILC luminosity is designed to deliver  $L = 500 \text{ fb}^{-1}$  per year under stable running conditions.

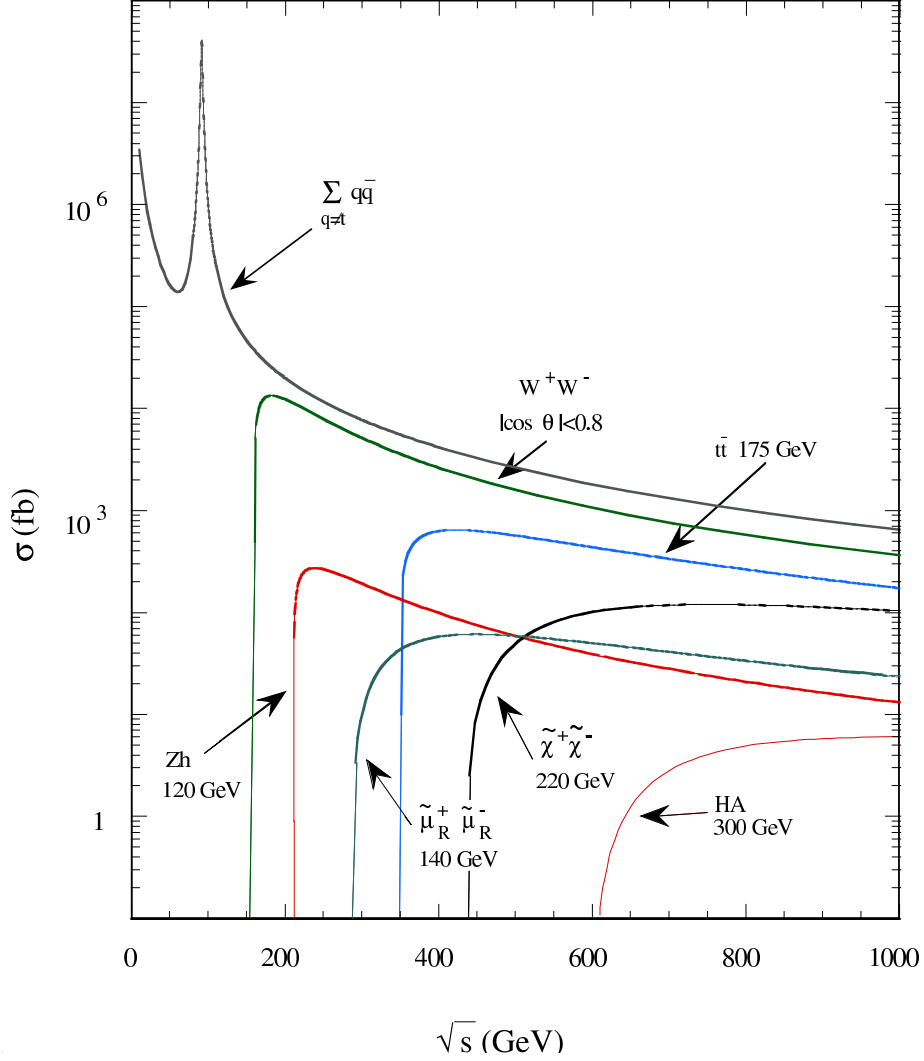


**Figure 2.3:** Interaction cross sections for some interesting final states in  $e^+e^-$  collisions within the energy range of the ILC.

### 2.2.3 Pinch Effect

The particles are kept together in a bunch against the Coulomb repulsion not only by means of the lensing fields of the quadrupole magnets but also by the magnetic field they induce themselves when moving. Two colliding bunches influence each other during penetration. As they come from opposite directions, in the case of opposite charges, their magnetic fields add up. Off-centre particles thus are accelerated towards the beam axis. This so-called pinch effect additionally focusses the bunches at the IP, that is, it reduces the beam cross section  $A$ . Hence the luminosity (2.3) is increased by the enhancement factor  $H_D$ :

$$\mathcal{L} = \frac{n^2 f_{\text{rep}} n_b}{4\pi \sigma_x \sigma_y} \cdot H_D . \quad (2.5)$$

Typical values for this increase at the ILC are  $H_D \approx 2$ . One can maximise this effect by focussing the beams such that the vertical waists emerge shortly before the IP [10].

However, the pinch effect also has a drawback. Charged particles moving on bent trajectories emit synchrotron radiation, called beamstrahlung if generated in beam-beam interaction. This involves an energy loss of the particles. A beamstrahlung parameter  $\Upsilon$  is introduced to describe this effect. Its average value can be approximated after Chen [11] by

$$\Upsilon \propto \frac{n \cdot \gamma}{(\sigma_x + \sigma_y)\sigma_z},$$

with  $\gamma$  denoting the relativistic factor and  $\sigma_z$  the bunch length. The correlation between this parameter and the average relative energy loss due to beamstrahlung is given as:

$$\frac{\Delta E}{E} \propto \frac{\Upsilon^2 \sigma_z}{E} \propto \frac{n^2 \cdot \gamma}{(\sigma_x + \sigma_y)^2 \sigma_z}. \quad (2.6)$$

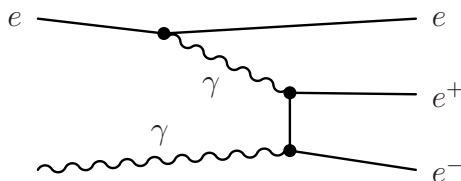
This quantity is estimated to be between 3 and 6 %, depending on the beam parameters.

Comparing (2.6) and the luminosity in (2.5), one can see that both depend on the transverse bunch dimensions. As mentioned above, the beam cross section, scaling with the *product* of  $\sigma_x$  and  $\sigma_y$ , should be small to increase the luminosity whereas the energy loss can be reduced when the *squared sum* of them is large. The problem is solved by choosing a flat shape for the bunches with a horizontal extension of  $\sigma_x \approx 100\sigma_y$ . A comprehensive overview of the beam parameters suggested for the ILC is given by Raubenheimer [12] and in extracts, relevant within the context of this work, also in Table 2.1 on Page 22.

## 2.2.4 Beamstrahlung Pairs

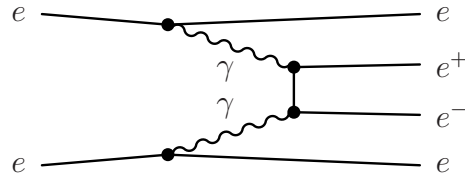
Beamstrahlung photons are emitted in the direction of the beam and have to pass through the colliding bunch. In doing so, they can interact with that bunch and produce  $e^+e^-$  pairs with a certain angular distribution. These pairs hit the inner and forward detectors and can disturb the detection of interesting events. Coherent pair creation, which takes place in interactions of a beamstrahlung photon with the collective electromagnetic field of the oncoming bunch, does not need to be considered at the given energies [13]. There are three main processes contributing to interactions between individual particles, called incoherent pair creation (IPC) [9, 14]:

- Most important is the Bethe-Heitler process (BH):



A real photon from beamstrahlung interacts with a virtual one emitted from a bunch particle. Due to the involved on-shell photon the probability depends on  $\Delta E/E$ .

- The interaction of two real beamstrahlung photons,  $\gamma\gamma \rightarrow e^+e^-$ , called Breit-Wheeler process, also scales with the energy loss. The contribution to pair production is small.
- Two virtual photons accompanying the high energy particles in off-shell photon clouds can produce pairs by means of the Landau-Lifshitz process (LL):



The rate of such events scales with the luminosity. In the ILC baseline design, the LL cross section is half that of BH and consequently this is true for the number of generated secondary electrons.

Those IPC beamstrahlung pairs form the main background in the ILC detector. Their amount and behaviour must be estimated in order to optimise the detector design, concerning e.g. the geometrical shape, masks for shielding or the readout speed.

## 2.3 A Detector for the ILC

### 2.3.1 Complex Detectors for High Energy Physics

In general, the structure of detectors for high energy physics experiments is similar. Different layers of sub-detectors are built around the interaction point as encompassing shells. For the reconstruction of events, the identity of the generated particles and the kinematics of the processes need to be measured.

Charged particles deposit energy in the material they traverse due to ionisation. In the inner part of a typical detector, the tracker system is located to trace back the tracks using a minimum amount of material. A high resolution pixel detector is positioned as close as possible to the interaction point. It determines the vertices of the primary interactions, which are distributed over the intersection volume of the crossing bunches. Furthermore, it can register decay vertices of short living particles. In a solenoidal magnetic field, the trajectories of charged particles are bent in the plane perpendicular to the beam, which allows to determine the particle's momenta. Their paths can be tracked by reading out the deposited energies on spatial segments.

The total energy of both charged and neutral particles can be measured in the surrounding calorimeters. Absorbers made of heavy material with short radiation length force most particles to release their energy producing showers of secondary particles. A high energetic electron, for example, generates bremsstrahlung photons, which in turn convert into  $e^+e^-$  pairs. These, again, emit bremsstrahlung, and this avalanche continues until the energy is reduced to a critical value. The number of produced secondaries is proportional

to the energy of the incident particle. Sensors with a certain spatial segmentation, called granularity, read out the deposited charge and energy.

Separate detectors are used in the forward region to detect particles that are produced with very small angles with respect to the beam, taking into account enhanced radiation doses near the beam pipe.

### 2.3.2 The Large Detector Concept

The large detector concept (LDC), described in detail in the detector outline document [15], is one of four different design concepts for an ILC detector [16]. A scheme of the full detector is displayed in Figure 2.4. It is composed of several sub-detectors built around the interaction point. The IP also marks the origin of the LDC coordinate system [17]. This is right-handed with the  $z$  axis following the electron beam (if no crossing angle is applied) and the  $y$  axis pointing upwards.

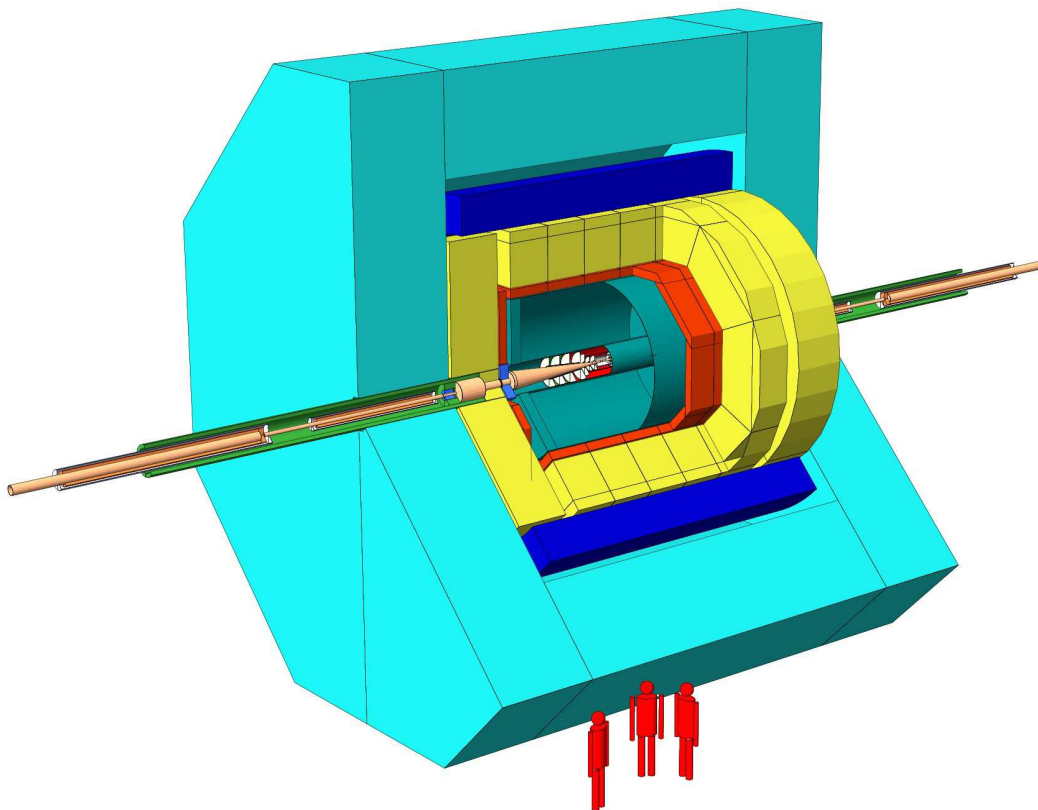


**Figure 2.4:** Structure of the LDC detector. The silicon trackers close to the IP, partially shown in white, are enclosed in the turquoise TPC. The successively surrounding layers are the ECAL in red, the HCAL in yellow, the coils in dark blue, and the iron yoke in cyan.

The innermost device, very close to the IP, is the vertex detector. The entire tracker system contains different silicon trackers and a cylindrical time projection chamber (TPC).

It is surrounded by electromagnetic (ECAL) and hadronic (HCAL) calorimeters, each consisting of a barrel and two end caps to cover a solid angle of nearly  $4\pi$ . All this is enclosed in superconducting coils, providing a magnetic solenoid field of 4 T. On the outside, this field is returned by an iron yoke, which additionally serves as a muon detector.

Additional calorimeters are placed in the very forward direction, close to the beam pipe but remote from the IP, performing special tasks in this particular region. A luminosity (LumiCal) and a beam calorimeter (BeamCal), both for the measurement of electromagnetic showers, are positioned at positive and negative  $z$  values each. As the detector is mirror-symmetric, usually only the half at positive  $z$  is considered. The very forward region will play a central role in this work and is discussed further on (Figure 2.6 on Page 15). Also a hadronic calorimeter for low polar angles is proposed, called LHCAL.

### 2.3.3 Vertex Detector and Tracker System

The tracks of charged particles are recorded by the tracker system to detect clear signatures from processes such as, e. g., the  $Z$  decay, mentioned in Section 2.1.1. The main tracker in the LDC is a cylindrical TPC (red in Figure 2.5), nearly 3 m in diameter. The barrel has a length of about 4.3 m with a central, light weight cathode at  $z = 0$  and two end plates with micro-pattern gas detectors. Charged particles ionise the gas along their paths, and the released electrons drift in the electric field parallel to the  $z$  axis to the electron-amplifying micro-pattern. By measuring both the  $x$ - $y$  coordinate on the end plate and the drift time,

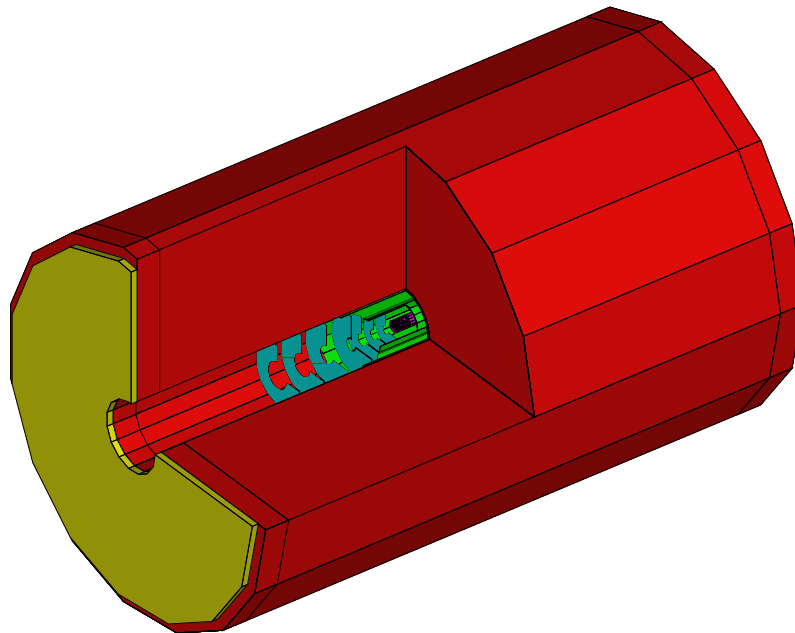


**Figure 2.5:** The tracker system of the LDC detector. The vertex detector (purple) in the center, the silicon intermediate tracker (green), and the forward tracking discs (blue) are silicon devices. The time projection chamber, TPC (red, other than in Figure 2.4), is filled with gas. The slices outside both end caps (yellow) are further silicon discs.

up to 200 three-dimensional space points per track are obtained. However, the inner radius of the TPC is 30 cm and does not allow to measure tracks near the beam pipe.

The vertex detector (VXD, purple in Figure 2.5), five layers of very thin silicon pixel detectors, encompasses the beam pipe at the IP position. The innermost layer has a radius of only 15 mm. Its  $z$  extension is restricted to  $\pm 50$  mm to prevent it from being exposed to high dose rates from beamstrahlung pairs at small polar angles. The other layers reach from  $z = -125$  mm to  $z = +125$  mm.

The distance from the VXD to the enfolding TPC is bridged by two cylindrical strip detector layers, named silicon intermediate tracker (SIT, green in Figure 2.5). Larger cylinder radii and lengths result in a latitude angle coverage in the same range as for the outer VXD layers.

Particles at small angles with respect to the beam can be detected by means of the forward tracking discs (FTD, blue in Figure 2.5). These are seven round slices (considering only  $z > 0$ ) parallel to the  $x$ - $y$  plane around the beam pipe. They are made of  $300 \mu\text{m}$  thick silicon, where the three closest to the IP have a pixel structure. The others are strip detectors, for which the number of readout channels is reduced considerably.

In order to trace back particle tracks to the corresponding vertex points, their hits must be found in the presence of background. The study of this background is a major topic of the work at hand. Hence the silicon trackers are described in more detail in the corresponding chapter.

### 2.3.4 Calorimeters

The energy and the type of particles initiating showers in the calorimeters can be determined with certain accuracy. These information are indispensable for the complete event reconstruction. The assignment of detected signals, called hits, to tracks and clusters poses a special challenge for the reconstruction software.

The novel concept of particle flow analysis [18] is suggested for some ILC detectors to measure the energy of jets: It is tried to assign all calorimeter clusters to reconstructed tracks of charged particles, whose momenta are measured much more precisely from the track's curvature. Remaining clusters, not matching any track, are assumed to be caused by neutral particles. The local calorimeter deposits<sup>1</sup> are used to determine energy and direction of these particles. The jet energy is then obtained as the sum of the charged particle energies, measured in the tracker, and the deposits from neutral particles in the calorimeter. High granularity is needed to ensure that the particle flow analysis can be applied. Different technologies are in discussion to reconcile high resolution and low costs.

ECAL will be a sandwich calorimeter with either tungsten or lead absorbers interspersed with silicon sensor layers, subdivided into pads. At a radius of about 1.6 m, a large area has to be covered. Scintillators could be substituted (even partially) for the expensive silicon. For the readout of the scintillators, novel silicon photo-multipliers (SiPMs) [19], which are

---

<sup>1</sup>The term “deposit” denotes the energy deposited in a certain element of extension whereas a “hit” is a space point where a particle meets a detector element, usually used in a logical sense on simulation level.

small multi-pixel photo-diodes operating in the Geiger mode, would replace multichannel photo-multipliers.

There are two technologies under consideration for the hadronic calorimeter, both using iron absorbers. The analogue HCAL also uses scintillator sensors with analogue readout via SiPMs. Alternatively, in the digital HCAL, gaseous detectors with a single-bit resolution read out hits proportional to the energy of the primary particle. The active detector elements, either RPCs (Resistive Plate Chambers) or GEMs (Gaseous Electron Multipliers), are characterised by small readout cells leading to a huge number of readout channels. See the detector outline document [15] and references cited therein for further information.

### 2.3.5 Forward Calorimeters

In the very forward region, additional calorimeters are placed, covering polar angles in the range of  $5 - 154$  mrad with respect to the beam. This is necessary to fully exploit the physics potential expected in the energy range of the ILC, and to extend hermiticity. Specific tasks are beam diagnostics and the high precision measurement of the luminosity  $\mathcal{L}$  [20]. The proportions of the very forward region are illustrated in Figure 2.6.

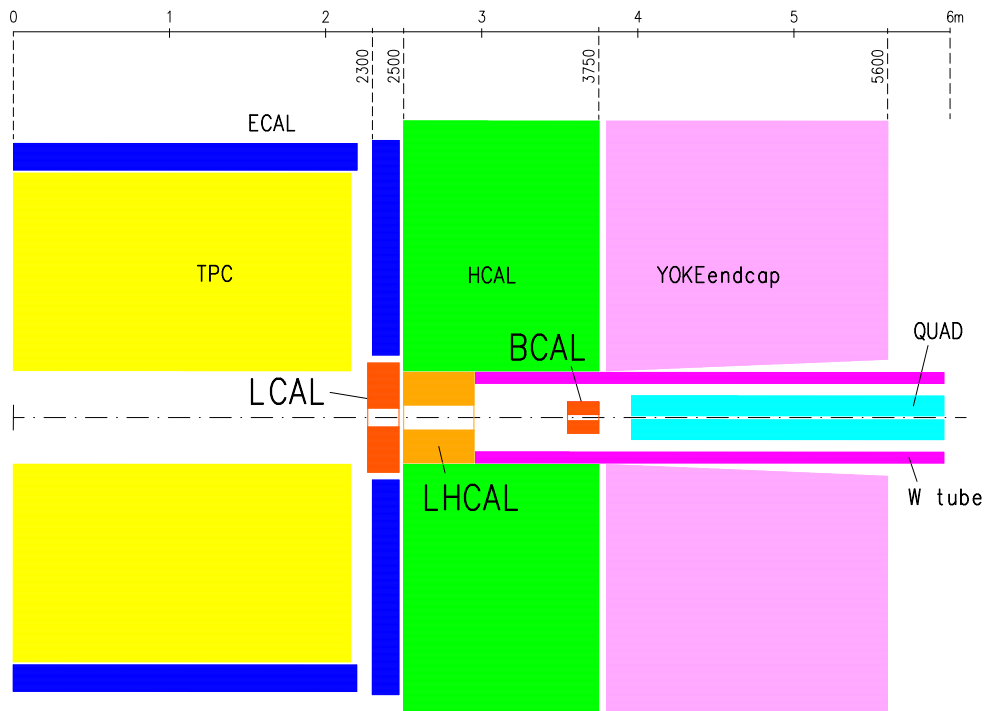


**Figure 2.6:** Scheme of the  $y = 0$  plane for the detector half at positive  $z$ . The IP is located at the left edge at the zero point of the scale given on top of the picture. In the centre of the ECAL (blue) and the HCAL (green) end caps, the very forward region is situated. LumiCal and BeamCal, both in red, are denoted as LCal and BCal, respectively. QUAD (turquoise) symbolically shows the final quadrupole of the beam delivery system.

The luminosity calorimeter is positioned at a distance of 2.27 m from the IP (on both

sides). It is centered around the beam pipe with an inner radius of 100 mm in the baseline design. This corresponds to a minimal polar angle of 44 mrad. The outer radius is 350 mm, approaching the inner radius of the ECAL end cap. Based on the measurement of the theoretically well known Bhabha scattering, a precision of  $\Delta\mathcal{L}/\mathcal{L} = 10^{-4}$  can be achieved for the luminosity measurement.

LumiCal is designed as a compact, cylindrical tungsten-silicon sandwich calorimeter, as depicted in Figure 2.7. The longitudinal depth of LumiCal is 200 mm holding up to thirty absorber-sensor layers. The thickness of the tungsten planes is chosen to be one radiation length  $X_0 = 3.4$  mm. Each is adjoined by a  $300\ \mu\text{m}$  thick silicon sensor plane with high granularity and the cabling. In detail this means a segmentation into 48 azimuthal sectors and 96 concentric strips.

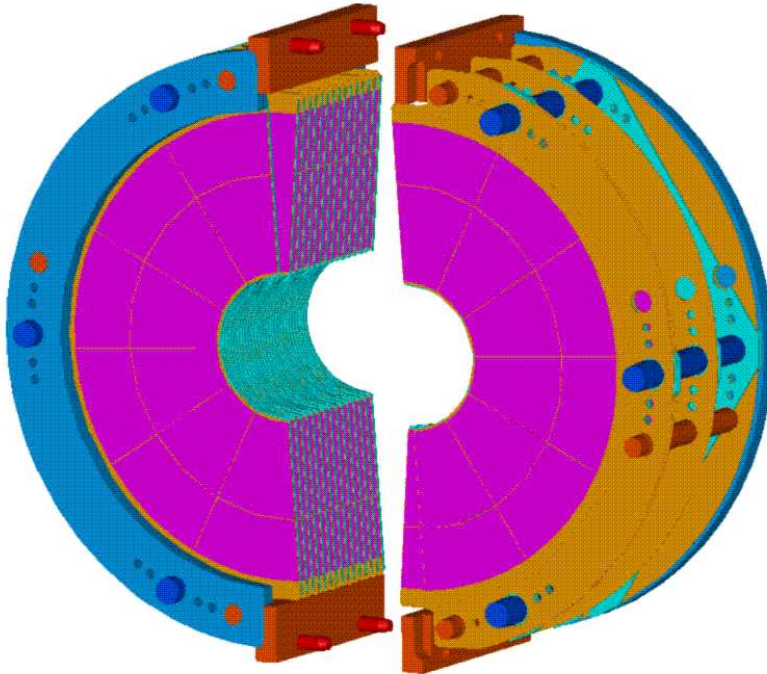


**Figure 2.7:** Design proposal for the luminosity calorimeter.

The beam calorimeter is placed adjacent to the beam pipe in front of the final quadrupole. The distance of this device from the IP is  $z = \pm 3.55$  m. For the baseline design, the inner and outer radii are 15 mm and 165 mm, respectively. The latter corresponds to a polar angle of 46 mrad, slightly overlapping with the LumiCal. One task of the BeamCal is fast beam diagnostics using beamstrahlung pairs to optimise the luminosity at run time. Furthermore, the detection of high energetic electrons at very low angles is important for the physics, e. g. to veto Standard Model processes with a similar signature in the detector like supersymmetric particles. It also serves as a mask to shield both the final focussing magnet from beamstrahlung and the inner detector elements from particles still scattered off the quadrupole.

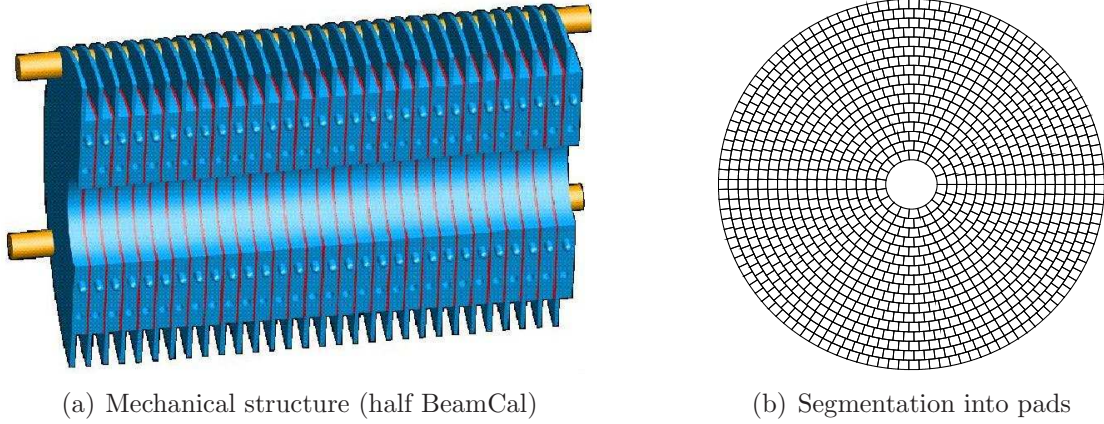


**Figure 2.8:** Layout of the beam calorimeter (a) as a whole and (b) in the sensor planes.

BeamCal is a sandwich calorimeter like LumiCal. Its proportions are displayed in Figure 2.8(a). Thirty absorber discs of tungsten are foreseen with a thickness of one radiation length each. In between the sensor planes are accommodated. For optimum shower resolution, they are subdivided into pads nearly uniform in size over the whole annulus, as shown in Figure 2.8(b) in principle.

For this thesis, treating the impact of the background on certain sub-detectors, the beam calorimeter is of crucial importance. Most of the beamstrahlung pairs are generated in a small cone around the beam and load the very forward region. A fraction of 5 to 10 % smashes into the BeamCal and induces electromagnetic showers in the absorber. The energy spectrum of particles in the showers was simulated by Drugakov [21] and is shown in Figure 2.9 for different penetrating depths. For the energy deposition in the sensors,

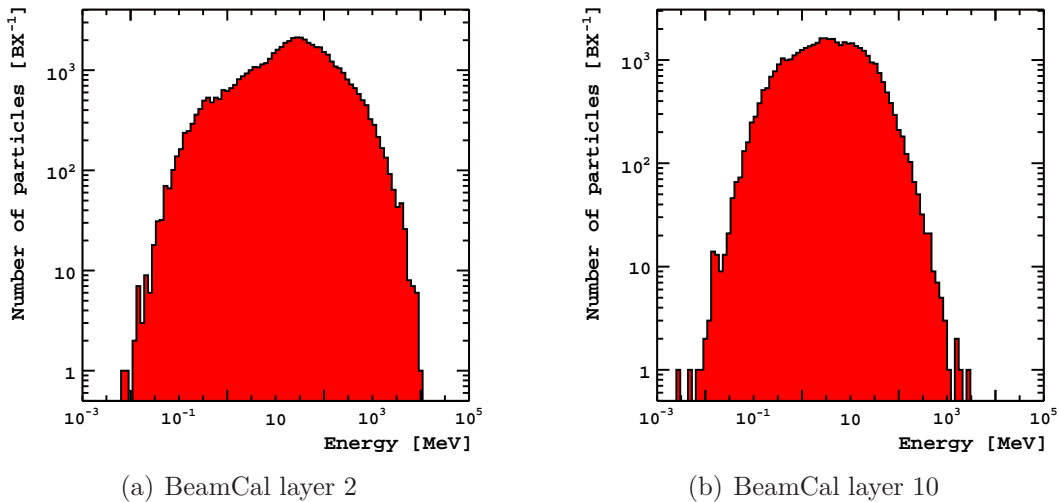


**Figure 2.9:** Energy spectra of the electrons in the shower after (a) two and (b) ten radiation lengths in the beam calorimeter.

dose rates of up to 10 MGy/year are expected. To resist such an exposure, the sensors need to be radiation hard. Polycrystalline CVD diamonds are one option for the material. The following chapter is devoted to the test of such sensors in an electron beam.

Due to the high atomic number of the absorber material, beamstrahlung remnants also scatter off the BeamCal back into the tracker system. As a result, a large background is produced in the central tracking devices. Among others, the design of the very forward region and the magnetic field in the detector influence this background. The amount of hits and deposits in the sub-detectors need to be estimated for the optimisation of the detector performance. The Chapters 4 and 5 are concerned with the background caused by electron-positron pairs in the silicon trackers of the LDC detector. In order to reduce the amount of low energetic particles scattered back at the BeamCal, a 5 mm graphite absorber is proposed to be installed directly in front of the IP-facing side of BeamCal.

## 2.4 Machine Detector Interface

The layout of the ILC partially governs the detector design and as well the latter can have implication in accelerator parameters. Machine detector interface is a term that incorporates all the subjects where the detector influences the accelerator layout and vice versa. Obviously, the machine-induced detector background, which is studied in this work, belongs to this topic. Moreover, it includes the design of the interaction region and the beam delivery system. The latter guides the beams from the linac into the detector. Part of the beam delivery system is the final focussing quadrupole, extending into the detector to a distance of  $L^* = 4.05$  m from the IP. It leads the beam through the very forward region, wherefore this is concerned, too.

Further items of the machine detector interface, particularly considered in this work, are the beam parameters, the beam crossing angle, and the magnetic field in the detector. They are described in more detail below.

### 2.4.1 Beamstrahlung-induced Background

As described in Section 2.2.3, we face a new phenomenon at the ILC due to the small bunch sizes: the beamstrahlung. Particles do not only interact in direct collisions as desired but are affected by Lorentz forces when bunches cross. Deflecting an electron owing to this pinch effect, taking just 1% of its energy in the case of 250 GeV beam energy means to create a 2.5 GeV beamstrahlung photon. This, in turn, is able to produce an  $e^+e^-$  pair with similar energy. Due to deflection inside the bunches, the momenta of the IPC pairs obey a certain angular distribution, leading to larger transverse momenta  $p_t$ . The beam pipe is conical in the tracker region to hold the major fraction of the pairs inside (cf. Figure 2.4). The transverse momentum distribution depends on several machine parameters and is different for electrons and positrons.

A remarkable fraction of pairs originating from beamstrahlung photon conversion is directed to the very forward region but does not disappear into the beam pipe. When

smashing into the BeamCal, they interact with the electrons and nuclei in the material. A small fraction of the created shower is scattered backwards. Low energetic charged particles are guided back to the central tracker system curling around the magnetic field lines of the detector solenoid.

In addition, also neutral particles are produced, moving independently of the magnetic field. Photons, for example, can generate further electrons and positrons as they act on material in three processes: pair production, photoeffect, and Compton effect. The consequence are additional deposits in the tracking devices. Much more problematic are neutrons. They collide elastically and fly around like ping-pong balls. Because of their mass, they affect, e. g. the bulk material of the silicon and diamond sensors and are capable of destroying the lattice structure, especially in materials with low atomic number. This would deteriorate the detector performance. Their flux through the tracker region can only be estimated in the simulation. Hence, it is also very important to obtain their number, energy spectra and spatial distributions, though this is not investigated in the work at hand.

## 2.4.2 LDC Geometry and Beam Options

The structure of the LDC detector was described in Section 2.3. However, several details in the ILC layout are not fixed yet. The options under discussion have to be evaluated in order to find the most efficient and most suitable one. For this study the beam delivery system is important. Crucial parameters are, e. g., the beam crossing angle,  $\theta_{\times}$ , and the focal length of the last focussing quadrupole,  $L^*$ . Inside the detector, a solenoidal magnetic field is induced, which may need small modifications for a non-zero beam crossing angle.

In this work, the background due to beamstrahlung remnants in the inner tracking detectors is estimated for different options of the crossing angle and the magnetic field.  $L^* = 4.05$  m is kept constant. In addition, the influence of several beam parameters is considered.

### 2.4.2.1 Beam Crossing Angle

The beam crossing angle  $\theta_{\times}$  is defined as the smaller angle between the electron and the positron beam. Values of  $\theta_{\times} = 2$  mrad, 14 mrad, and 20 mrad are under consideration. In case of 2 mrad (or head-on), the spent bunches must be extracted from the beam line outside the detector by electrostatic or magnetic separators. For the larger crossing angles, a second pipe already starting in the very forward region is needed. This increases the complexity of the detector as e. g. the BeamCal cannot simply be azimuthally symmetric. The structure of its sensor layers is depicted in Figure 2.10 for a crossing angle of 14 mrad, viewing from the IP along the electron beam (positive  $z$  direction). Beams from the linac, entering the detector upstream the IP, are called “incoming”. The spent bunches, moving downstream the IP, are denoted as “outgoing” beams. BeamCal is centered around the outgoing beam pipe. The unsegmented sector in Figure 2.10 holds the pipe for the incoming positrons.

In the baseline design, an angle of 14 mrad is chosen. This corresponds to the minimal angle allowed by the geometry of the last focussing quadrupoles when separate magnets for the incoming and outgoing beams are used. To ensure maximum luminosity, a crab crossing cavity is foreseen in the beam delivery system. It turns the bunches of both beams by half the crossing angle to collide them in a minimal effective cross section area.

As the beam crossing angle lies in the  $x$ - $z$  plane of the LDC detector, it breaks the symmetry in this plane. This might have an effect on the distribution of the background in the detector. On both detector halves, the respective incoming beams and the detector's  $z$  axis enclose half the beam crossing angle at  $y = 0$  and negative  $x$ . The same applies to the outgoing beams at positive  $x$  values. Polar angles in the LDC detector with respect to the  $z$  axis will be denoted with a squiggly  $\vartheta$ . Angles that refer to the (outgoing) beam are expressed by a straight  $\theta$ , as for the beam crossing angle  $\theta_x$  between incoming and outgoing beam.

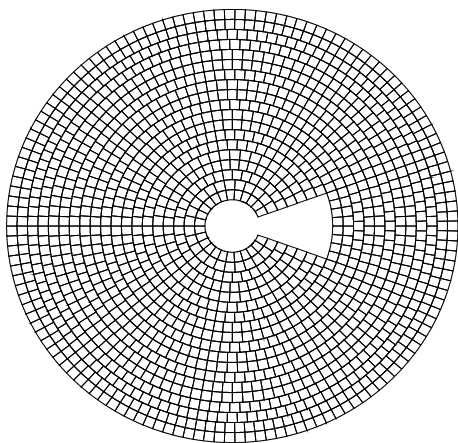


**Figure 2.10:** Asymmetric structures in the BeamCal in case of larger  $\theta_x$ . In the central hole, the outgoing beam pipe is enclosed. The non-instrumented sector accommodates the incoming pipe.

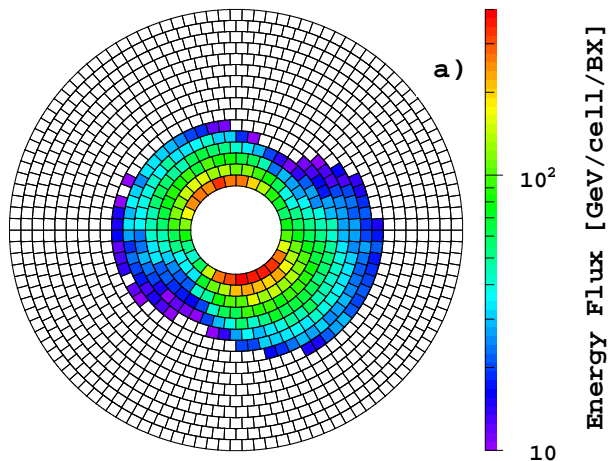


**Figure 2.11:** Expected energy distribution in BeamCal due to beamstrahlung remnants for  $\theta_x = 2$  mrad, solenoidal magnetic field, and one bunch crossing. The energy density is largest at small radii and highly asymmetric in the azimuth angle.

### 2.4.2.2 Magnetic Field Configuration

Although the LDC detector is cylindrically symmetric and its magnetic field is a pure solenoid in case of the small crossing angle, there are structures in the background. In Figure 2.11 one can see the expected energy distribution of beamstrahlung remnants in BeamCal for one single bunch crossing. As expected, the energy density is highest near the beam pipe. However, it also depends strongly on the azimuth angle. The reason for that is the flat shape of the beams. Pairs are produced with small polar angles in the whole cross section area of the colliding beams. In the magnetic field they are forced on helical

trajectories due to their transverse momenta.

Another inconvenience occurs for crossing angles different from zero: the beam path would no longer be parallel to the solenoidal magnetic field lines. One consequence is a precession of the particle spin as discussed by Parker and Seryi [22]. To solve this problem, a modification of the solenoid field was proposed by means of a detector-integrated dipole (DID). It bends the magnetic field lines such that they match the orientation of the *incoming* beams and do not affect their properties upstream the IP.

Though, the impact of the magnetic field on the outgoing beams is enhanced then, as the angle between the field lines and the beam direction doubles downstream the IP. The polarisation of particles measured in the outgoing beams must be corrected for the spin precession. In addition to that, charged particles from beamstrahlung curl around the magnetic field lines towards the incoming beam pipes. The pairs arrive at the BeamCal with a spatial distribution as shown in Figure 2.12 [23]. With DID field the background is enhanced considerably and spread asymmetrically over a larger area.

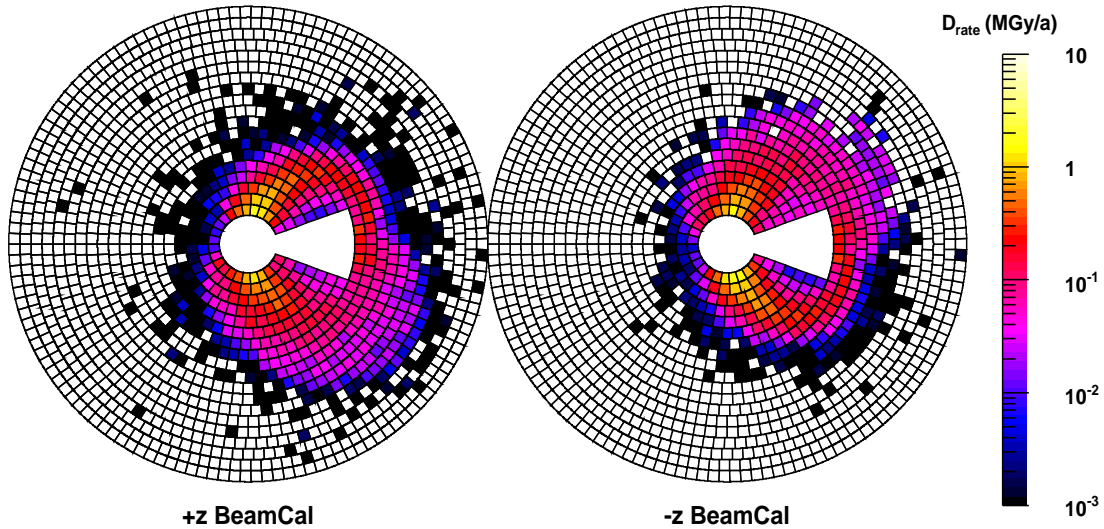


**Figure 2.12:** Spatial distribution of the dose rate in BeamCal for  $\theta_x = 14$  mrad and DID field. The field lines are parallel to the incoming beams. Electrons and positrons from beamstrahlung are guided helically around these field lines. For better comparison the sensor layers of both sides are depicted with the same orientation.

The modification of the solenoid field where the dipole aligns the magnetic field lines with the *outgoing* beams is called anti-DID option. A spin precession correction has to be applied in any case, so it can be done before the bunches cross, where the states of motion are well known. The anti-DID focusses the beamstrahlung pairs into the outgoing beam pipe and a smaller fraction hits the BeamCal, reducing also the background backscattered into the tracker system.

### 2.4.2.3 Beam Parameter Sets

From the accelerator point of view, several sets of beam parameters are under consideration. Two of them are considered here and briefly described in Table 2.1. The parameter set of the *Tesla* machine [24] is given for comparison.

The *Nominal* beam parameters are inherited from the *Tesla* baseline set and adapted to the conditions at the ILC. Therefore both are similar. At TESLA, the anticipated luminosity was nearly one and a half that for the ILC, leading to a larger beamstrahlung.

As a second important proposal, the so-called “low beam power” set (*LowP*) is considered. It would reduce the power consumption of the linac and facilitate damping by halving the number of bunches per pulse,  $n_b$ . This option is favourable in terms of costs, as it would economise on cavities. On the other hand, the luminosity must be recovered by smaller beam sizes. This could be managed by the beam delivery system but would increase the beamstrahlung.

There are even further sets such as “low charge”, “large spot”, or “high luminosity”. They all are discussed in detail by Raubenheimer [12].

		<i>Tesla</i>	<i>Nominal</i>	<i>LowP</i>
<b>Beam parameters</b>				
center-of-mass energy $\sqrt{s}$	GeV	500	500	500
Repetition rate $f_{\text{rep}}$	Hz	5	5	5
Bunch charge	$10^{10}e$	2	2	2
Bunches per pulse $n_b$		2820	2820	1330
Bunch spacing	ns	336.9	307.7	461.5
<b>Parameters at the interaction point</b>				
Beam width $\sigma_x$	nm	554	655	452
Beam height $\sigma_y$	nm	5.0	5.7	3.8
Bunch length $\sigma_z$	$\mu\text{m}$	300	300	200
Geometric luminosity (2.3)	$10^{34} \text{ cm}^{-2} \text{ s}^{-1}$	1.64	1.20	1.24
Enhancement factor $H_D$		1.80	1.70	1.65
Luminosity $\mathcal{L}$	$10^{34} \text{ cm}^{-2} \text{ s}^{-1}$	2.94	2.03	2.05
IPC pairs per BX	$10^5$	4.14	2.59	6.12

**Table 2.1:** Selection of some important parameters for the beam parameter sets *Tesla*, *Nominal*, and *LowP*.

# Chapter 3

## Testbeam Studies

### 3.1 Testbeam Setup and Simulation

For the instrumentation of the beam calorimeter of the ILC, which is exposed to high dose rates, diamond sensors are an option to detect charged particles in electromagnetic showers. The performance of the sensors as a function of the absorbed dose is measured using an electron testbeam at the DALINAC accelerator of the TU Darmstadt. The diamond sensor samples are irradiated for time intervals of roughly 1 hour. In between the charge collection distance is measured using  $\beta$ -particles from a  $^{90}\text{Sr}$  source to characterise the sensors concerning the detection of charged particles.

The sensors are polycrystalline diamonds, grown in chemical vapour deposition, with a thickness of 300 to 500  $\mu\text{m}$ . Their quadratic surfaces of 12 mm  $\times$  12 mm are metallised on an area about 10 mm  $\times$  10 mm. One sample is shown in Figure 3.1. Samples from different manufacturers are compared.

When passing through the sensor, charged particles ionise the material and deposit a fraction of their energy along their path. Both the electrons in the testbeam and those emitted by the source can be considered to be minimal ionising particles (MIPs). The average charge induced by ionisation,  $Q_{\text{induced}}$ , is calculated using the Bethe-Bloch formula. Applying high voltage to the electrodes, the charge carriers drift through the sample, where a fraction is trapped in lattice imperfections. The ratio of the measured charge,  $Q_{\text{measured}}$ , over the induced charge, scaled with the sensor thickness  $d$ , is referred to as charge collection distance:

$$\delta = \frac{Q_{\text{measured}}}{Q_{\text{induced}}} \cdot d. \quad (3.1)$$

The sensor samples are exposed to an electron beam with 10 up to 100 nA and an energy of 10 MeV—a typical energy of electrons in a shower as seen in Figure 2.9. The number of electrons penetrating the sample per time can be determined by measuring the current from a Faraday cup downstream the sensor. From the number of traversed

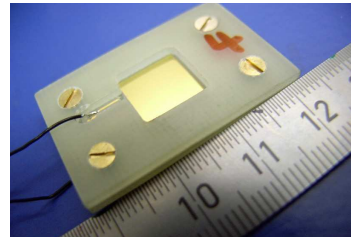
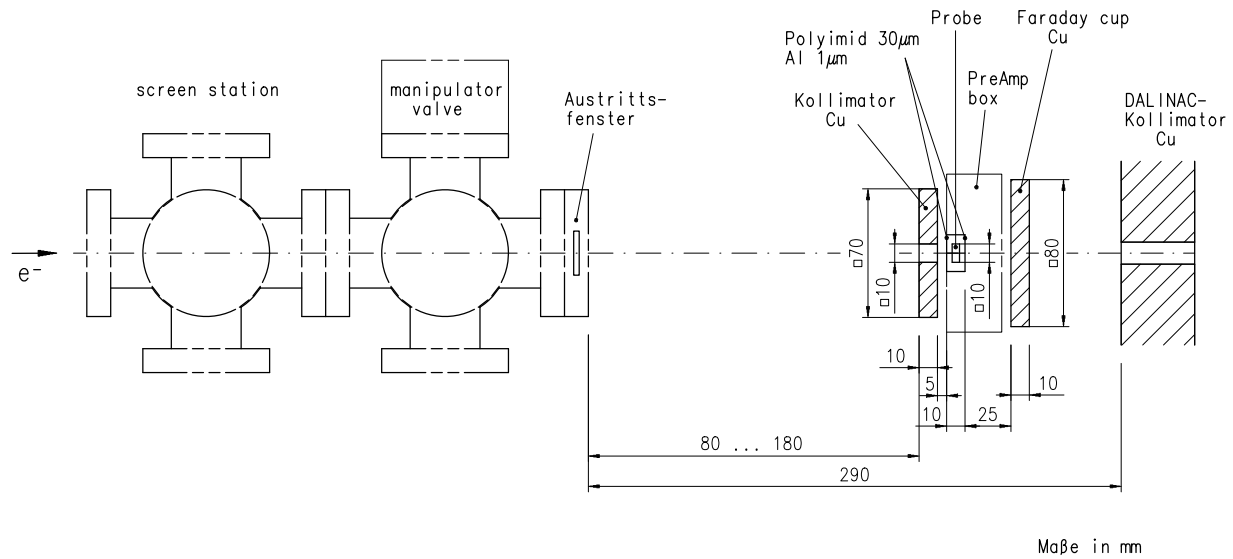


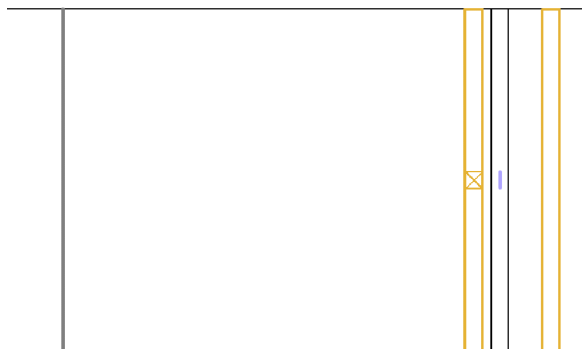
**Figure 3.1:** Diamond sensor sample mounted in a G10-made frame.



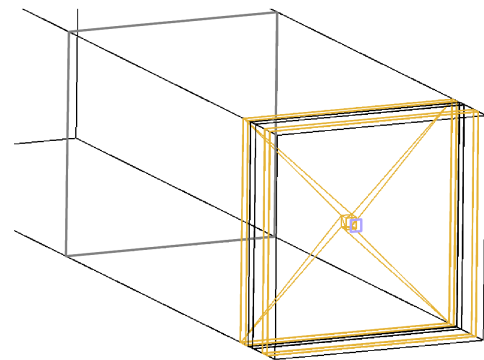
SETUP TESTRUN 2006 vers.2

04.05.2006

(a) Technical drawing of the testbeam setup



(b) GEANT 4 geometry, 2d projection



(c) GEANT 4 geometry, 3d view

**Figure 3.2:** Testbeam setup as (a) technical scheme and as geometry in the simulation, below, where the latter only shows edges of logical volumes. The beam enters from the left side. At the beam exit window (“Austrittsfenster”, grey in simulation) it passes from vacuum into air. The copper-made collimator cuts the beam size to the area of the sensor (“Probe”, blue in simulation). The sensor is housed in a light tight box of copper clad G10 material. The beam entry and exit windows of this box are made of 30  $\mu\text{m}$  thick polyimide foil covered with 1  $\mu\text{m}$  aluminium and are indicated as black lines in (b) and (c). A Faraday cup made of copper is placed behind the box.

electrons and the energy deposited per electron, the absorbed dose is obtained. Figure 3.2 shows a scheme of the arrangement in the beam path.

In preparation for this testbeam the setup had to be dimensioned. The goal was to optimise the geometry for efficient beam utilisation and concerning the measurement of quantities needed for the determination of the absorbed dose. One purpose of the simulations thus is to estimate the average energy deposition of electrons in the sensor bulk. Moreover, we have to evaluate which fraction of electrons potentially is backscattered from the Faraday cup or absorbed by the cup without traversing the sensor. This would affect the determination of the absorbed dose from the Faraday cup current.

The paths and the energy deposition of the electrons are simulated using the toolkit GEANT 4 [25]. This is an object oriented, C++ based library, providing classes and routines that can compute physics processes. GEANT 4 is a transport code to simulate the passage of particles through matter. The functionality ranges from the description of complex geometries and the tracking to the decays and the interactions of particles, according to physics models. Large sets of particles, elements and materials are offered. The models include electromagnetic, hadronic and optical processes over a wide energy range from keV to TeV. The tool is used and tested in various applications and validated by many experiments, as for example testbeam measurements.

On the basis of a code prepared by Kuznetsova [26] to simulate the measurement of the charge collection distance in the laboratory, I implemented the geometry of the testbeam using version GEANT 4.6.2. The  $z$  axis in this geometry is identical to the initial direction of the electrons in the simulation. Since several materials are located in the beamline between the beam exit window and the sample under test, electrons may be scattered or deflected. We had to estimate how many electrons are penetrating the sample, how to measure this as precise as possible and how we can control systematic errors in the experiment. Furthermore, the results of the simulation are needed for the determination of the totally absorbed dose. Each run is processed for  $10^5$  electrons.

## 3.2 Optimisation of the Geometry

First, the setup was optimised to use the beam efficiently. Due to scattering in the aluminium exit window of the beam pipe the electron beam is spread. Additionally it has to cover the distance from that point to the sensor through air, where the electrons also can be scattered. Hence a certain amount of electrons is missing the sensor. Figure 3.3 shows the trajectories of 10 MeV electrons downstream the beam exit window. At the sensor plane they are spread over an area larger than the sensor size.

A block of copper is positioned in front of the sensor box to shield the Faraday cup from electrons missing the sensor volume. The quadratic aperture of this collimator is adapted to the metallised area on the sensor surface. The simulation, visualised for one hundred electrons in Figure 3.4, showed that actually a thickness of 10 mm of copper is needed in order to ensure that electrons will not pass through. Only secondaries, generated by high energetic photons, appear behind the collimator bulk. For its outer dimensions

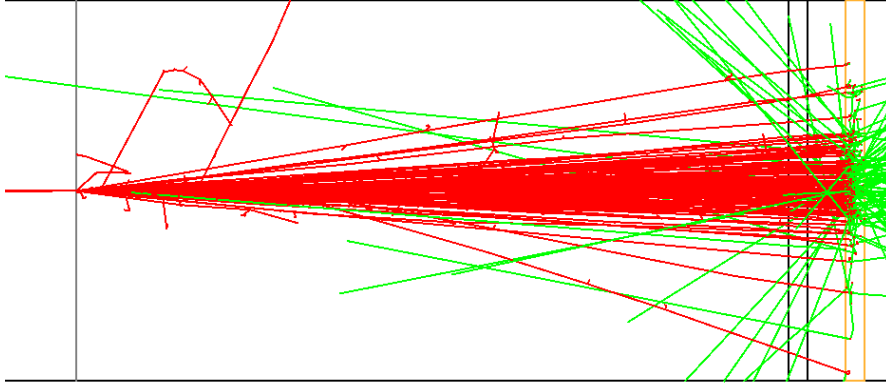


**Figure 3.3:** Simulated trajectories of 100 electrons with 10 MeV energy when crossing the aluminium exit window at the left side (red for  $e^-$ , green for  $\gamma$ ). See Figure 3.2 for the visualisation of the setup components.

30 mm  $\times$  30 mm are sufficient. Then, the number of primary electrons passing by the collimator is less than 1 %.

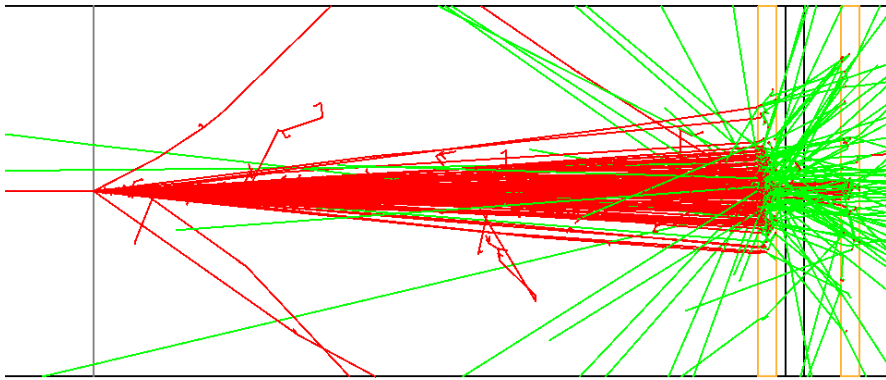


**Figure 3.4:** Like Figure 3.3 with an additional collimator of copper with 10 mm thickness. The collimator has a window aligned with the sensor face.

In the first layout, studied in Figures 3.3 and 3.4, the idea was to mount the setup on the accelerator facility (cf. Figure 3.2(a), “DALINAC-Kollimator”). For this configuration, the distance  $l$  between beam exit window and collimator was 370 mm. This led to a yield of only 10 % of the primary electrons hitting the sensor. Higher energies could improve the situation, e.g. for 50 MeV electron energy a yield of 80 % was achieved. However, due to limitations at the DALINAC, we fixed the energy to 10 MeV.

Another possibility for efficient irradiation of the sensor is to decrease the distance from the beam exit window. As main parameter the distance  $l$  between *exit window and collimator* was used since the arrangement of the collimator and the sensor box is fixed<sup>1</sup>.

<sup>1</sup>The additional pathway for electrons from the collimator upstream side to the sensor is nearly 20 mm.

A first step to reduce  $l$  was to lengthen the beam pipe, which brings the exit window closer to the sensor. Then the distance became  $l = 250$  mm. The result is depicted in Figure 3.5.

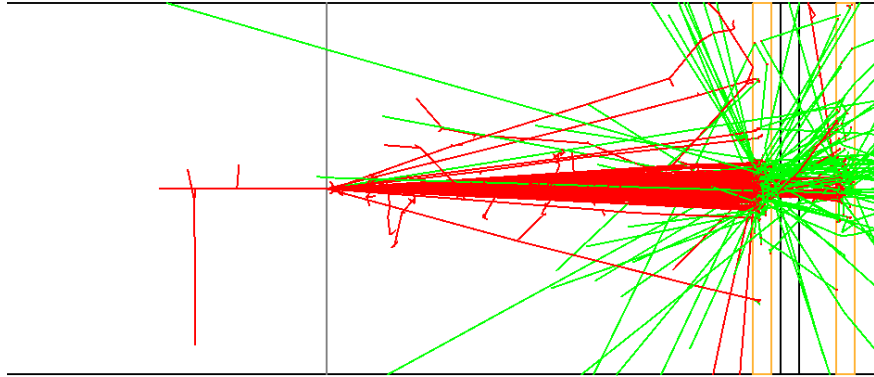


**Figure 3.5:** Like Figure 3.4 but with reduced distance between exit window and sensor.

As a second step, a special holding device for the sensor box was designed. It is installed on a table and adjustable in height and distance from the beam pipe. One has to bear in mind that the circularly spread beam is directed to a quadratic aperture in the collimator. A homogeneous spatial distribution of the electrons over the sensor area is desirable. The yield of beam electrons traversing the sensor is given in Table 3.1 for several geometries. According to this, the distance then was set to  $l = 80$  mm as a standard value.

Distance $l$	Fraction of primary electrons penetrating the sensor
140 mm	52 %
110 mm	65 %
80 mm	81 %
60 mm	90 %

**Table 3.1:** Yield from the beam depending on the distance from the beam exit window.

These values refer to the sensor region and do not depend on the size of the collimator window as soon as this is at least  $9 \text{ mm} \times 9 \text{ mm}$ . However, taking into account trigonometry the aperture should be slightly smaller than the sensor area (which is  $10 \text{ mm} \times 10 \text{ mm}$ ). Otherwise a large amount of electrons can hit the Faraday cup without penetrating the sensor. Table 3.2 shows that smaller holes reduce the yield from the beam and wider holes do not serve the purpose of the collimator. Consequently the size of the aperture was adjusted to  $9 \text{ mm} \times 9 \text{ mm}$ .

As an attempt to refine the counting accuracy even further and to reduce scattering effects at the collimator, the shape of the aperture was adapted to the projective geometry of the spread beam. This means that the size at its downstream side was kept as mentioned and the walls were formed projectively matching the angle of beam spread for 9 mm at collimator end position. That way no electrons can strike into the aperture walls and

Aperture size in collimator	Passing through the collimator	Penetrating the sensor	Missing the sensor
10 mm × 10 mm	88.1 %	81.1 %	7.0 %
9 mm × 9 mm	84.8 %	81.5 %	3.3 %
8 mm × 8 mm	79.7 %	76.6 %	3.1 %

**Table 3.2:** Influence of the collimator window on the fraction of electrons that pass through the collimator, penetrate the sensor and that do not cross the sensor but potentially contribute to the current at the Faraday cup. Above an aperture size of 9 mm × 9 mm more electrons miss the sensor, beneath that measurement less electrons traverse it.

thus most of them follow straight tracks through the sensor to the Faraday cup. However, the yield from the electron beam was somewhat reduced, as summarised in Table 3.3. Obviously the unbevelled planes act as a kind of lens focussing electrons to the sensor.

### 3.3 Measurement Accuracy

The number of electrons going through the sensor over time is counted as a current at the Faraday cup. There are several effects to be considered. Electrons are scattered off the cup, secondary electrons induced by photons in the collimator can reach it. For a Faraday cup thickness of 10 mm, the electrons cannot cross it. Nevertheless, if the size of the copper block in  $x$  and  $y$  is dimensioned according to the intercept theorems, electrons near the border can be scattered off transversely, as visualised in Figure 3.6. Then electrons are missing in the cup and thus the measured current is too low.

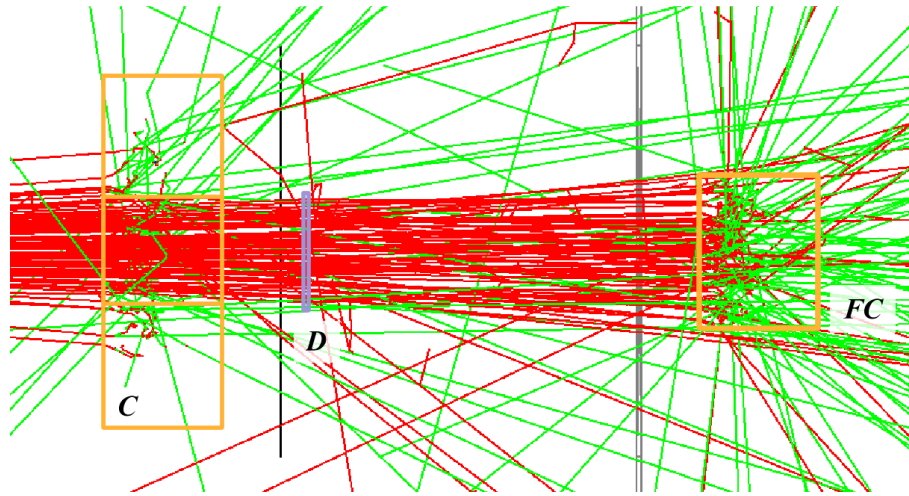


**Figure 3.6:** Zoomed view of the setup with a Faraday cup ( $FC$ ) of 13 mm × 13 mm, corresponding to the projection of rays being tangent to the sensor's borders. The geometries of the collimator ( $C$ ), the diamond sensor ( $D$ ) and the Faraday cup are shown. The outer  $x$ - $y$  dimensions of the collimator in this case are 30 mm × 30 mm.

In several runs with this projected cup size of  $13\text{ mm} \times 13\text{ mm}$  and different collimators the influence of the accessory material (foils, the sensor, housing) was investigated for given  $l$  and aperture size. The sensor volume close behind the collimator always is penetrated by the same fraction, and these incoming electrons are directed to the Faraday cup. They can be deflected from this direction during the passage through the material layers of the diamond and the sensor box windows, which means a wider beam spread. A fraction of about 9% does not reach the cup compared to the case without all the accessories. This means a considerable deviation of the Faraday cup current. After all, this fraction did not vary when changing the collimator dimensions.<sup>2</sup> However, the scattering in the sensor box, especially the direction of the scattered electrons, is affected by the beam spread and the collimator aperture. Hence, the number of electrons absorbed in a Faraday cup with projected size might vary strongly when changing  $l$  or the aperture. For the sake of reproducibility the influence of such scattering effects should be minimised.

By increasing the Faraday cup size beyond the trigonometrically postulated dimensions, the number of absorbed electrons rises. An extension of at least 7 mm in  $x$  and  $y$  is needed in order to retain electrons within the cup that approach on a path straight through the outer rim of the sensor. Above that size, a constant fraction of about 3.5% of the electrons entering the Faraday cup volume is scattered off again. A few of them are compensated by electrons that reach the cup although they never met the sensor. These electrons are produced as secondaries in the collimator or diffracted from their track through the sensor.

The only way to handle these effects is to correct for them and assigning the uncertainty of the correction as a systematic error. As mentioned above, the off-scattering rate nearly stays constant for a cup size of  $20\text{ mm} \times 20\text{ mm}$  or larger. The more the cup is enlarged above that, the more electrons flying around can be captured. Using  $10^5$  primary electrons the statistical uncertainty of this rate in simulations under fixed settings is at the per mille level. As a measure with which the current at the Faraday cup reproduces the number of electrons penetrating the sensor, the ratio

$$R = \frac{e^- \text{ absorbed in the cup}}{e^- \text{ penetrating the sensor}}$$

is considered. It becomes independent of other parameters for a Faraday cup with dimensions of  $40\text{ mm} \times 40\text{ mm}$ . As can be seen from Table 3.3, neither an excessively expanded collimator nor the shape of its aperture can influence that value as well as the components of the sensor box. Even a change of the distance  $l$  does not affect this result in a range of 60 to 120 mm. Of course, the yield from the electron beam is much higher at shorter distances.

$R$  is constant within the relevant range for the important geometry parameters  $l$  and the collimator aperture. A higher fraction of electrons is scattered off the Faraday cup than captured from trajectories bypassing the sensor. The number of electrons penetrating the sensor in a measured time interval is by 2% larger than what we measure as a current at

---

<sup>2</sup>Even in case of omitted collimator the number of electrons absorbed in the cup was reduced by just 9% in presence of the sensor box material.

Setup parameters	Passing through the collimator	Penetrating the sensor	$R$
Collimator dimensions (thickness / exterior / interior) in mm			
10 / 30 × 30 / 9 × 9	84 %	82 %	0.98
10 / 30 × 30 / projective	81 %	80 %	0.98
20 / 40 × 40 / 9 × 9	85 %	82 %	0.98
20 / 40 × 40 / projective	80 %	79 %	0.98
Distance from the beam exit window, $l$ , in mm			
110	68 %	65 %	0.98
80	86 %	81 %	0.98
60	92 %	90 %	0.98

**Table 3.3:** To evaluate how the number of electrons in the sensor depends on the Faraday cup current, the ratio  $R$  is calculated. The Faraday cup has a fixed size of 40 mm × 40 mm. The aperture width at the downstream side is 9 mm × 9 mm—only the shape was modified.

the cup. This has to be taken into account as a correction factor. Since the correction is small its systematic uncertainty was neglected.

The setup finally used for the testbeam at the DALINAC is shown in Figure 3.7. For the distance between the beam exit window and the collimator,  $l = 70$  mm was chosen. The size of the collimator is 70 mm × 70 mm with a thickness of 10 mm and a non-projective aperture of 9 mm × 9 mm. The Faraday cup dimension are 10 mm in  $z$  and 40 mm × 40 mm in the transverse plane.

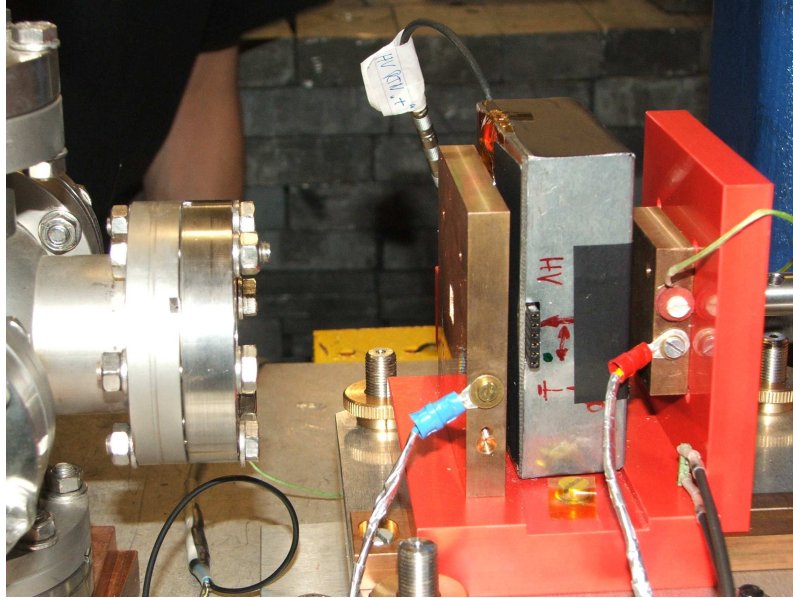


**Figure 3.7:** Testbeam setup used at the DALINAC accelerator. On the left side the end cap of the beam pipe can be seen. The sensor box is placed between the collimator and the Faraday cup at the holding device on the right hand side.

## 3.4 Energy Deposition

### 3.4.1 pCVD Diamonds

In order to calculate the totally absorbed dose we need the average energy deposit per incoming particle. The simulation program sums up the deposits of all “hits”<sup>3</sup> in one “event”. Such an event is processed for each particle injected by the generator and traces completely its full path. This means that also penetrations from backscattered electrons, meeting the sensor twice, or secondaries, traversing it non-perpendicularly, are treated. All hits occurring in this event are assigned to the primary electron. A hit can only be registered in a so-called sensitive detector which here is solely the diamond sensor. The spectrum of energies deposited in the diamond material is shown in Figure 3.8 for  $10^5$  primary electrons.

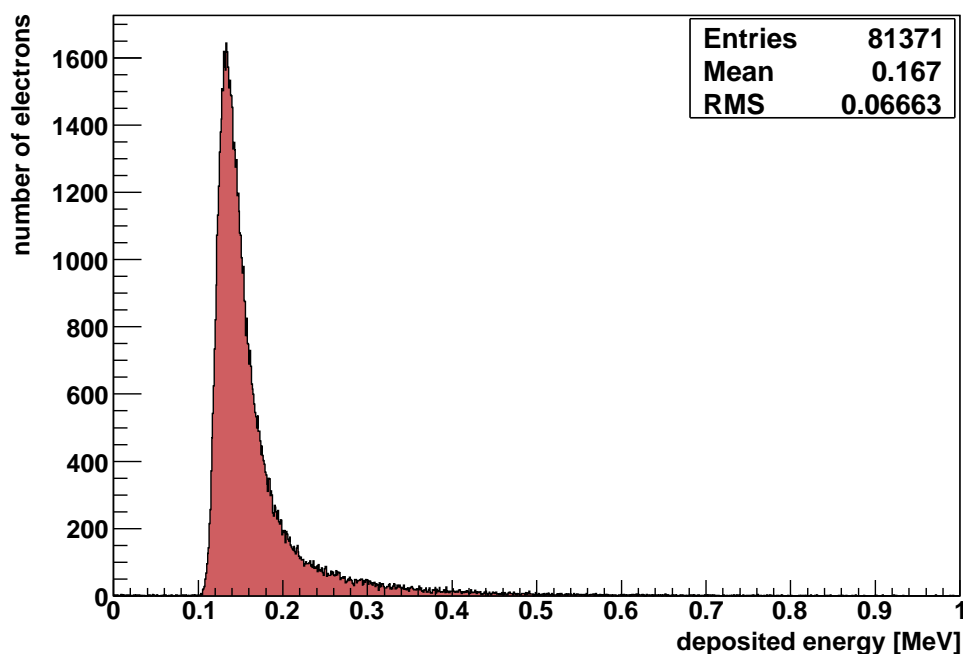


**Figure 3.8:** Spectrum of the energy deposits from 10 MeV electrons in  $300\ \mu\text{m}$  of diamond. “Entries” gives the number of primary electrons out of  $10^5$  that deposit energy in the sensor.

As the mean value for the final setup  $\overline{E_{dep}}(Di) = 167.0\ \text{keV}$  was obtained. This value is slightly higher than the theoretical result<sup>4</sup> for the average energy deposition of a MIP in  $300\ \mu\text{m}$  diamond, which is  $164.4\ \text{keV}$  [27]. The reasons are trajectories traversing the sensor at an angle, multiple scattering and the dependence of the deposits on the particle energy after Bethe-Bloch.

---

<sup>3</sup>A hit is stored in case that a minimal amount of energy is deposited during the passing of a particle through the material. Then the deposits,  $dE/dx$ , of every single computing step are summed up for one complete passage.

<sup>4</sup>Calculated after Bethe-Bloch formula, including corrections.

### 3.4.2 Silicon

Just by replacing the material filling the sensor volume the same study was done for silicon as sensitive material. In general, silicon is well understood for detector applications and, of course, it is much cheaper than diamond and could be an alternative.

Here, an average energy deposition of  $\overline{E_{dep}}(Si) = 106 \text{ keV}$  was found. It deviates by 2.35 keV from the theoretical value of 103.65 keV per 300  $\mu\text{m}$  silicon for a MIP.

## 3.5 Results of the Testbeam

We measured the performance of diamond samples from Element Six Ltd., UK, and the Fraunhofer Institute for Applied Solid State Physics, Germany, in July 2006. For the most samples we found the charge collection distance increasing at irradiation up to doses of about 1 MGy. This effect is called pumping as trapping centres in the diamond are filled with electrons. For very high doses above 1.5 MGy the charge collection distance decreases like in Figure 3.9(a) but all sensors were still operational after the irradiation. Both the current-voltage characteristics and the charge collection distance as a function of the applied electric field in Figure 3.9(b) showed the same behaviour as before the irradiation. Just a little increase of the current value is observed afterwards whereas the charge collection distance drops down to approximately 20 %. By pumping, i. e. irradiating the sample with doses of the order of Gy immediately before the measurement, this loss can be recovered almost completely. The results of the testbeam [28] were presented at the Nuclear Science Symposium of the IEEE Conference in San Diego in November 2006.

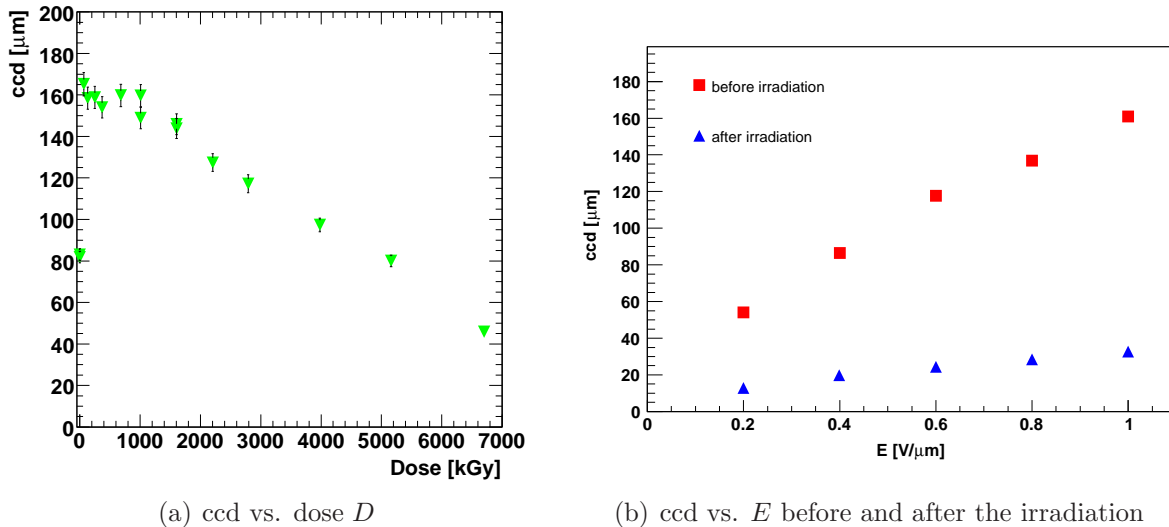


**Figure 3.9:** The performance of a diamond sample from Element Six<sup>TM</sup>. In (a) the dependence of the charge collection distance (here denoted as ccd) on the absorbed dose is plotted. The sample was irradiated up to 7 MGy. The charge collection distance as a function of the applied electric field  $E$  is shown in (b) before and after the irradiation.

# Chapter 4

## Background in the Silicon Tracking Detectors of the LDC

### 4.1 Simulation of the Pair Background

The tracks and the showers of particles in a detector must be registered for the purpose of particle identification and event reconstruction. Simulation tools for interesting physical and background processes are developed to understand the performance of a designed detector, or for the implementation and optimisation of reconstruction algorithms. A special linear collider input/output framework (LCIO) is used as a basis to describe both experimental data and simulated event samples generically for linear collider studies. Input parameters define the initial conditions in a simulation and refer to the technologies employed in accelerators and detectors.

The simulation of such a complex system like the ILC detector is processed in different stages. The first stage is the generation of events in the beam-beam interaction. The propagation of the created particles and their interaction with the detector material are simulated according to their properties, e.g. the charge or the energy. The simulated data afterwards is reconstructed and analysed using the same tools as for real data. It is described in the following how these stages were realised for this work.

#### 4.1.1 Simulation of Bunch Crossings

For the first stage, namely the simulation of certain processes in the colliding beams, Monte Carlo generators are developed. The background from the collision of bunches of electrons and positrons, essentially this means the beamstrahlung and the resulting pairs, is simulated by the program GUINEA-PIG [9]. The beam parameters given in Table 2.1 are used for the simulation of the bunch crossings. For a chosen accelerator and beam parameter set, GUINEA-PIG delivers the particles and their four-momenta generated in beam-beam interaction. This information subsequently is feeded into a detector simulation.

### 4.1.2 Full Detector Simulation

The full detector simulation for the ILC is performed using the GEANT 4-based program MOKKA.

MOKKA mainly provides the geometry of the detector components and transports the particles through the material of the sub-detectors. In order to use MOKKA flexibly, for instance for different geometry options, the sub-detectors are implemented in separate drivers. This code does not contain the values of variable parameters but describes the structure only in principle. All the values of the dimensions and positionings as well as further parameters such as the material are collected in a MySQL [29] database for the relevant options and versions.

In sensitive materials, the interactions and depositions of traversing particles are registered. The physics processes considered for the interactions and decays are defined in a so-called physics list<sup>1</sup>. For example for electrons, this includes multiple scattering, ionisation, bremsstrahlung, and a hadronic model for electron-nuclear processes. Cuts are applied at low energies to regulate the precision and the computing efficiency, respectively.

MOKKA simulates energy deposits in the sub-detectors stored in LCIO format. Moreover, the crossings of particles not depositing energy through arbitrary detector segments can be recorded on simulation level.

### 4.1.3 Analysis and Reconstruction

LCIO is a persistency framework that provides container classes to accumulate data for linear collider studies in a compressed format. It facilitates the communication between the processing stages of the simulation. As the structure is object-oriented, the user can utilise the framework to implement applications for both writing and reading data. However, the classes and routines of this library offer just an elementary functionality.

Some basic tools are already available in MARLIN<sup>2</sup>. This is another simple and generic framework that gives access to LCIO collections and offers extension classes and precast functions. For particular tasks individual processors can be implemented by the user. The executable program is built up modularly and allows to call each desired processor arbitrarily, passing parameters via a steering file. The extracted information can be interpreted with common analysis tools.

## 4.2 Analysis of the Simulated Event Samples

GUINEA-PIG-generated  $e^+e^-$  pairs are processed through MOKKA<sup>3</sup> and analysed by MARLIN processors to extract the information related to the sub-detectors under investigation.

---

<sup>1</sup>The current event samples are based on the GEANT 4 built-in physics list QGSP\_BERT\_HP. It provides a mature model for processing neutrons.

<sup>2</sup>Artificial word for Modular Analysis and Reconstruction for the LINear collider.

<sup>3</sup>The processing of 100 bunch crossings for several machine and detector options was prepared and performed by Adrian Vogel.

Hit positions and times, energy deposits, and the particles generating them are considered with the data analysis framework ROOT [30].

### 4.2.1 The Vertex Detector

The vertex detector (VXD), the innermost part of the tracker system described in Section 2.3.3, is positioned very close to the interaction point. Its task is the determination of the primary vertex and to measure secondary vertices of short living particles. For these purposes, a spatial resolution in the  $\mu\text{m}$  range is needed. The sensors are silicon pixel devices with a pixel size of  $20 \times 20 \mu\text{m}^2$  and a thickness of only  $37.44 \mu\text{m}$ . In such a thin layer, the multiple scattering is low, which is necessary for extrapolating the tracks to the vertex. Under ideal conditions, one would only record the hits from primary particles and each event would be perfectly reconstructed. However, beamstrahlung pairs will add background hits. To ensure a high reconstruction efficiency, the level of spurious tracks from this background needs to be low. Figure 4.1 shows a schematic view of the VXD, the details of the geometry are given in Table 4.1.

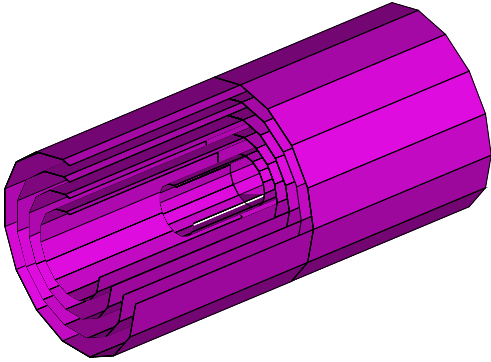


**Figure 4.1:** Artistic picture of the vertex detector.

Layer	$r$ [mm]	$z/2$ [mm]	$u$ [mm]	$\vartheta$ [deg]
1	15	50	94.3	16.70
2	26	125	163.4	11.75
3	38	125	238.8	16.91
4	49	125	307.9	21.41
5	60	125	377.0	25.64

**Table 4.1:** Geometric dimensions of the VXD layers;  $r$  is the radius,  $z$  the cylinder height,  $u$  the circumference and  $\vartheta$  the smallest covered polar angle.

#### 4.2.1.1 Total Hit Occupancy from Background

In a first step the density of hits<sup>4</sup> in the sensors is investigated. The number of hits per area per 100 BX, denoted hereafter as occupancy, gives information about the accumulation of background hits. The position of a hit is the centre between entry and exit point of a particle track through this sensor. Figure 4.2 shows the total hit occupancy in VXD Layer 1 due to beamstrahlung remnants. In the figure, the cylindrical layer is rolled out to a plane. In this plane it is characterised by the  $z$  coordinate of the LDC detector at the abscissa and the properly calculated azimuth angle  $\varphi = \arctan \frac{y}{x}$  at the ordinate. Note

---

<sup>4</sup>A hit is recorded if an energy deposit above the threshold of 20% of a MIP deposit arises during the passage through a sensitive material.

that the dots in this scatter plot do not show one hit, each, but merely represent the spatial distribution of the hit density.

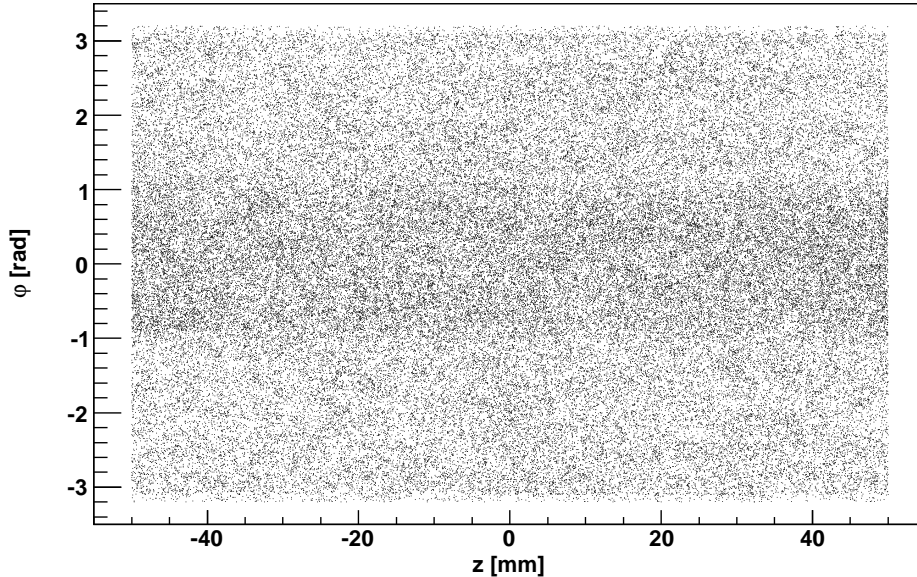


**Figure 4.2:** Scatter plot of the total hit occupancy for 100 BX in the innermost layer of the vertex detector. The parameters of this event sample are 20 mrad crossing angle, a solenoidal magnetic field and the *Tesla* beam parameter set for  $\sqrt{s} = 500$  GeV.

The hit occupancy lacks any information about energies or the size of the deposits. Nevertheless it is very helpful for the estimation of the flux of charged particles. The plot in Figure 4.2 for example, shows a clear inhomogeneity for the  $\varphi$  coordinate. This effect is explained further on.

#### 4.2.1.2 Geometric Projection

Searching for spatial inhomogeneities of the energy deposition density, one should remind the symmetric construction of the detector. It is mirrored at the  $z = 0$  plane and the cylindrical detectors are positioned concentrically round the detector axis. The axis labels for the VXD layer in Figure 4.2 reflect this symmetry and suggest to consider the data just from the perspective of the beam and also perpendicular to it. For the  $z$  projection a one-dimensional histogram is filled independently of the  $\varphi$  coordinate. The same can be done for the  $\varphi$  projection which is basically the view of the beam, even if a crossing angle is applied. In Figure 4.3 the occupancy of VXD Layer 1 is shown as projections to the  $z$  and  $\varphi$  axis, respectively.

In Figure 4.3(a) one can see that the total occupancy in the first VXD layer does not depend on the  $z$  coordinate. In contrast the  $\varphi$  projection in Figure 4.3(b) shows a conspicuous enhancement around  $\varphi = 0$ . There are two sharply zoned regions with distinct levels of hit population. This is surely not desirable since the track reconstruction

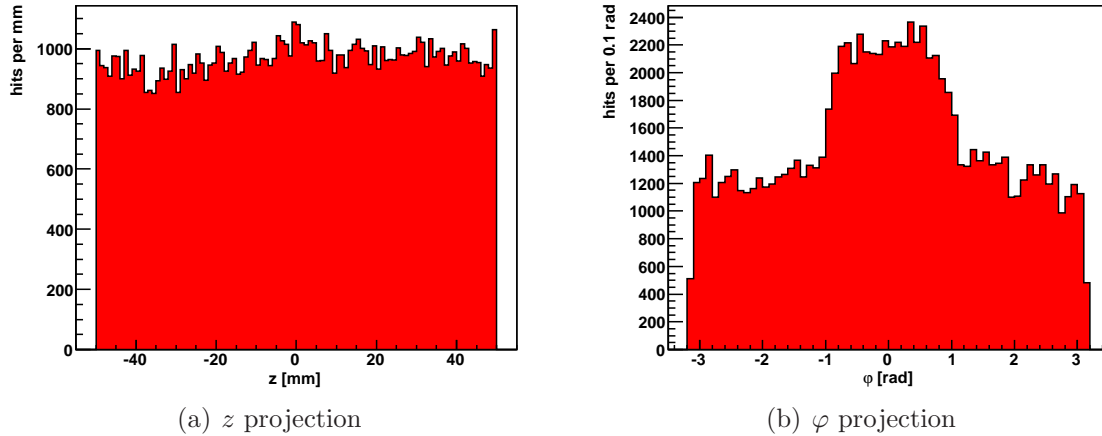


**Figure 4.3:** The occupancy for 100 BX like in Figure 4.2, in (a)  $z$  and (b)  $\varphi$  projection.

performances will be different in this regions. The reason is explained later and should be eliminated if possible.

#### 4.2.1.3 Time Separation

Although the particles mainly move with almost speed of light, they have to travel a macroscopic distance of  $d = 3.5$  m from the IP to the BeamCal<sup>5</sup> and back again. The path length of 7 m corresponds to a time of flight of at least  $t = 2d/c \approx 23$  ns which is a measurable quantity. Plotting the time distribution of all the vertex detector hits, as shown in Figure 4.4, two peaks become visible. The first near  $t = 0$  originates from particles generated at the IP. The second peak above 23 ns stems from particles backscattered from the BeamCal.

Upon closer inspection one can see a double peak structure in the hits from backscattered particles. The second maximum rising at approximately 27 ns very close to the first one corresponds to a distance of 4.05 m from the IP. This is exactly the distance of the final quadrupole magnet,  $L^*$ . A noticeable fraction of secondary hits is produced by particles scattered off the final quadrupole.

To reduce the occupancy, it might be considered to cut off the backscatter hits. The reduction of background hits would amount to approximately 30 %.

The occupancy distributions as shown in Figure 4.3 are now repeated for hits arriving before 23 ns, called hereafter “immediate hits”, and for hits arriving after 23 ns, called “secondary hits”. The result is shown in Figure 4.5. Immediate hits are represented by a red bin content and hits later than 23 ns after bunch crossing by a blue one, respectively. The plots are overlaid, the bars for both types are filled starting from zero ordinate value.

The relatively flat distribution of hits as a function of the  $z$  coordinate in Layer 1, cf. Figure 4.3(a), arises only in sum of all hits. In Figure 4.5(a) one can see the non-uniform

<sup>5</sup>Actually the pairs reach the graphite absorber at  $z = 3500$  mm, which is considered as part of the BeamCal device. In the baseline design the graphite thickness is 50 mm.

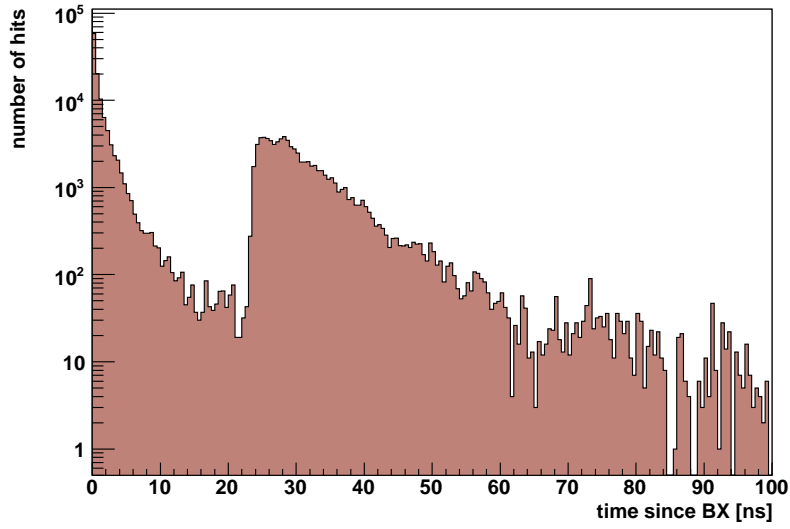


**Figure 4.4:** Distribution of VXD hits as a function of time. The bunch crossing occurs at  $t = 0$ . Note the logarithmic scale at the ordinate. Parameters are the same as in Figure 4.2.

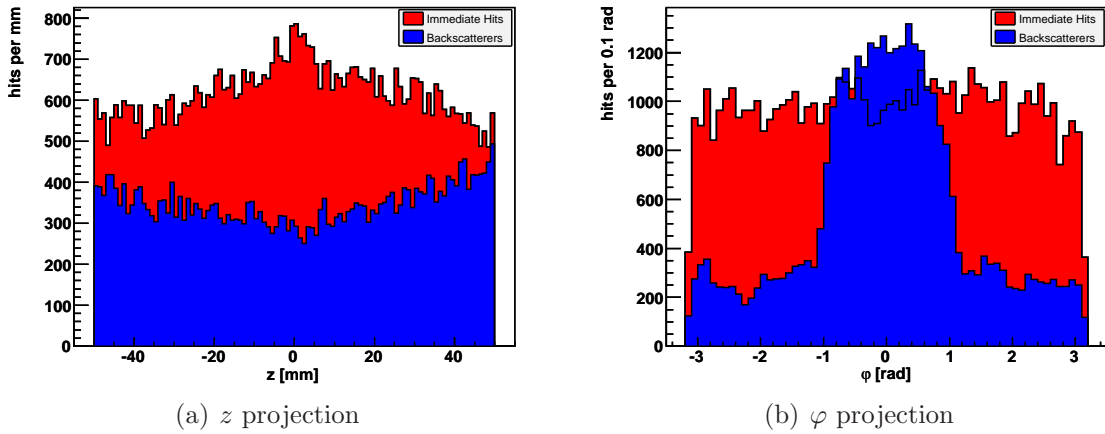


**Figure 4.5:** Time separation applied to the projections of the occupancy in Figure 4.3. Immediate hits are represented by red bars, secondary hits, caused by particles arriving 23 ns after the bunch crossing, are blue.

behaviour for both immediate and secondary hits that compensate in the sum.

Similarly, from the  $\varphi$  projection in Figure 4.5(b) it becomes clear that the enhancement in the  $\varphi$  distribution is caused by backscattered particles only. In this special case it can be attributed to the DID field. This matches the incoming beams and thus guides pairs with small  $p_t$ , curling around the magnetic field lines, from the IP to the incoming beam pipe. They are scattered at the wall of the tube and lots of low energetic particles again leave the beam pipe directed to the IP. It turned out that the field map for this setup is not optimised yet. A large amount of backscattered particles with nearly zero  $p_t$  does not meet the small beam pipe diameter at IP position but reaches it with a little shift to positive  $x$  values. Then the centre of this stream scattered off the incoming beam pipe crosses the  $z = 0$  plane at  $y = 0$  and  $x > 0$ . With the current  $x$  shift, that is, the particles smash into the innermost VXD layer at values around zero for  $\varphi = \arctan \frac{y}{x}$ .

#### 4.2.1.4 Comparison between the VXD Layers

The LCIO information of the VXD Layers 2 to 5 are processed the same way. The layers are distinguished simply by their number. These four outer layers have a uniform length of  $z = 250$  mm and a circumference,  $u$ , growing with the layer number, cf. Table 4.1. Since the layer surfaces are depicted in dependence on the azimuth angle  $\varphi$ , they have equal numbers of bins in this quantity.

The five VXD layers cover a similar latitude angle range. Nevertheless the occupancy diminishes at larger radii, as can be seen in Figure 4.6. Two effects are responsible: Firstly, charged particles curl around the magnetic field lines with a helix diameter depending on the transverse momentum  $p_t$ . If they start from the  $z$  axis, which should be true at least for the immediates, they will hit each layer within this diameter. That means both the electron reaching Layer 4 and the one reaching Layer 2 will penetrate the Layers 1 and 2 but only the former will also penetrate the Layers 3 and 4. Secondly, the number of pairs becomes very small for larger transverse momenta. The minimum for electrons to reach the VXD is  $p_t \approx 9 \cdot 10^{-3}$  GeV/ $c$ . The  $p_t$  distribution for IPC pairs has its maximum at approximately  $6 \cdot 10^{-4}$  GeV/ $c$  and drops rapidly to larger values and likewise the polar angle distribution does.

In Figure 4.6(b) another structure can be found. A peak arises in the occupancy of Layer 5 and to a lesser extend also for Layer 4 and 3. As before the reason is the DID field. High energetic beamstrahlung pairs from the IP move downstream almost not influenced by the magnetic field. Those with a small polar angle  $\theta$  smash into the BeamCal around the outgoing beam pipe or the tube itself. A stream of low energetic particles is formed by backscattered pairs and secondaries leaving the outgoing beam pipe towards the IP. As the distance between the tubes at BeamCal position is  $x_{io} = z_{BC} \cdot \tan \theta_x = 70$  mm, these particles, moving along the DID field lines, reach the  $z = 0$  plane at  $x \approx 70$  mm near the outermost VXD layer.

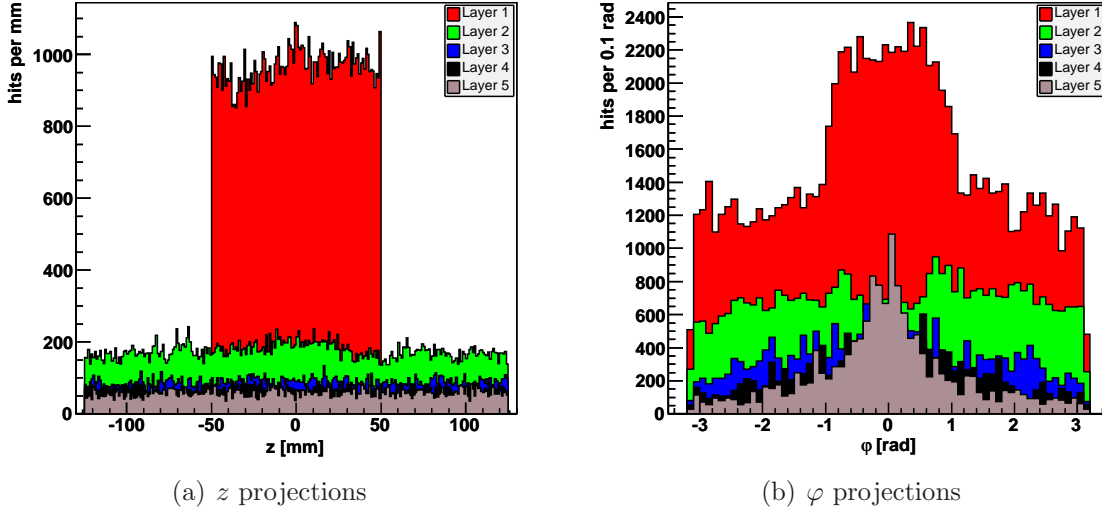


**Figure 4.6:** Comparison of the occupancies of the five VXD layers, again represented in (a)  $z$  and (b)  $\varphi$  projection. Note that Layer 1 is shorter in  $z$ . Parameters are the same as in Figure 4.2.

#### 4.2.1.5 Estimation of the Absorbed Dose

Obviously the innermost VXD layer suffers most from the Background fluxes. Hence it suggests to investigate this layer in particular in terms of the absorbed radiation dose. The LCIO collection also contains the deposited energy of each hit.<sup>6</sup> In Figure 4.7, the spectrum of these deposits in the innermost layer is represented. The plot in Figure 4.7(a) resolves the spectrum logarithmically in order to show the distribution over the entire range. The cut at lower energies is made by MOKKA at 20% of the deposition from a minimal ionising particle in silicon. The maximum arises close to the MIP position. For higher energies the number of hits drops slowly and deposits of up to 1 MeV occur.

The mean value of the deposited energies must be calculated from a linear scale in the distribution. The result for Layer 1 gathered from Figure 4.7(b) is  $\overline{E_{\text{dep}}} = 23.17$  keV. This is almost twice the theoretical value of 12.94 keV for a MIP in 37.44  $\mu\text{m}$  of silicon. Reasons for this deviation are mainly the effective path length of particles not traversing perpendicularly as well as the energy dependence of  $dE/dx$  as given by the Bethe-Bloch formula.

Having estimated the total energy deposit in the sensor,  $E_{\text{dep}}$ , one can calculate the absorbed dose. The dose absorbed in matter is defined as deposited energy over mass  $m$ . In case of known mass density,  $\rho$ , one can substitute the volume for the mass using  $m = \rho V$ :

$$D = \frac{E_{\text{dep}}}{m} = \frac{E_{\text{dep}}}{\rho \cdot V} . \quad (4.1)$$

<sup>6</sup>In fact a hit is only stored in the collection in case that a minimal amount of energy is deposited during the traversing of a particle. Then the deposits,  $dE/dx$ , of every single computing step are summed up for one complete passage through the sensitive material.

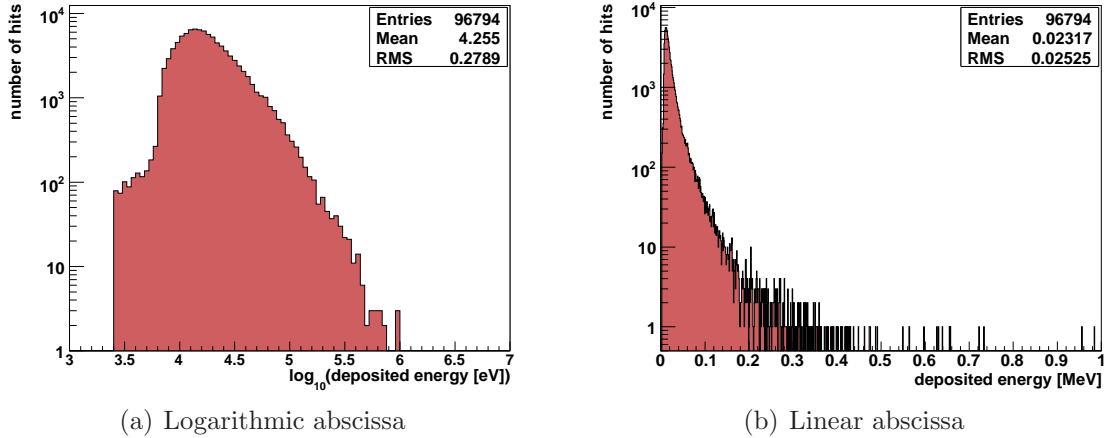


**Figure 4.7:** Spectrum of the energy deposits in VXD Layer 1. In (a) the abscissa gives the order of magnitude based on electron volt to resolve the entire spectrum logarithmically. In (b) the linear distribution is plotted to obtain the correct mean value that is written in the statistics box at the top right corner.  $\overline{E}_{\text{dep}} = 23.17 \text{ keV}$  in this example. Note that the ordinate is logarithmic in both plots. Parameters are the same as in Figure 4.2.

In order to see the spatial distribution of the dose, the surface of Layer 1, depicted like in Figure 4.2 on page 36, is subdivided into bins of  $5 \text{ mm} \times 5 \text{ mm}$  in the azimuthal arc,  $u$ , and the  $z$  coordinate. This seems a reasonable resolution for the discussion of the background. With the sensor thickness denoted as  $dr$ , the volume in equation (4.1) is expressed by the element of extension,  $dV = du dz dr$ .

The luminosity in the form (2.5) depends on machine parameters, in particular it contains the beam geometry. On the other hand, these parameters after equation (2.6) determine the energy loss due to the pinch effect and therefore also the amount of the beamstrahlung remnants per bunch crossing. In this manner, the amount of the background scales with the considered integrated luminosity  $L$ . The number of bunch crossings in the specified run period  $\Delta t$  can be calculated using (2.4):

$$\Delta t \cdot f_b = \frac{L}{\mathcal{L}} \cdot f_{\text{rep}} \cdot n_b . \quad (4.2)$$

Taking the simulated deposits as a starting point, one can project from 100 BX in the event samples to the totally absorbed electromagnetic dose in  $500 \text{ fb}^{-1}$ . First, the data have to be normalised to a single bunch crossing accounting for different beam parameters. The energy deposited per BX is denoted as  $E_{\text{dep}}^b$ . Then the dose (4.1) is obtained from

$$D = \frac{E_{\text{dep}}^b}{\rho_{\text{Si}} \cdot dV} \cdot \frac{500 \text{ fb}^{-1}}{\mathcal{L}} \cdot f_{\text{rep}} \cdot n_b . \quad (4.3)$$

The mass density of silicon is  $\rho_{\text{Si}} = 2.33 \text{ g cm}^{-3}$ . The space element where the energy is deposited is approximated by  $dV = du dz dr$  such the circumference has the same number

of segments for each layer and hence the bin size grows with the layer number.  $d\varphi$  is chosen to obtain  $du \approx 5$  mm in the first layer.<sup>7</sup> As can be seen in Figure 4.6(b), the flux decreases strongly to the outside and the occupancy becomes smaller despite of the larger  $du$ . The  $z$  segmentation is  $dz = 5$  mm for all layers, the sensitive silicon is  $dr = 37.44 \mu\text{m}$  thick. The machine parameters of the *Tesla* beam set are specified in Table 2.1 on page 22. Measuring the deposited energy in Joule  $D$  is obtained in Gy.

Using the simulations for VXD Layer 1, this procedure leads to Figure 4.8 where the colour scale is given in kGy. The maximum of 3 kGy is already the worst case for the options under consideration.

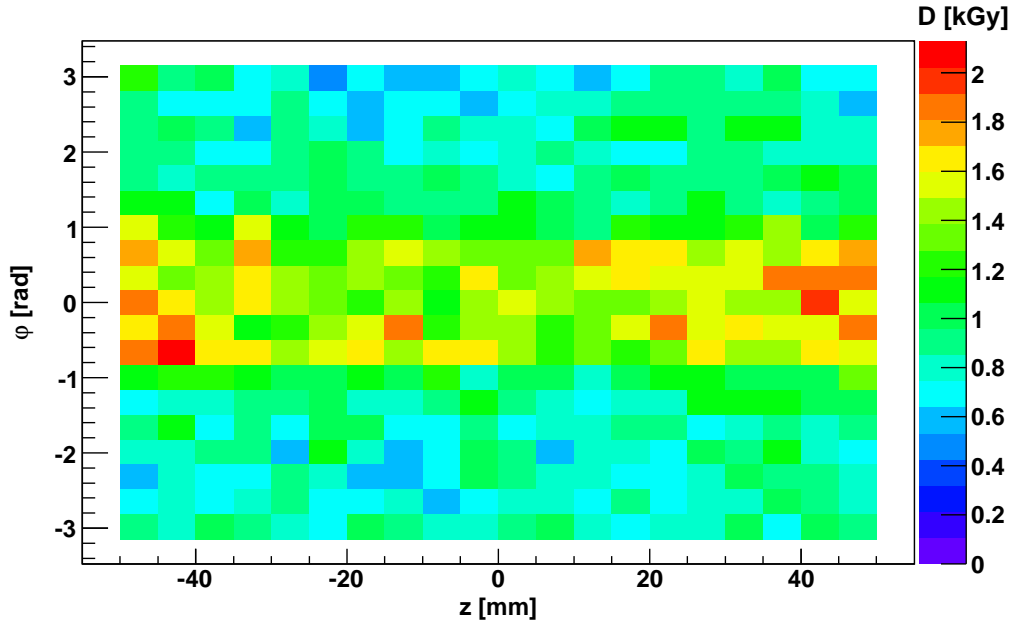


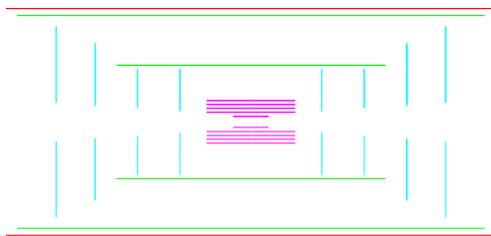
**Figure 4.8:** The electromagnetic dose absorbed in Layer 1 of the VXD for an integrated luminosity of  $500 \text{ fb}^{-1}$ . The color scale is given in kGy on the right side. The spatial distribution is resolved by bins that represent surface elements of  $5 \text{ mm} \times 5 \text{ mm}$ . Parameters are the same as in Figure 4.2.

## 4.2.2 The Silicon Intermediate Tracker

The radius of the outermost layer of the vertex detector is  $r_5 = 60$  mm. The sensitive volume of the encompassing TPC starts at the inner radius of  $r_i = 386$  mm. The resulting gap is bridged by means of two additional layers of silicon strip detectors, called silicon intermediate tracker, SIT. These are cylindrical layers with radii of 160 mm and 300 mm, respectively. In Figure 4.9 a schematic view of the  $x = 0$  plane is given to show the sizes coverage of the SIT (green) compared to the VXD (purple). The sensitive material has

<sup>7</sup>The exact value of  $du$  in Layer 1 is  $2\pi r_1/19 = 4.96$  mm.

a thickness of  $300\ \mu\text{m}$  and is mechanically much robustier than the extremely thin VXD sensor. Their task is to link the TPC tracks to hits acquired from the VXD.



Layer	$r$ [mm]	$z/2$ [mm]	$u$ [mm]	$\vartheta$ [deg]
1	160	380	1005.3	22.83
2	300	660	1885.0	24.44

**Table 4.2:** Geometric dimensions of the SIT layers;  $r$  is the radius,  $z$  the cylinder height,  $u$  the circumference and  $\vartheta$  the smallest covered polar angle.

**Figure 4.9:** Scheme of the  $y$ - $z$  cross section through the silicon trackers at  $x = 0$ . The intersection lines of the SIT layers with this plane are drawn in green, the dimensions are given in Table 4.2. The purple lines show the VXD layers, cf. Figure 4.1. The outer red lines mark the inner radius of the interior insensitive wall of the TPC barrel. The vertical light blue lines indicate some of the forward tracking discs.

#### 4.2.2.1 Total Hit Occupancy from Background

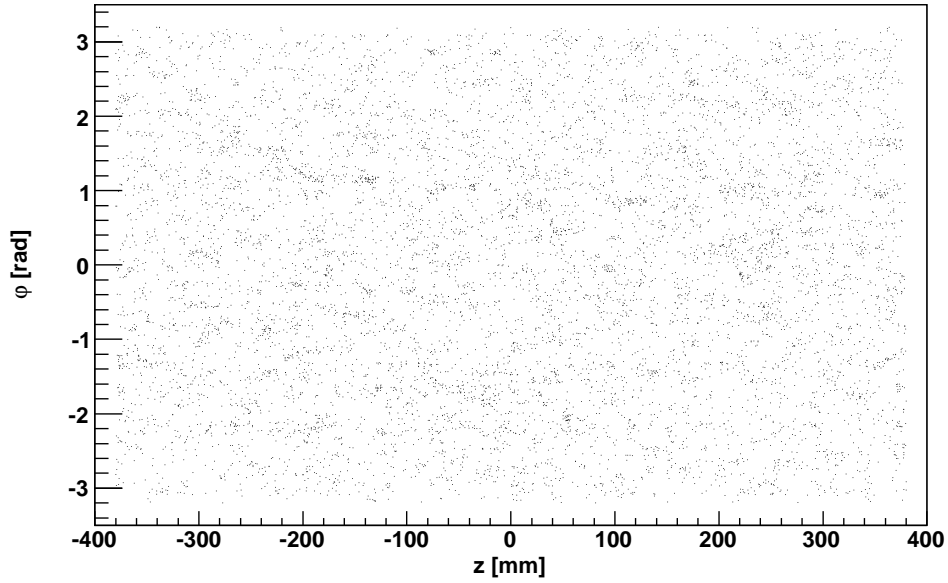
The hit occupancy in the SIT layers is represented similarly to the VXD layers. Again the cylindrical tubes are rolled out, thence a  $z$ - $\varphi$  distribution is obtained. This can be projected onto the  $z$  and  $\varphi$  axis, respectively, as before. The corresponding plots are shown in Figure 4.10 for the inner SIT layer.

Although the  $z$  projection is subdivided into bins of 10 mm the number of hits is much smaller than for the VXD. Both layers cover polar angles between the ranges of VXD Layers 4 and 5.

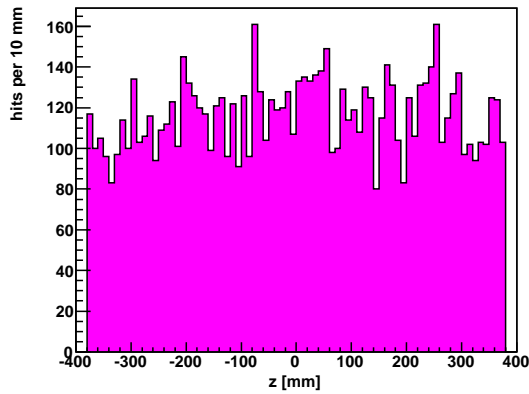
#### 4.2.2.2 Time Separation

The effective path length of particles to reach the SIT after being scattered off the BeamCal is a bit less than in case of the VXD. The distance of  $2d = 7\ \text{m}$  must be reduced by half the  $z$  length given in Table 4.2 for the respective layer. One obtains a corresponding time of  $t = \frac{2d-z/2}{c} \approx 22\ \text{ns}$  for Layer 1 and another nanosecond less for Layer 2. The time distribution of hits in Layer 1, shown in Figure 4.11, confirms this calculation.

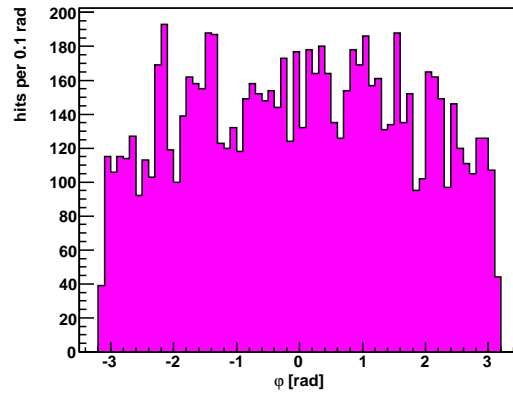
Separating the projected occupancies in Figures 4.10(b) and 4.10(c) results in similar plots as for the VXD, see Figure 4.12. Again the bars for immediate hits are filled in red and those from backscattered particles are blue. Note that, in contrast, the secondary hits clearly form the largest fraction of all hits here. Hence the red bars are drawn in front of the blue ones.



(a)  $z$ - $\varphi$  distribution



(b)  $z$  projection



(c)  $\varphi$  projection

**Figure 4.10:** Total hit occupancy for 100 BX in the inner layer of the silicon intermediate tracker. The parameters are 20 mrad crossing angle, a solenoidal magnetic field and the *Tesla* beam parameter set for  $\sqrt{s} = 500$  GeV, cf. Section 4.2.1. In subfigures (b) and (c) the projections of the scatter plot above are shown.

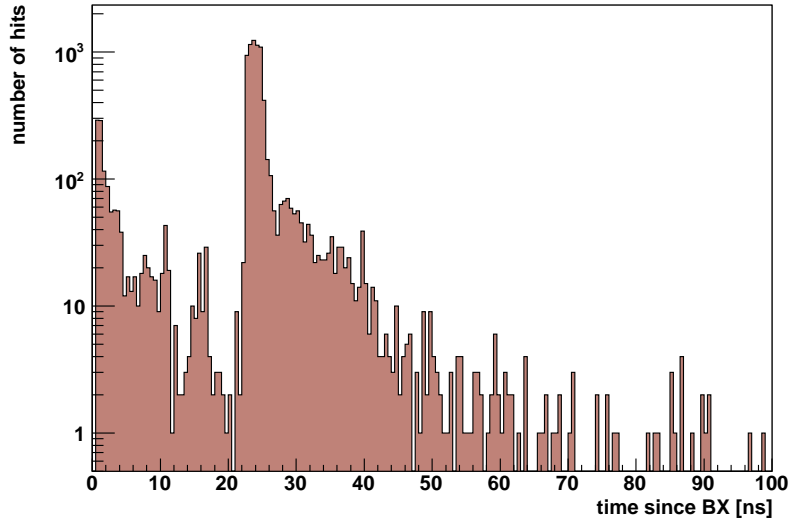


**Figure 4.11:** Distribution of hits in SIT Layer 1 as a function of time. The bunch crossing occurs at  $t = 0$ . Note the logarithmic scale. Parameters are the same as in Figure 4.10.

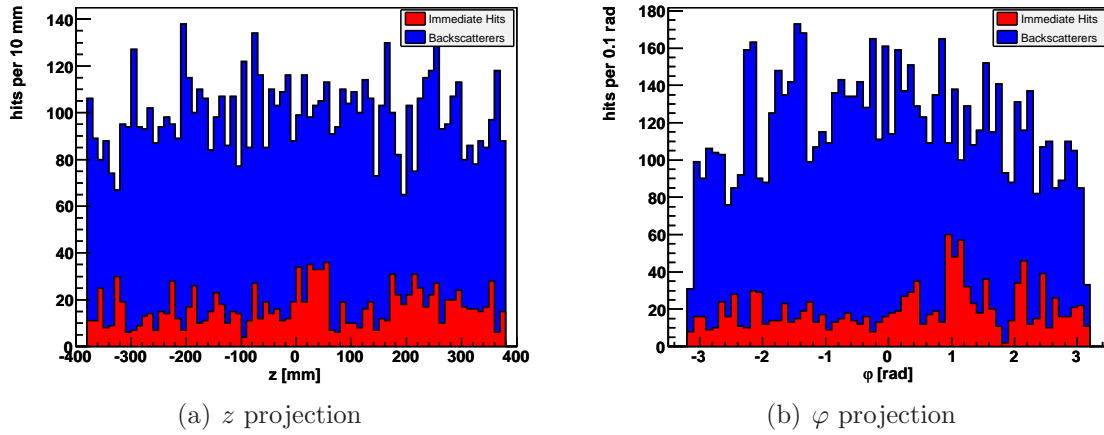


**Figure 4.12:** Time separation applied to the projections of the occupancy in Figure 4.10. Immediate hits are represented by red bars, secondary hits are blue.

### 4.2.2.3 Absorbed Dose in the SIT

The totally absorbed electromagnetic dose is obtained as described in Section 4.2.1.5. Only a few specifics have to be taken into account, for example the active silicon thickness. At the radius of the SIT the expected flux is reduced considerably compared to the VXD.

According to the increased thickness the spectrum of the energy deposits should be similar to the one for the VXD but shifted to higher values. Its shape, however, is a little surprising. This spectrum is shown in Figure 4.13 for Layer 1, again at logarithmic and linear scale. The mean value of this distribution amounts to  $\overline{E}_{\text{dep}} = 281.5 \text{ keV}$  which is nearly a factor three times the theoretical value of 103.7 keV.

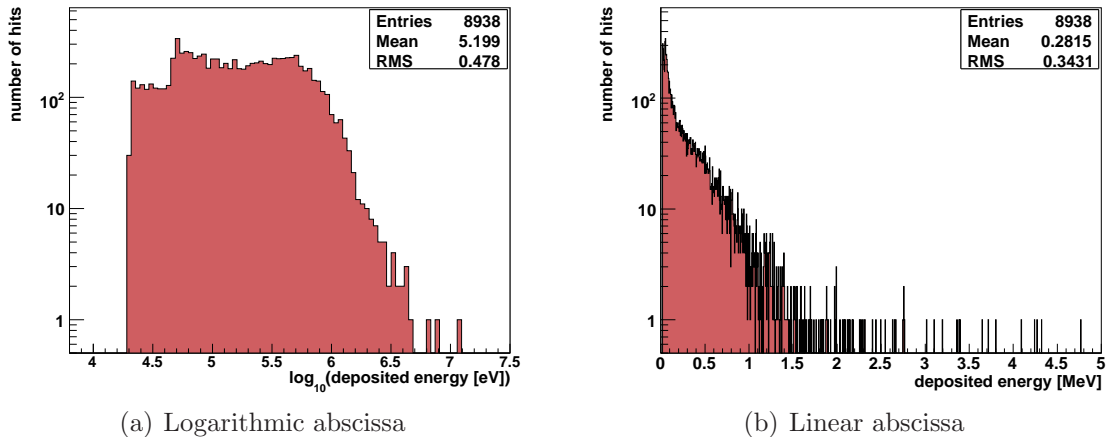


**Figure 4.13:** Spectrum of the energy deposits in SIT Layer 1. In subfigure (a) the abscissa gives orders of magnitude based on electron volt, in (b) the linear distribution is plotted. The issued mean value is  $\overline{E}_{\text{dep}} = 281.5 \text{ keV}$ . Parameters are the same as in Figure 4.10.

The shape of the spectrum as it appears in Figure 4.13(a) poses questions. The sharp edge at low energies matches the MOKKA cut at 20% of a MIP but there is no physical explanation for two maxima. The reason has been found in the simulation software:

- Other than for the VXD only the sensitive silicon layers of the SIT are described in MOKKA. There is no mechanical support or electronics implemented, yet. To account for the additional scattering in such material the radiation length of the layers was increased by means of an enhanced value for the silicon density. An entry `silicon_8.72gccm` is fetched from the materials database, which indeed is silicon with a mass density of  $\rho = 8.72 \text{ g cm}^{-3}$ . This call is hard-coded in the SIT driver, as shown in Figure 4.14, and leads to an appropriate radiation length for SIT traversings. On the other hand the assignment of these interactions to the active silicon sensor is not reasonable—the issued value of the deposited energy is too large.
- The simulations for the currently considered event sample were processed in October 2006 using MOKKA 6.01. Up to this version the based GEANT 4 version providing the description of the physics was 8.0. There were some known problems concerning

```

[...]
//*****
// Two cylindres in modified Si to keep good X0
//*****
[...]
G4LogicalVolume *SitLogical = new G4LogicalVolume(SitSolid,
                                                    CGAGeometryManager::GetMaterial("silicon_8.72gccm"),
                                                    "Sit", 0, 0, 0);
[...]

```

**Figure 4.14:** Extract of the SIT driver for MOKKA. The upper lines show a comment in the code. Beneath a logical volume for the internal processing of the particle transportation through the SIT layer is implemented. It is build from a geometrical shape (“solid”) and a material. Here silicon with a mass density of  $8.72 \text{ g cm}^{-3}$  is assigned. Further parameters can be set.

electromagnetic scattering in very thin layers. The misconduct depends on thresholds and limits; thus it could affect the SIT sensors while working properly for the VXD. The two maximum structure of the spectrum may be related to this topic. Major improvements for the electromagnetic processes were made in version GEANT 4.8.1. For simulations using the later version, the double peak structure disappears.

For the estimate of the totally absorbed dose, the spectrum of the energy deposits is scaled by the ratio of the real mass density over the enhanced one:

$$K = \frac{2.33 \text{ g cm}^{-3}}{8.72 \text{ g cm}^{-3}}.$$

The result is truncated again at 20% of a MIP deposit.

Using the scaled spectrum of deposits the dose can be calculated from (4.3) inserting the real silicon mass density  $\rho_{\text{Si}} = 2.33 \text{ g cm}^{-3}$ . The silicon thickness is  $dr = 300 \mu\text{m}$  and the cylinder length is subdivided into bins of  $dz = 20 \text{ mm}$ . Angular segmentation is applied as for the VXD. Due to the reduced flux at the SIT radii the colour scale in the resulting dose distribution, shown in Figure 4.15, issues Gy. The maximum of the absorbed dose is three orders of magnitude less than in the innermost VXD layer.

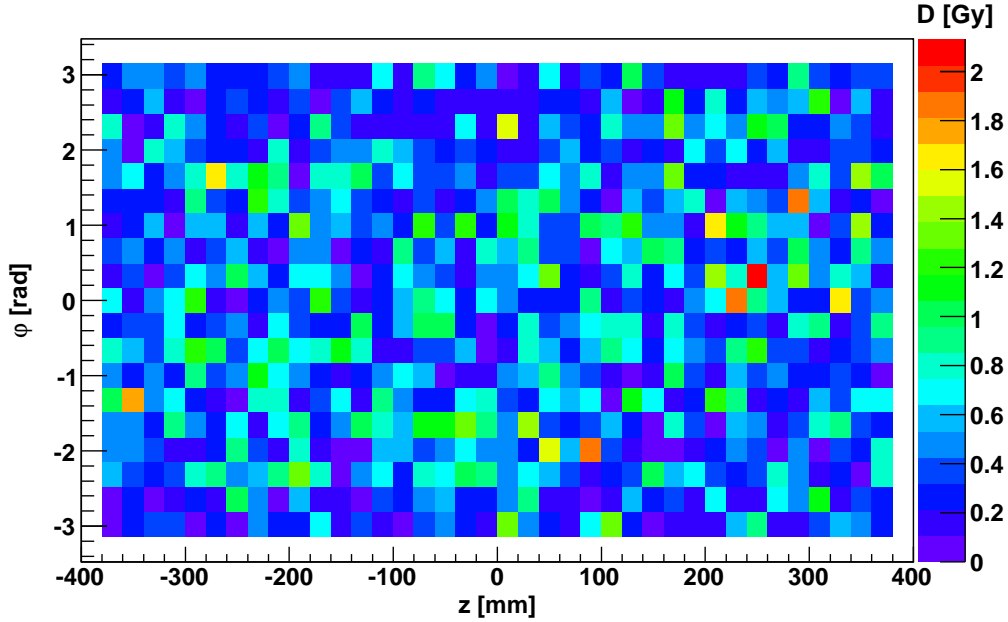


**Figure 4.15:** The electromagnetic dose absorbed in Layer 1 of the SIT for an integrated luminosity of  $500 \text{ fb}^{-1}$ . The spatial distribution is resolved by bins of  $dz = 20 \text{ mm}$  along the detector axis and  $d\varphi = 2\pi/19$  in the azimuth angle. The colour scale is given in Gy on the right side. Parameters are the same as in Figure 4.10.

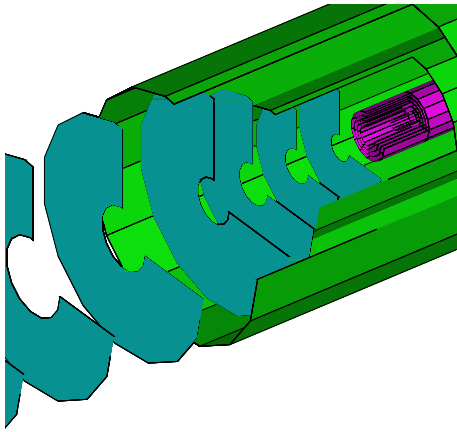
### 4.2.3 The Forward Tracking Discs

In order to cover the largest possible solid angle for the track measurement, seven silicon discs are installed around the beam pipe at different distances from the  $z = 0$  plane. They record particles within a polar angle range between  $\vartheta = 5.8^\circ$  and  $35.0^\circ$ . The thickness of the sensitive silicon is  $300 \mu\text{m}$  for all discs but there are two different read-out structures. While the Discs 1 to 3 close to the IP are pixel detectors, for the four more distant discs a strip design is sufficient. The positioning and the proportions relatively to the VXD and SIT can be seen in Figure 4.16 together with a list of relevant dimensions.

#### 4.2.3.1 Total Hit Occupancy from Background

The forward tracking discs are flat round discs parallel to the  $x$ - $y$  plane. The spatial distribution of background hits can be displayed in a natural way showing this plane. Exemplarily, the scatter plots for Disc 2 and Disc 5 are shown in Figure 4.17. The inhomogeneity of the occupancy is caused by the mentioned stream of low energetic particles scattered off the outgoing beam pipe and leading to increased hit density around  $\varphi = 0$  in the outer VXD layers. The shape and the size of this stream are captured by the tracking discs, especially those with small inner radius.

The projections of the occupancy to the polar coordinates,  $r$  and  $\varphi$ , are given in Figure 4.18 for Disc 5 in order to get an idea of the amount of hits. In particular the dependence



Disc	$z$ [mm]	$r_i$ [mm]	$r_o$ [mm]	$\vartheta_i$ [deg]
1	200	38	140	10.76
2	320	48	140	8.53
3	440	59	210	7.64
4	550	68	270	7.05
5	800	90	290	6.42
6	1050	111	290	6.03
7	1300	132	290	5.80

**Table 4.3:** Geometric dimensions of the FTD layers;  $z$  is the position along the detector axis,  $r_i$  and  $r_o$  the inner and outer radius, respectively, and  $\vartheta_i$  the minimal covered polar angle.

**Figure 4.16:** The arrangement of the inner silicon trackers. The vertex detector is represented in purple as in Figure 4.1. It is surrounded by the two SIT layers, shown in green (cf. Figure 4.9). For one detector side the forward tracking discs are shown in blue, where the seventh disc is merely indicated. Some important properties are given in Table 4.3.

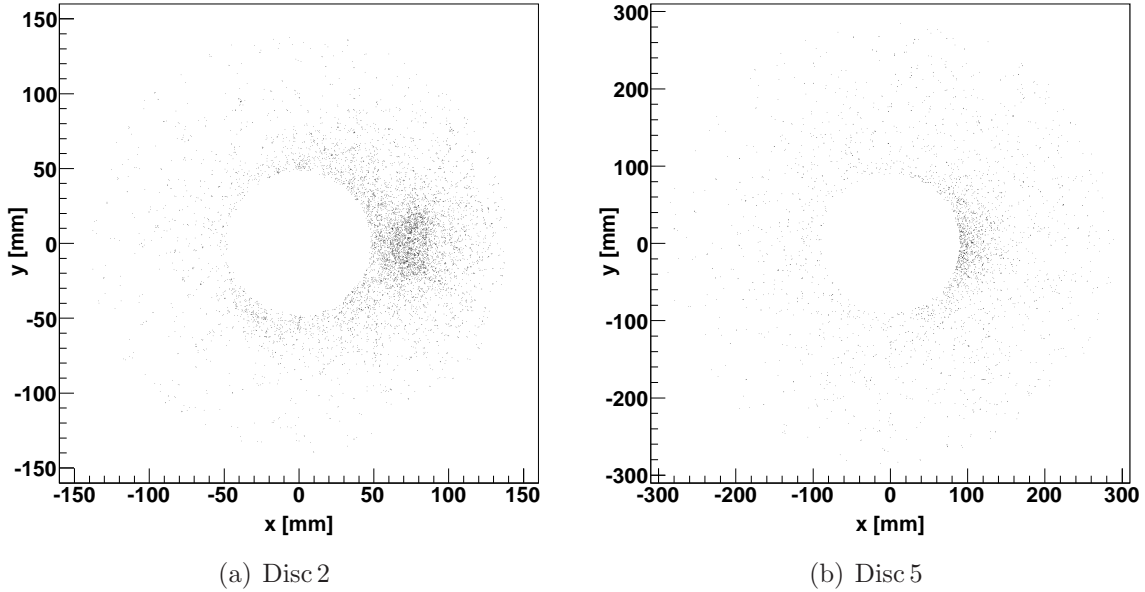


**Figure 4.17:** Scatter plots of the total hit occupancy for 100 BX in the forward tracking discs 2 and 5. Note the different extensions. The parameters of this event sample are 20 mrad crossing angle, a solenoidal magnetic field and the *Tesla* beam parameter set for  $\sqrt{s} = 500$  GeV.

on the distance from the beam,  $r$ , and the asymmetry in  $\varphi$  are visible. The occupancy is clearly lower than for the VXD.

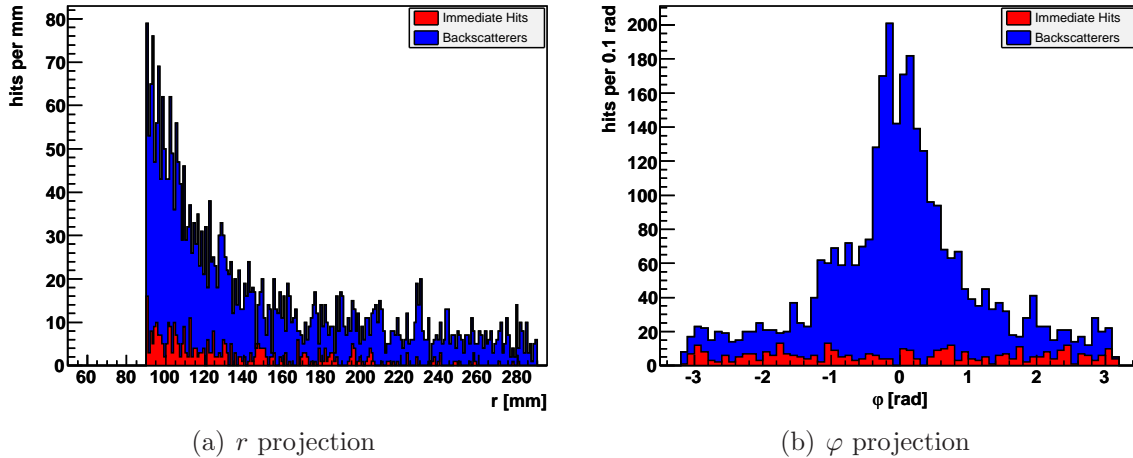


**Figure 4.18:** Time separated projections of the hit occupancy for Disc 5, shown in Figure 4.17(b), to (a)  $r$  and (b)  $\varphi$ . Immediate hits are represented by red bars, secondary hits are blue.

The currently discussed plots are already separated into immediate and secondary hits. The former contribute only a little fraction to the entire FTD occupancy, less than 20%. Most beamstrahlung pairs are produced with very small angles along the beam axis. That is they pass by at smaller radii than the disc coverage whereas backscattered particles in general are not aligned with the beam and may reach to larger radii. The dependence on the radius is similar for both. Immediate hits occur isotropically in the whole  $\varphi$  range.

#### 4.2.3.2 Time Separation

The time distribution of hits in the forward tracking discs is also considered. One important point is the placement of the discs along the  $z$  axis. Due to the different distances from the BeamCal the expected arrival time of backscattered particles varies for each disc. Since the spacings between the discs are similar and the flux of immediate hits drops down rapidly, the time of flight can be parameterised as follows:

$$t_i = t_7 + 0.6 \text{ ns} \cdot (7 - i).$$

The index  $i = 1 \dots 7$  numbers the discs and  $t_7 = 19.0 \text{ ns}$  is the minimal time of flight to reach the seventh disc assuming scattering at the BeamCal absorber. For Disc 5 the computed time of arrival is  $t_5 = 20.2 \text{ ns}$ , and is seen clearly as a peak in the time distribution in Figure 4.19.

As Disc 5 is 80 cm away from the IP no hits occur before 2.5 ns. In addition there is a third peak at 26 ns. This time is needed when particles from the IP fly in the opposite direction, hitting the BeamCal at  $z = -3.5 \text{ m}$ , and back to the Disc 5 at positive  $z$  position.

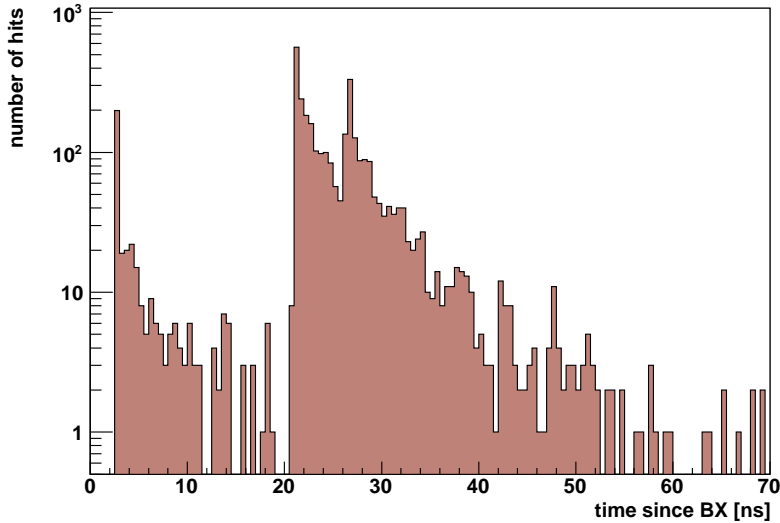


**Figure 4.19:** The distribution of FTD hits in Disc 5 as a function of time. The bunch crossing occurs at  $t = 0$ . The different peaks are explained in the text. Note the logarithmic scale at the ordinate. Parameters are the same as in Figure 4.17.

#### 4.2.3.3 Absorbed Dose in the FTD

The way how the FTD experience deposition from particles differs a little bit from the cylindrical trackers, because the main direction of motion of the particles is perpendicular to the disc surfaces. This holds for the majority of high energetic primaries as well as for particles curling around the magnetic field lines. The latter can traverse the cylindrical layers, which extend over a certain  $z$  region, many times, gradually depositing a lot of or even all their energy. The forward discs are crossed only once by most of the particles which explains the comparatively low occupancy.

Furthermore, these conditions influence the spectrum of the energy deposits. Contrary to expectations, two qualitatively different spectra were obtained dividing the discs into two groups. One contains the pixel detectors, Discs 1 to 3, the other includes the Discs 4 to 7. As representatives of the groups again the Discs 2 and 5 are chosen; their spectra of deposited energies are shown in Figure 4.20 in comparison. From Figures 4.20(b) and 4.20(d), respectively, a mean value of 350 keV for Disc 2 and 115 keV for Disc 5 is obtained. The calculated average energy deposit in 300  $\mu\text{m}$  silicon is 103 keV.

MOKKA's FTD driver describes the geometry of the discs consecutively in a loop assuming a uniform setup for all of them. It ignores additional hardware components for the pixel Discs 1 to 3. While strips can be read out at their endings, the pixels will be connected with the accompanying electronics each. This is done via bump bonding, employing In-Sn-soldering as material. To take care of the multiple scattering in these layers of material, the entry `silicon_8.72gccm` is called from the database as material for the first three discs. The radiation length in these detectors is described properly but the energy deposits in the sensitive material are strongly overestimated (cf. values in previous paragraph). Besides that the spectrum shows two clearly separated maxima.

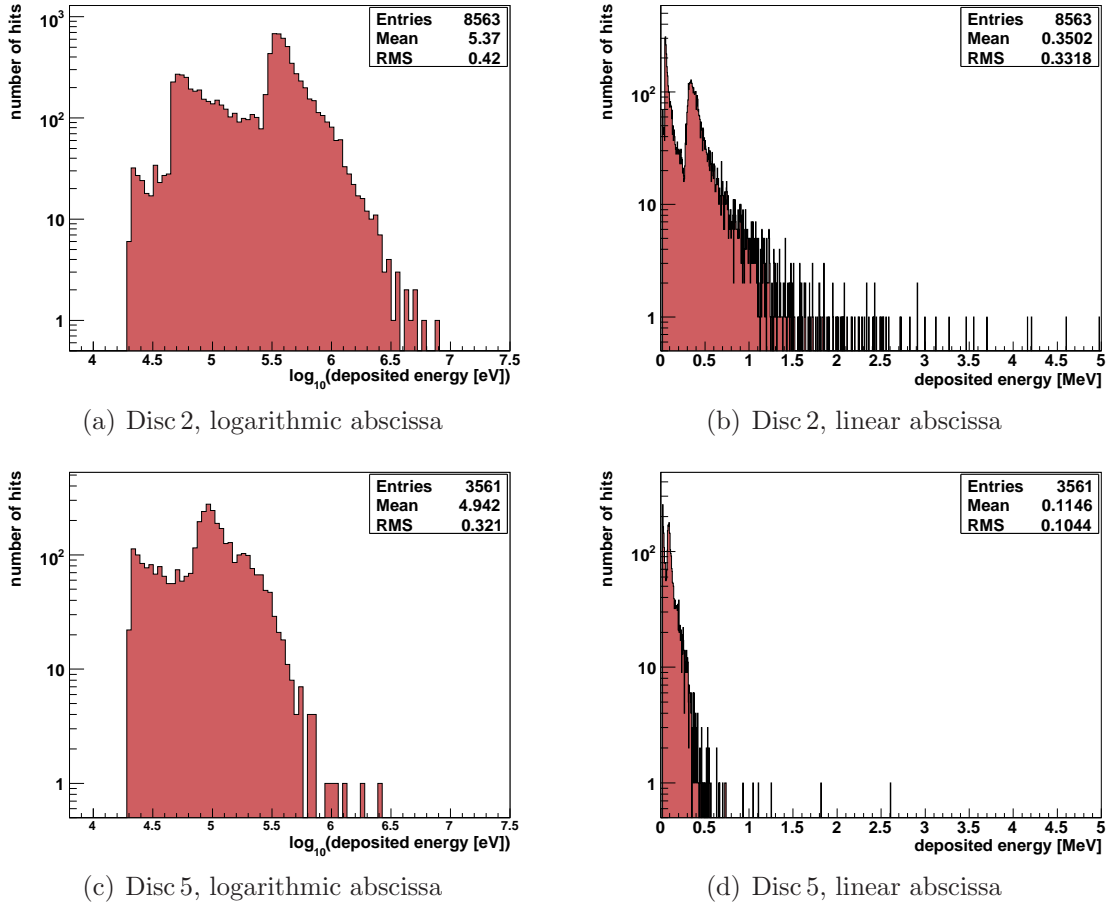


**Figure 4.20:** Spectra of the energy deposits in the FTD 2 and 5, both with logarithmic and linear abscissa as well. In Disc 2 at the top and Disc 5 beneath the shapes are different.

Apparently the shape of the spectrum in Figure 4.20(c) is equivalent to that in 4.20(a) though shifted to lower energies and truncated at 20% of the MIP deposit. Scaling down the spectrum of Disc 2 to the real silicon mass density by the correction factor  $K$  will probably not yield the accurate distribution neither the correct mean value. The fraction of stopped particles has to be taken into account. To proof their influence, the spectrum was plotted again regarding particles that are stopped within the logical volume of the respective disc. Substantially, the distribution of the deposits from such particles is isotropic over the full range. In this case a shift does not change the shape, and the spectrum of Disc 2 becomes similar to that for Disc 5.

As before, the totally absorbed dose is calculated using equation (4.3). The distinguishing feature of the FTD compared to the cylindrical trackers is the spatial orientation. It offers to display the disc surfaces in polar coordinates and requires a new expression for the element of extension,  $dV$ . The radial segmentation matches the inner and outer radii for each disc and consequently the bin size  $dr$  varies between 9 and 15 mm. Azimuthally, the annulus is subdivided into 60 segments yielding arc lengths of  $4 \text{ mm} \leq du \leq 30 \text{ mm}$ .

The sensor thickness is given by  $dz = 300 \mu\text{m}$ .

Using the scaled spectra with disc numbers up to 3, the dose distribution in Gy is given in Figure 4.21 for the Discs 2 and 5 and  $500 \text{fb}^{-1}$ . Hundreds of Gray are detected in the maximum of Disc 2; Disc 5 is less affected.

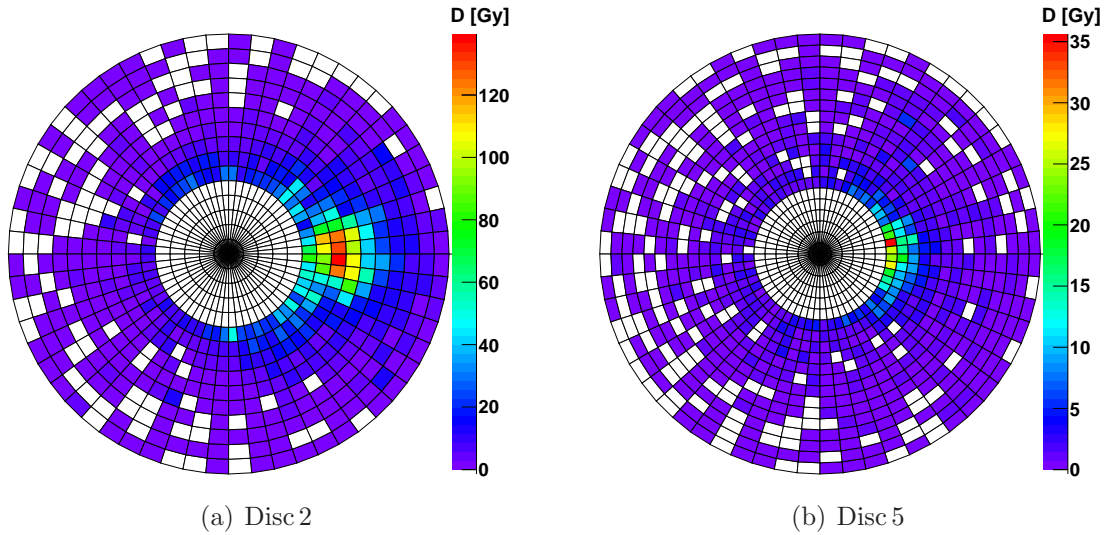


**Figure 4.21:** The electromagnetic dose absorbed in (a) Disc 2 and (b) Disc 5 of the FTD for an integrated luminosity of  $500 \text{fb}^{-1}$ . The colour scale is given in Gy on the right side. White segments are not hit by charged particles in this event sample. Parameters are the same as in Figure 4.17.



# Chapter 5

## Comparison of the Background for Different Options and Optimisation of the Design

Several event samples were simulated by Vogel [31] in order to compare options under discussion. In Table 5.1 the parameters used are summarised. The crossing angle and the magnetic field options are described in Section 2.4.2. Here they are combined uniquely, i. e. each crossing angle case is considered for only one specific magnetic field configuration. This is a result of the relation between them and of the chronology of the proposals for these design options. The beam sets refer to Table 2.1 on page 22. The column “Absorber” gives the thickness of the graphite layer in front of the BeamCal and the last column contains the underlying software versions.

Event sample	Crossing angle	Field	Beam set	Absorber	MOKKA/GEANT
X02tesla	2 mrad	solenoid	<i>Tesla</i>	50 mm	6.01 / 4.8.0
X20tesla	20 mrad	DID	<i>Tesla</i>	50 mm	6.01 / 4.8.0
X14tesla	14 mrad	anti-DID	<i>Tesla</i>	50 mm	6.02 / 4.8.1
X14nom	14 mrad	anti-DID	<i>Nominal</i>	50 mm	6.02 / 4.8.1
X14lowp	14 mrad	anti-DID	<i>Low P</i>	50 mm	6.02 / 4.8.1
X14nom020	14 mrad	anti-DID	<i>Nominal</i>	20 mm	6.03 / 4.8.1
X14nom050	14 mrad	anti-DID	<i>Nominal</i>	50 mm	6.03 / 4.8.1
X14nom100	14 mrad	anti-DID	<i>Nominal</i>	100 mm	6.03 / 4.8.1

**Table 5.1:** Summary of the parameters used for the simulation of the considered event samples.

Comparing different beam parameter options, one has take into account the relation between the integrated luminosity and the necessary number of bunch crossings, given in Equation (4.2). In order to compare occupancies and doses for the different options, the simulated event samples are normalised using the integrated luminosity,  $L$ . One hundred complete bunch crossings were processed for each parameter combination, except the one

with *LowP* beam parameters. Here the number of bunches in a train,  $n_b$ , is reduced by a factor of slightly more than two at the same repetition rate (cf. Section 2.4.2.3). Due to the smaller bunch sizes, the luminosity per bunch is almost the same and hence only half the bunch crossings were processed. Also one has to keep in mind that for the *Tesla* beam set, the luminosity per bunch crossing is by 30% higher than for the *Nominal* one. Hence a smaller number of bunch crossings is necessary to reach  $L = 500 \text{ fb}^{-1}$ . However, the *Tesla* parameters are obsolete for the ILC machine and merely used for comparison.

## 5.1 Beam Crossing Angle and Magnetic Field

### 5.1.1 Background in the VXD and the SIT

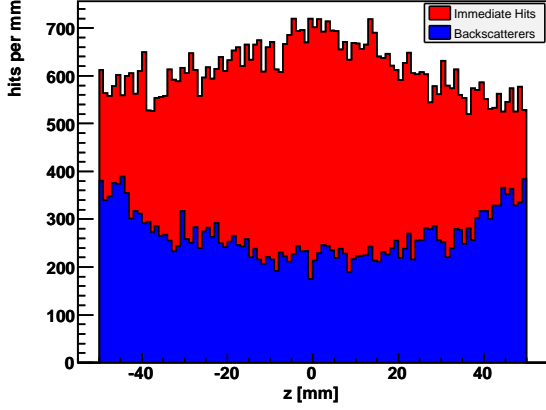
The largest flux of charged particles occurs in the innermost VXD layer. Therefore the time-separated occupancies of this layer in  $z$  and  $\varphi$  projection are compared in Figure 5.1 for the three crossing angle cases. As the beam parameters are equal, the amount of immediate hits is nearly the same. The small difference for the 14 mrad case can be attributed to the different MOKKA version.

The contribution from backscattered particles is smallest for 14 mrad crossing angle with anti-DID, as can be seen by comparing the left hand plots in Figure 5.1. All three options show a conspicuous profile in the  $\varphi$  projection of the occupancies from backscattered particles. The unisotropic distribution of secondary hits for  $\theta_x = 2 \text{ mrad}$  with solenoid field in Figure 5.1(b) is a result of the spatial distribution of beamstrahlung pairs at BeamCal position. which is reflected by the distribution of the energy deposited onto the BeamCal, shown in Figure 2.11 on Page 20. Charged particles backscattered at the BeamCal, again, follow helical trajectories back to the inner trackers. The cross section profile is turned once more by this angle in the same direction. The enhancement for  $\theta_x = 20 \text{ mrad}$  with DID in Figure 5.1(f) was already discussed in Section 4.2.1. Similarly the field map of the anti-DID option, used with the 14 mrad case in Figure 5.1(d), needs further refinements. As given, the field lines guide low energetic particles scattered off the outgoing beam pipe to the opposite side of the inner VXD layers around  $\varphi = \pi$ .

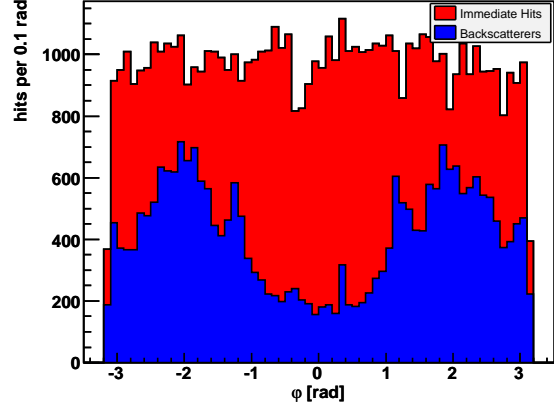
This comparison is repeated in Figure 5.2 for Layer 2. As expected, the density of immediate hits is lower. The distributions in  $z$  are almost flat. In the  $\varphi$  projection for 14 mrad with anti-DID field in Figure 5.2(d) the same structure as for Layer 1 is visible in the distribution of secondary hits. In contrast, the enhancements for the other options in the left hand plots of Figure 5.1 have disappeared.

The expected doses absorbed in the first VXD layer are compared in Figure 5.3 for an integrated luminosity of  $500 \text{ fb}^{-1}$ . They are similar due to the dominating fraction of immediate hits. The worst case is  $\theta_x = 20 \text{ mrad}$  with DID field, reaching a maximal dose of about 2 kGy. The reason is the enhanced density of secondary hits around  $\varphi = 0$ , as can be seen in Figure 5.3(c). The colour scale of this plot is adopted in the Figures 5.3(a) and 5.3(b).

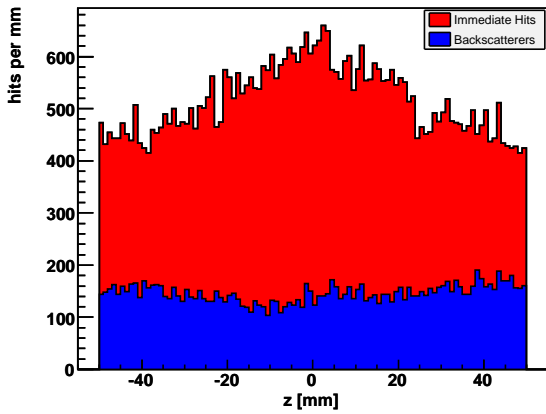
At the larger radii of the SIT, a large fraction of the background stems from backscat-



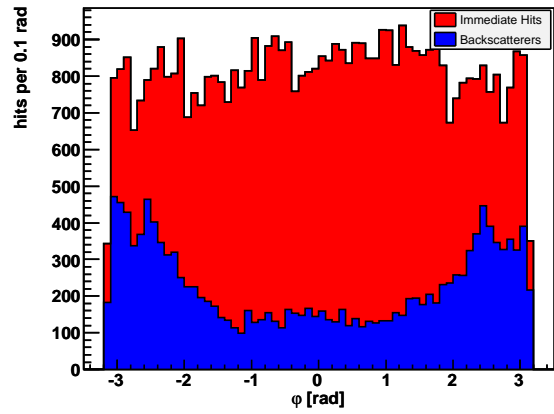
(a) Layer 1,  $z$  projection, 2 mrad, solenoid



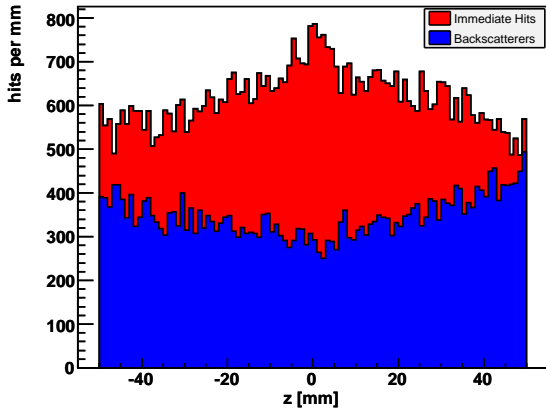
(b) Layer 1,  $\varphi$  projection, 2 mrad, solenoid



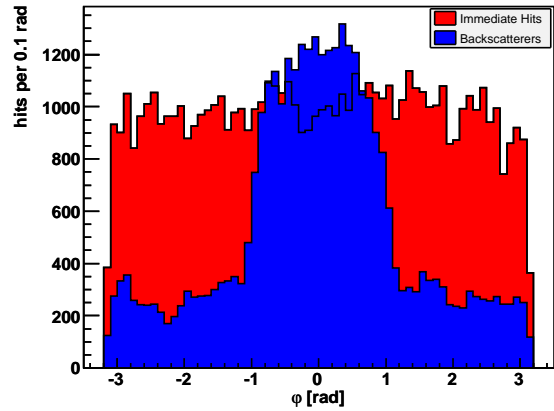
(c) Layer 1,  $z$  projection, 14 mrad, anti-DID



(d) Layer 1,  $\varphi$  projection, 14 mrad, anti-DID

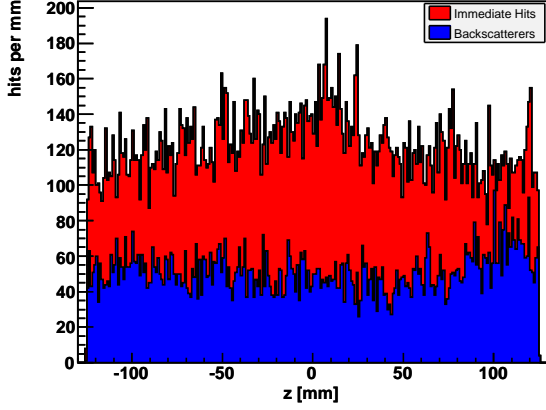


(e) Layer 1,  $z$  projection, 20 mrad, DID

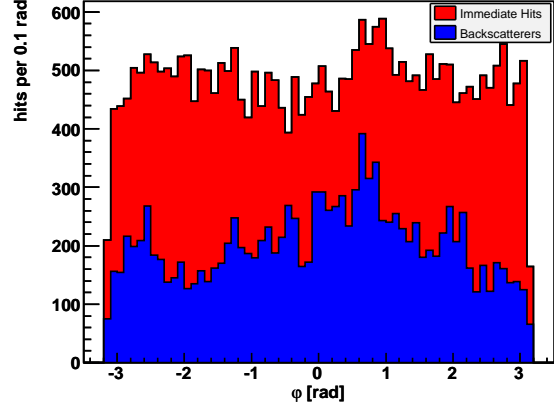


(f) Layer 1,  $\varphi$  projection, 20 mrad, DID

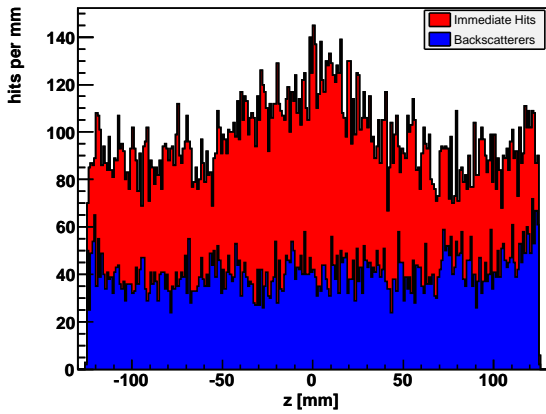
**Figure 5.1:** Comparison between the occupancies in VXD Layer 1 for the event samples 2 mrad with solenoid field (top), 14 mrad with anti-DID field (centre) and 20 mrad with DID field (bottom). For each case 100 BX were simulated using *Tesla* beam parameters. Shown are the projections to the  $z$  (left) and  $\varphi$  (right) coordinate. Time separation is applied.



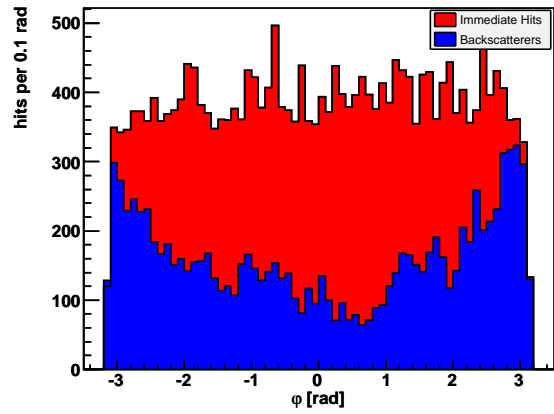
(a) Layer 2,  $z$  projection, 2 mrad, solenoid



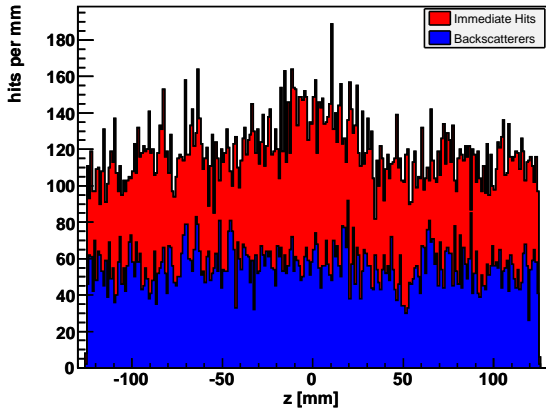
(b) Layer 2,  $\varphi$  projection, 2 mrad, solenoid



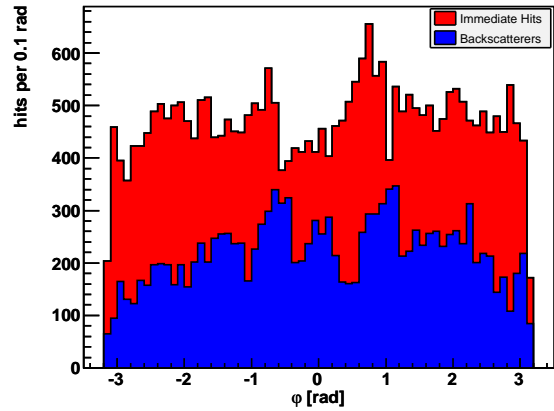
(c) Layer 2,  $z$  projection, 14 mrad, anti-DID



(d) Layer 2,  $\varphi$  projection, 14 mrad, anti-DID



(e) Layer 2,  $z$  projection, 20 mrad, DID



(f) Layer 2,  $\varphi$  projection, 20 mrad, DID

**Figure 5.2:** Comparison between the occupancies in VXD Layer 2 for the event samples 2 mrad with solenoid field (top), 14 mrad with anti-DID field (centre) and 20 mrad with DID field (bottom). For each case 100 BX were simulated using *Tesla* beam parameters. Shown are the projections to the  $z$  (left) and  $\varphi$  (right) coordinate. Time separation is applied.

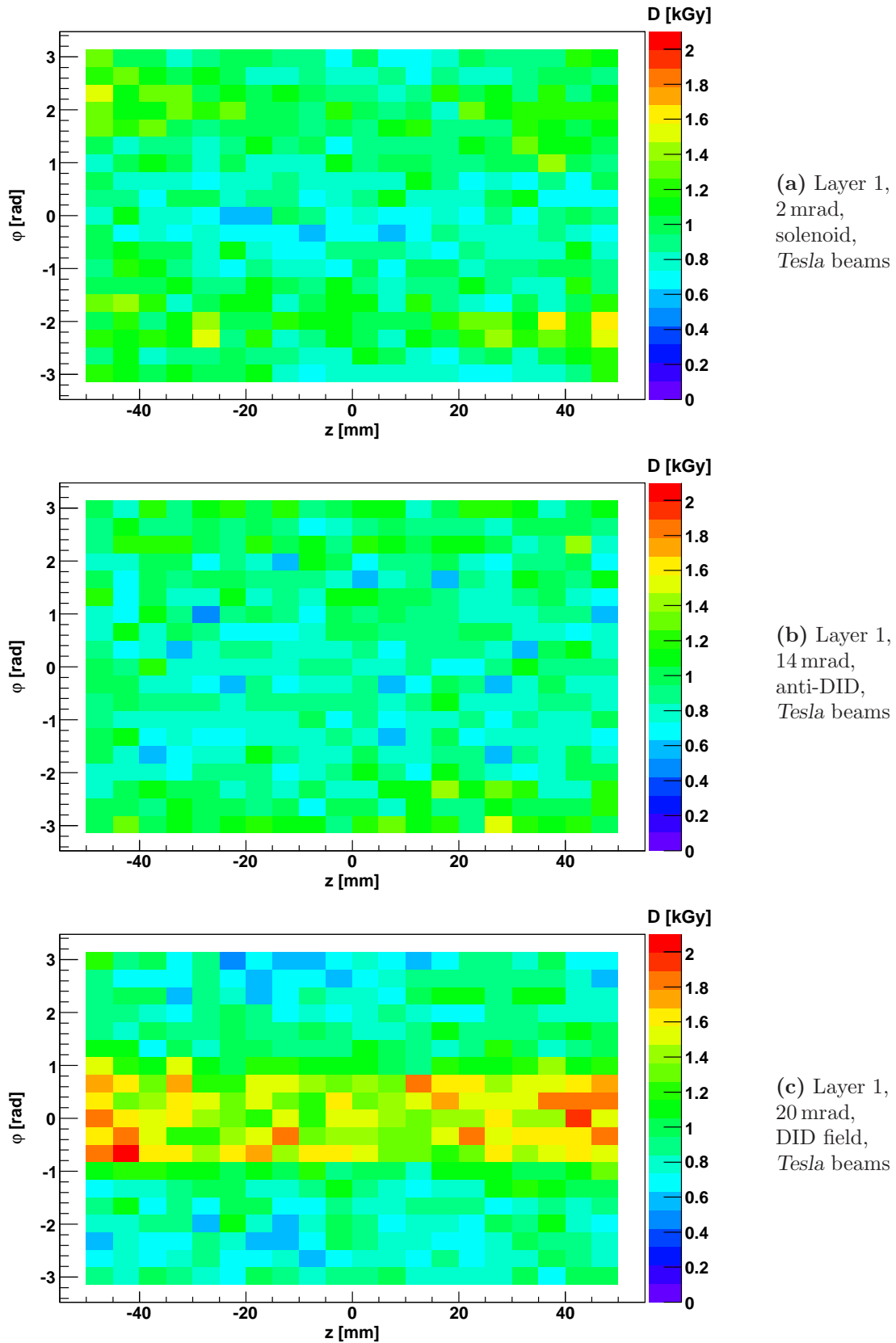


Figure 5.3: Comparison of the doses in VXD Layer 1 for  $L = 500 \text{ fb}^{-1}$  and *Tesla* beams.

tered particles, as shown in Figure 4.12. Nevertheless the differences between the dose distributions for the three crossing angle cases are scarcely worth mentioning. The maximum of slightly above 2 Gy—note the order of magnitude—appeared in SIT Layer 1 likewise for  $\theta_x = 20$  mrad with DID field.

### 5.1.2 Background in the FTD

In Figure 4.18 on page 50, the major fraction of background hits in Disc 5 is caused by backscattered particles. This is, however, a peculiar result for the DID field case at  $\theta_x = 20$  mrad. As shown in Figure 5.4 for Disc 2, the situation looks different for the other configurations. Similarly to the VXD, the distributions of the immediate hits are nearly the same and also the occupancies from secondary hits at 2 and 14 mrad are comparable. The latter show considerable enhancements for 20 mrad in Figures 5.4(e) and 5.4(f) originating from the stream of low energetic particles scattered off the outgoing beam pipe, as described in Section 4.2.1.4.

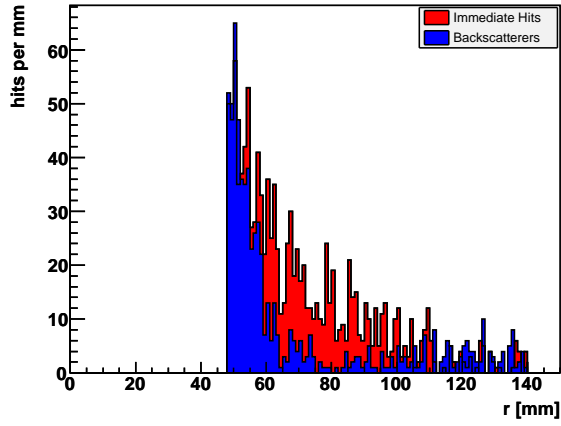
The absorbed doses for an integrated luminosity of  $500 \text{ fb}^{-1}$  are given in Figure 5.5 for pixel Disc 2 and strip Disc 5. Note the different colour scales of each plot. The maximum of the expected dose in the forward tracking discs is about 200 Gy, which occurred as an outstanding peak in the dose distribution of Disc 4 at 20 mrad and DID field. For the other options the values are clearly lower.

## 5.2 Beam Parameter Sets

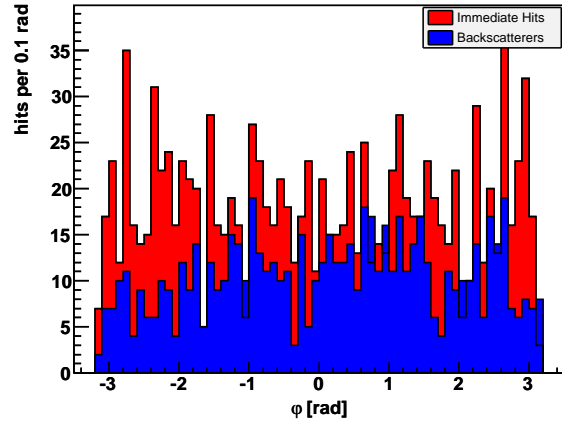
### 5.2.1 Background in the VXD and the SIT

As before, the time separated occupancies in Layer 1 are compared. Both  $z$  and  $\varphi$  projection are shown in Figure 5.6 for the three considered beam parameter sets. Here the shapes of the distributions are in agreement, and the influence of the beam parameters on the immediate hits is visible. Their number is reduced to roughly 60 % for the *Nominal* case in comparison with the *Tesla* parameters. The latter provide a larger luminosity  $\mathcal{L}$ , resulting in intenser incoherent pair creation (cf. Table 2.1). The amount of hits for the *LowP* case in Figures 5.6(e) and 5.6(f) is similar to the *Nominal* one in (c) and (d), though a little increased. This corresponds to comparable event rates with only half the bunch crossings for *LowP* beams. However, for the reconstruction of a certain event the occupancy per bunch crossing might be essential. For *LowP* beams there will be more than twice as much spurious hits per BX in the tracker. From that point of view this option seems not very favourable.

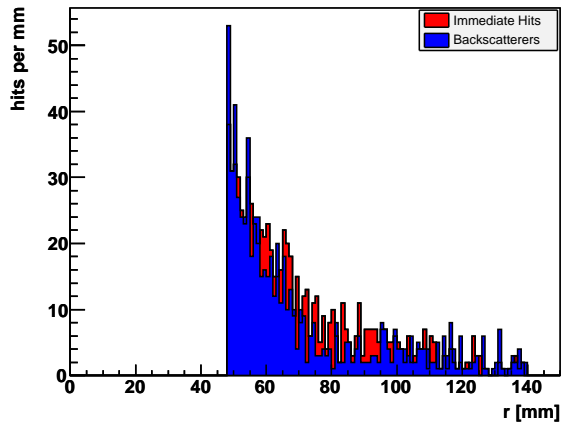
The absorbed doses are extrapolated to an integrated luminosity  $L$ , which accommodates a stipulated statistics. Hence, the differences between the dose distributions for the three beam parameter sets are not very pronounced. They are shown in Figure 5.7 for VXD Layer 1, again with the same colour scale applied to all. The maximal dose is obtained for the *LowP* case. It is reduced by 15 % for *Nominal* parameters.



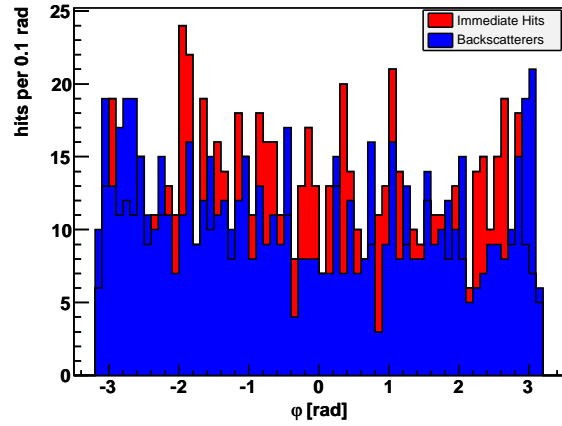
(a) Disc 2,  $r$  projection, 2 mrad, solenoid



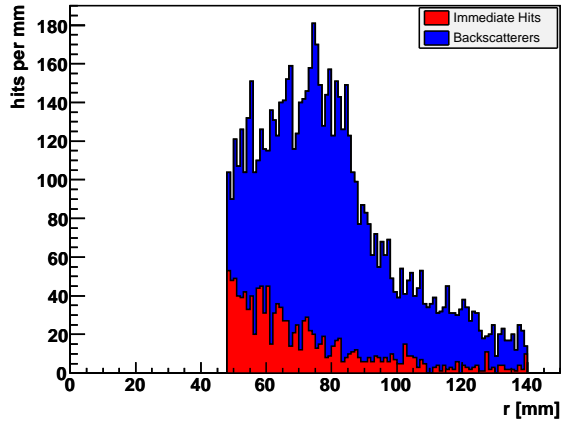
(b) Disc 2,  $\varphi$  projection, 2 mrad, solenoid



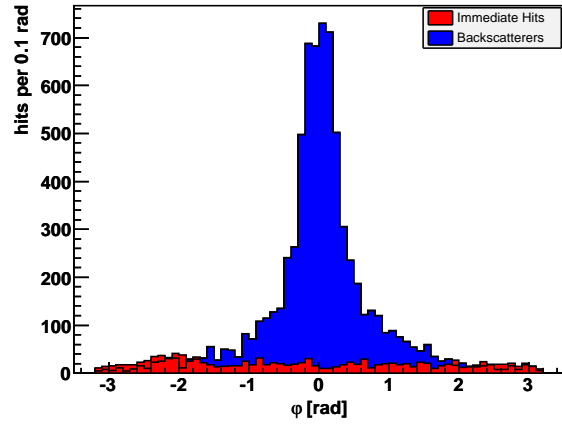
(c) Disc 2,  $r$  projection, 14 mrad, anti-DID



(d) Disc 2,  $\varphi$  projection, 14 mrad, anti-DID



(e) Disc 2,  $r$  projection, 20 mrad, DID



(f) Disc 2,  $\varphi$  projection, 20 mrad, DID

**Figure 5.4:** Comparison between the occupancies in FTD 2 for the event samples 2 mrad with solenoid field (top), 14 mrad with anti-DID field (centre) and 20 mrad with DID field (bottom). For each 100 BX were simulated using *Tesla* beam parameters. Shown are the projections to the  $r$  (left) and  $\varphi$  (right) coordinate. Time separation is applied.

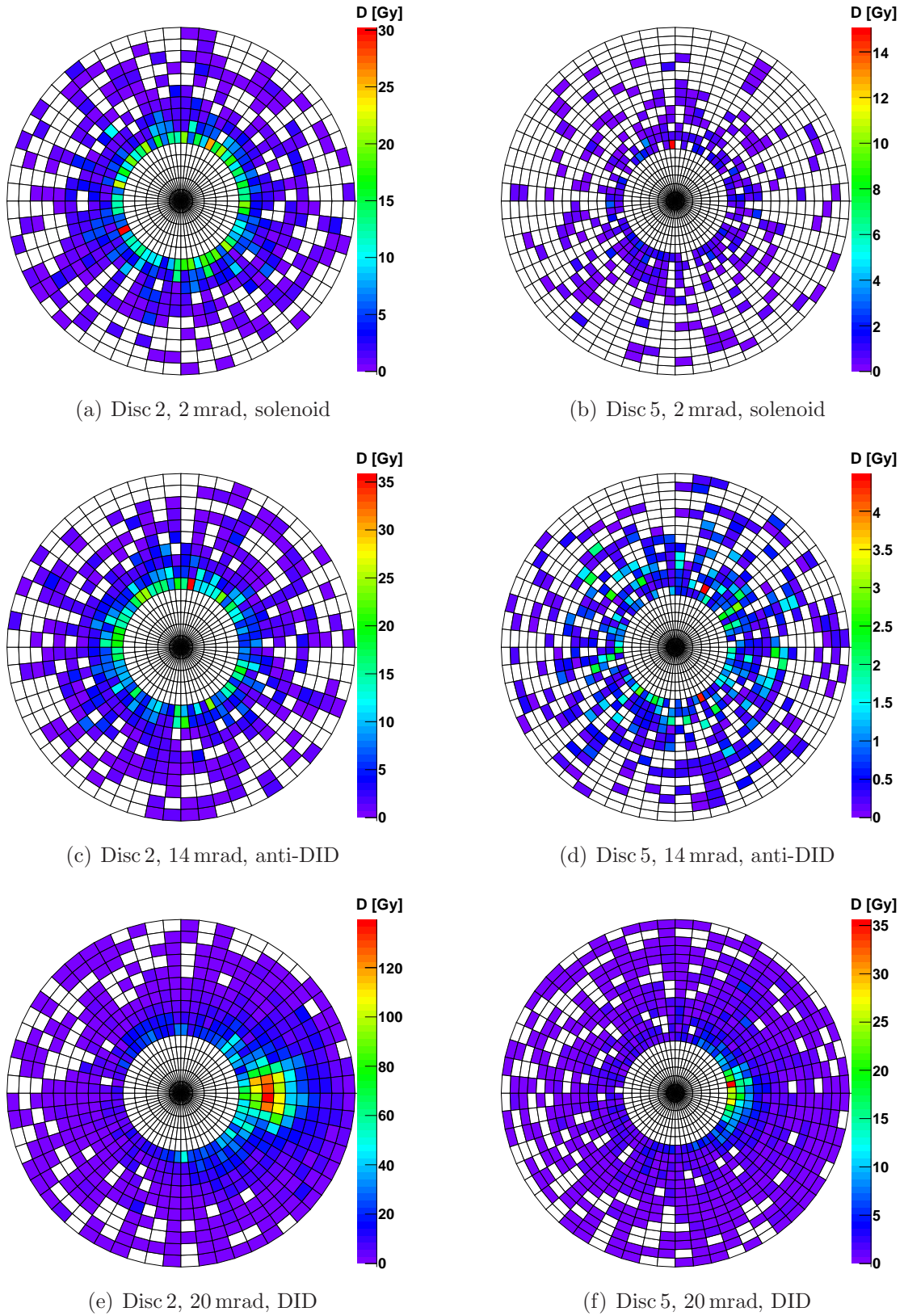
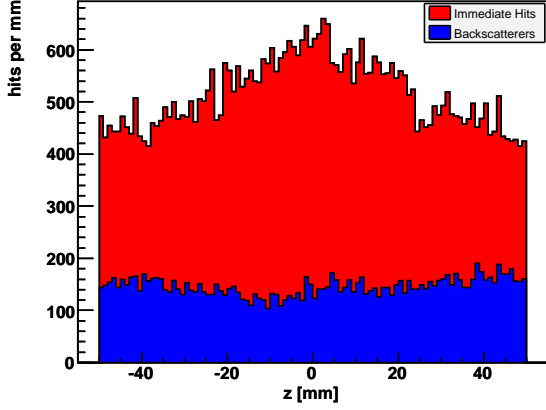
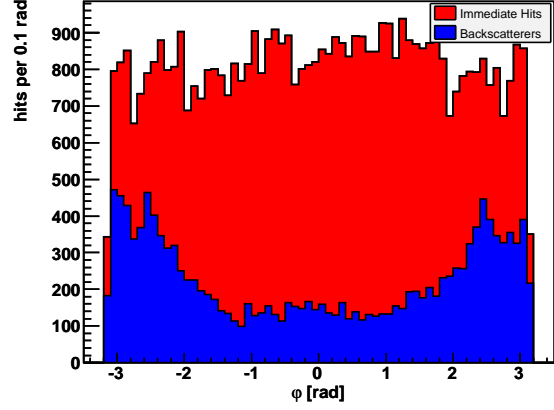


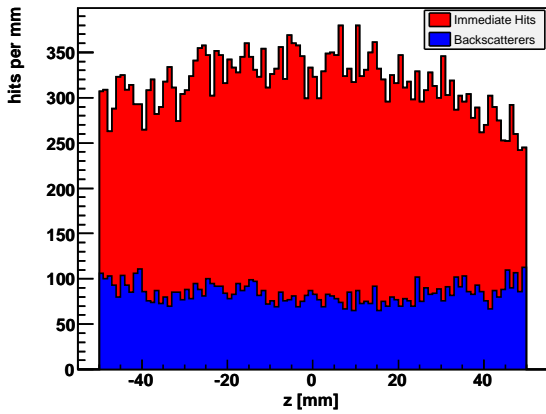
**Figure 5.5:** Comparison of the doses in Disc2 (left) and 5 (right) for an integrated luminosity of  $500 \text{ fb}^{-1}$ . The three crossing angle cases are simulated uniformly using *Tesla* beams.



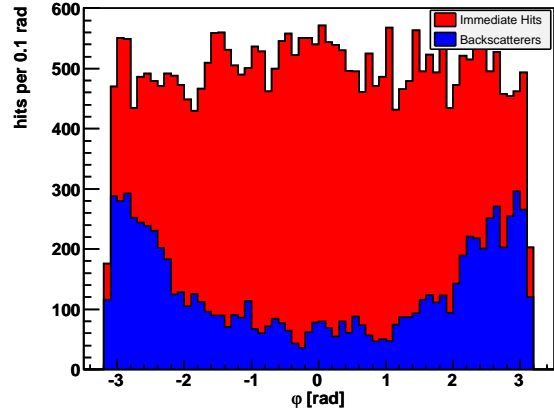
(a) Layer 1,  $z$  proj., *Tesla* beams, 100 BX



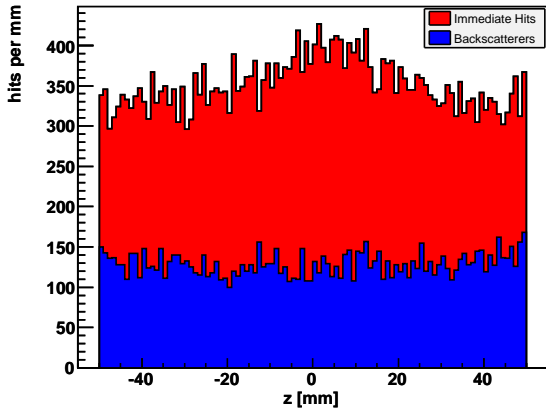
(b) Layer 1,  $\varphi$  proj., *Tesla* beams, 100 BX



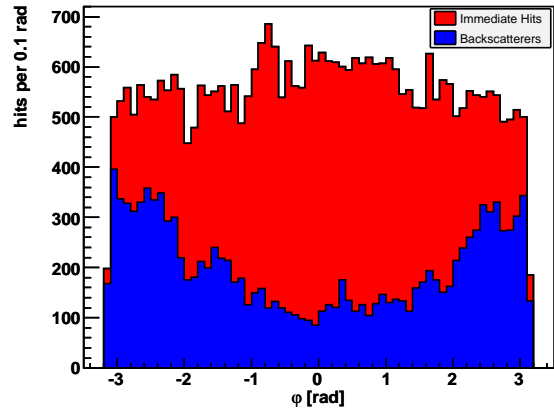
(c) Layer 1,  $z$  proj., *Nominal* beams, 100 BX



(d) Layer 1,  $\varphi$  proj., *Nominal* beams, 100 BX



(e) Layer 1,  $z$  proj., *LowP* beams, 50 BX



(f) Layer 1,  $\varphi$  proj., *LowP* beams, 50 BX

**Figure 5.6:** Comparison between the occupancies in VXD Layer1 for the three beam parameter sets *Tesla* (top), *Nominal* (centre) and *LowP* (bottom). For each event sample the crossing angle is  $\theta_{\times} = 14$  mrad with anti-DID magnetic field option. Shown are the projections to the  $z$  (left) and  $\varphi$  (right) coordinate. Time separation is applied.

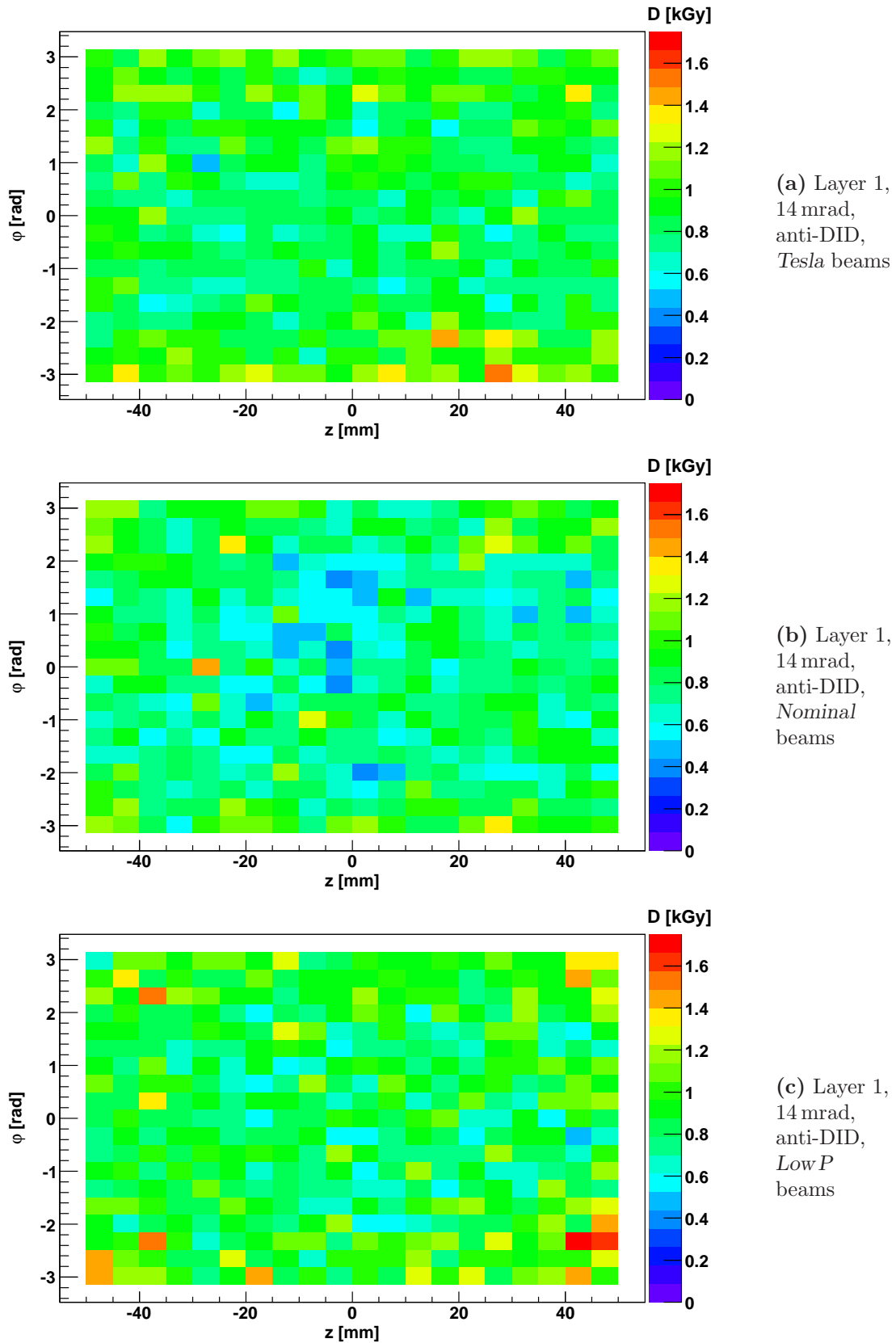


Figure 5.7: Comparison of doses in VXD Layer 1 for  $500 \text{ fb}^{-1}$  and 14 mrad with anti-DID.

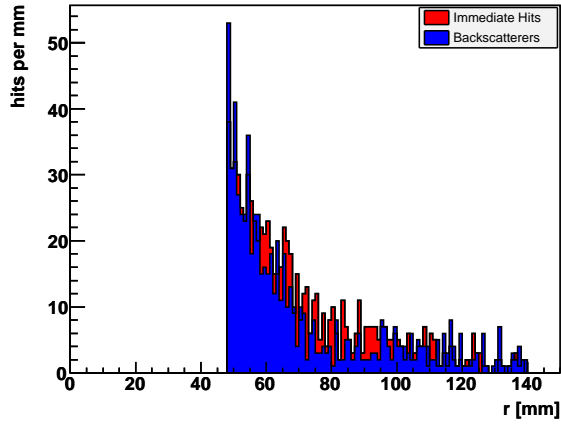
The occupancies in the SIT are very similar for the different beams. The qualitative relations agree with the VXD results but the statistics is low. For *Nominal* beams the hit density is a little bit smaller, for the *LowP* case it is accumulated by half the bunch crossings. The dose distributions in Layer 1 are almost indistinguishable.

### 5.2.2 Background in the FTD

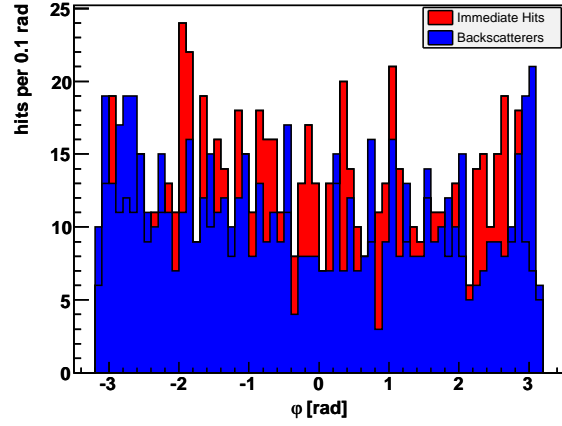
It applies also to the FTD that the relation between immediate and secondary hits does not depend on the beam parameters. According to Figure 5.8 the total occupancy is largest for *Tesla* beams. Again the number of hits for *LowP* beams is twice as much as for the *Nominal* case. The expected doses confirm these results in principle. There are fluctuations due to the small statistics. The maximum is below 100 Gy.

## 5.3 Design of the Mask and the Graphite Absorber

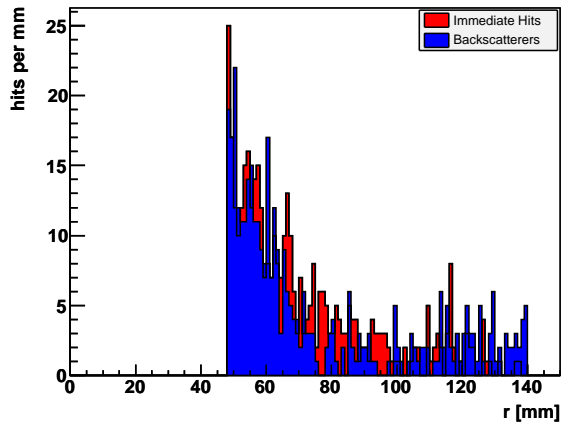
The importance of the graphite absorber in front of the BeamCal becomes clear in Figure 5.9. For the baseline design with  $\theta_x = 14$  mrad, anti-DID field and *Nominal* beam parameters, the thickness of the graphite layer was varied. Additionally, the beam pipe in the very forward region was simulated as beryllium instead of steel, like it is planned for the interaction region. Hence another event sample for a 50 mm absorber was produced besides the simulations with 20 and 100 mm graphite, respectively. While the distributions of immediate hits are the same, the amount of secondaries changes strongly. If there is the possibility to hold 100 mm of graphite in front of the BeamCal instead of 50, the background in the silicon trackers due to backscattered particles could be suppressed significantly.



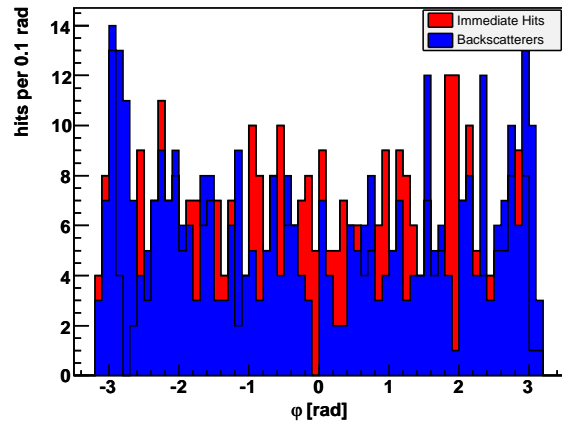
(a) Disc 2,  $r$  proj., *Tesla* beams, 100 BX



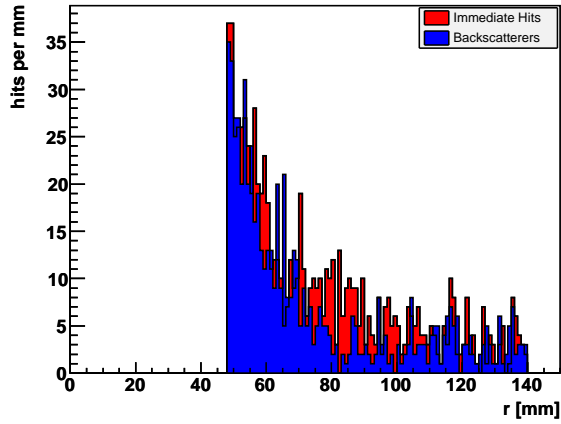
(b) Disc 2,  $\varphi$  proj., *Tesla* beams, 100 BX



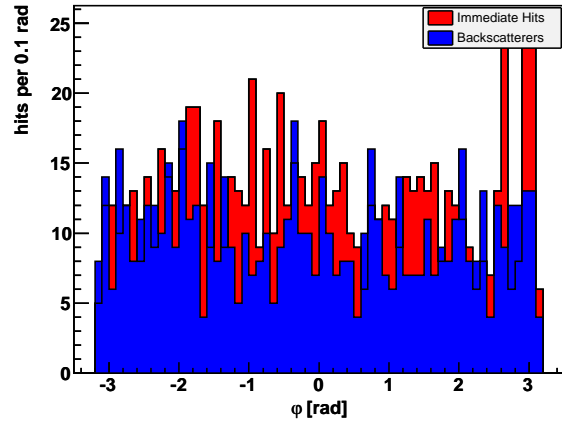
(c) Disc 2,  $r$  proj., *Nominal* beams, 100 BX



(d) Disc 2,  $\varphi$  proj., *Nominal* beams, 100 BX

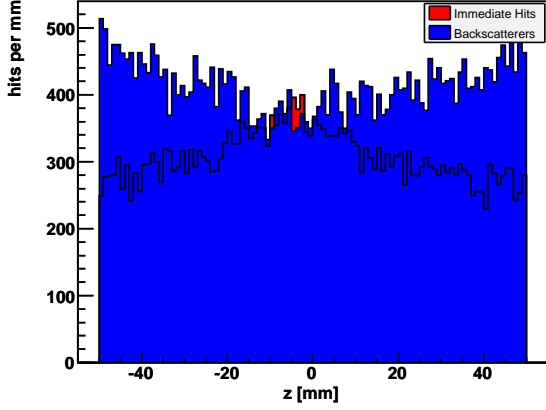


(e) Disc 2,  $r$  proj., *Low P* beams, 50 BX

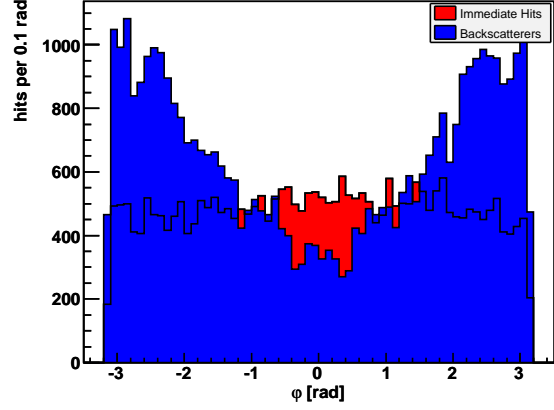


(f) Disc 2,  $\varphi$  proj., *Low P* beams, 50 BX

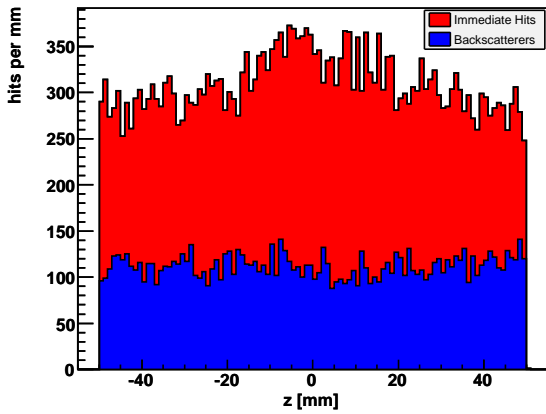
**Figure 5.8:** Comparison between the occupancies in FTD 2 for the three beam parameter sets *Tesla* (top), *Nominal* (centre) and *Low P* (bottom). For each event sample the crossing angle is  $\theta_{\times} = 14$  mrad with anti-DID magnetic field option. Shown are the projections to the  $r$  (left) and  $\varphi$  (right) coordinate. Time separation is applied.



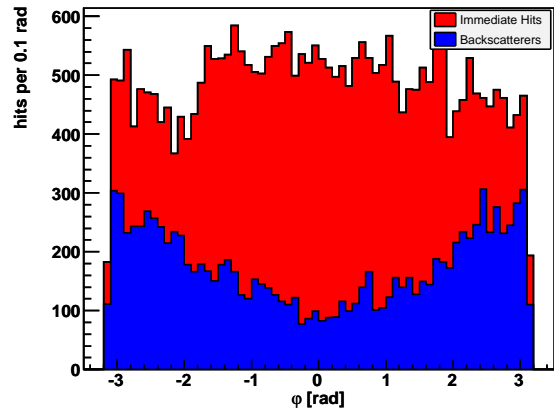
(a) Layer 1,  $z$  projection, absorber: 20 mm



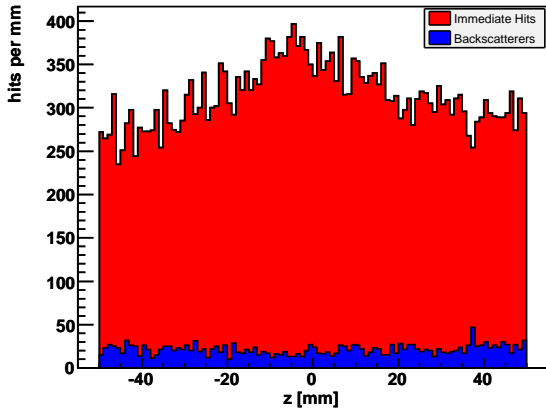
(b) Layer 1,  $\varphi$  projection, absorber: 20 mm



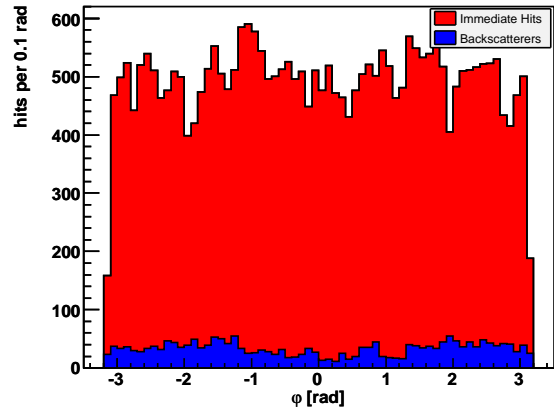
(c) Layer 1,  $z$  projection, absorber: 50 mm



(d) Layer 1,  $\varphi$  projection, absorber: 50 mm



(e) Layer 1,  $z$  projection, absorber: 100 mm



(f) Layer 1,  $\varphi$  projection, absorber: 100 mm

**Figure 5.9:** Comparison between the occupancies in VXD Layer 1 for graphite absorbers of 20 (top), 50 (centre) and 100 mm (bottom) thickness. For each event sample the crossing angle is  $\theta_{\times} = 14\text{mrad}$  with anti-DID option, *Nominal* parameters are used. Shown are the projections to the  $z$  (left) and  $\varphi$  (right) coordinate. Time separation is applied.



# Chapter 6

## Conclusions

A testbeam setup to measure the performance of sensors as a function of the absorbed electromagnetic dose was optimised by Monte Carlo simulations. The geometry of this setup was dimensioned to exploit an electron beam efficiently and to accomplish irradiation over the complete sensor area as uniform as possible. The testbeam setup in Figure 3.7 eventually was built on the basis of the simulation results.

The setup was used at the 10 MeV electron accelerator DALINAC to irradiate diamond and silicon sensors. The number of the electrons passing through the sensor, which is needed for the calculation of the totally absorbed dose, was measured over the time as a current at the Faraday cup downstream the sensor. The backscattering rate at this copper-made Faraday cup was estimated from the simulation. It was found to be about 2% of the electrons that reach the cup. Thus the current measured is too low and needs to be corrected in order to determine the electron flux through the sensor.

To calculate the dose, the deposition of energy during the passage of the electrons through the sensor material was simulated. The obtained average energy deposit, together with the corrected Faraday cup current, yields the absorbed dose in the sensor over the according period of irradiation. At the testbeam, diamond sensors were tested up to 7 MGy absorbed dose, which approaches the expected dose in the beam calorimeter of the International Linear Collider during one year of running. A so-called pumping was observed for all samples, that is an increase of the charge collection distance for doses of up to 1 MGy. Above that value the charge collection distance as a function of the absorbed dose decreases. However, all samples remained operational after irradiation.

In the second part of this thesis, the beamstrahlung-induced background in the silicon tracking devices of the large detector concept for the International Linear Collider is considered. The hit occupancy and the expected dose due to beamstrahlung remnants is estimated. Several parameters of the International Linear Collider and the detector magnetic field are discussed. The collision of electron and positron bunches was simulated with the GUINEA-PIG program for several beam parameter sets: *Tesla*, *Nominal* and *LowPower*. The generated beamstrahlung pairs were processed for different crossing angles and magnetic fields using the full detector simulation MOKKA of the large detector concept. The simulated data were analysed, and the background was estimated in the silicon trackers,

namely the vertex detector, the silicon intermediate tracker and the forward tracking discs.

The results for the different parameters of the International Linear Collider and the magnetic field are compared in order to find the minimum hit occupancy in the trackers. In this manner, the *Low Power* beam parameter set has proved to be unfavourable. Though it exposes the detectors with a comparable long-term dose rate, the number of background hits per single bunch crossing roughly doubles in comparison with the *Nominal* parameters. This may make event reconstruction more difficult.

The background in the silicon trackers caused by particles that arrive immediately after the bunch crossing only depends on the beam parameters.

For a chosen beam parameter set, the influence of the detector geometry and the magnetic field configuration on the background can be estimated. While the most beamstrahlung pairs disappear into the outgoing beam pipe, a small fraction hits the beam calorimeter, producing showers in the tungsten absorber. Large amounts of backscattered particles, again, reach the interaction region with a delay of the time of flight from the interaction point to the beam calorimeter and back. The amount as well as spatial and energy distributions of the arising secondary hits in the central trackers are strongly influenced by the design of the very forward region and the magnetic field of the detector. The forward region design, in turn, depends among others on the beam crossing angle. It turned out that the solenoid field modified with the detector-integrated dipole leads to the highest density of secondary hits with very unisotropic spatial distributions. The occupancy for the anti-DID and 14 mrad crossing angle corresponds to that for 2 mrad and solenoidal magnetic field. In the anti-DID option, the dipole magnet aligns the magnetic field lines with the outgoing beams and thus guides low energetic particles, as in the 2 mrad case, to the outgoing beam pipe.

The absorbed electromagnetic doses for an integrated luminosity of  $500 \text{ fb}^{-1}$ , corresponding to one year of running, is estimated for the vertex detector, the silicon intermediate tracker and the forward tracking discs. While the innermost layer of the vertex detector very close to the interaction point has to resist up to several kGy, the dose in the silicon intermediate tracker is at the order of Gy. Again, the 14 mrad with anti-DID option is the most favourable case as the dose is lower than for the other options. For that case, the forward tracking discs are loaded with doses of a few Gy in disc 7 and up to 100 Gy in disc 1, near the interaction point.

The results of this work support the choice of  $\theta_{\times} = 14 \text{ mrad}$  for the beam crossing angle and the anti-DID field option as a baseline design for the large detector concept.

# Bibliography

- [1] TESLA Working Group. *TESLA Technical Design Report*. DESY 2001-011, ECFA 2001-209, March 2001.
- [2] The NLC Design Group. *Zeroth-Order Design Report for the Next Linear Collider*. LBNL-5424, SLAC-474, May 1996.
- [3] JLC Design Study Group. *JLC Design Study*. KEK Report 97-1, 1997.
- [4] F. Richard, J. R. Schneider, D. Trines, and A. Wagner, editors. *TESLA Technical Design Report, Part I Executive Summary*. DESY 2001-011, ECFA 2001-209, 2001.  
R.-D. Heuer, D. Miller, F. Richard, and P. Zerwas, editors. *TESLA Technical Design Report, Part III Physics at an  $e^+e^-$  Linear Collider*. DESY 2001-011, ECFA 2001-209, 2001.
- [5] Peter W. Higgs. Broken symmetries, massless particles and gauge fields. *Phys. Lett.*, 12(2):132–133, Sep 1964.  
Peter W. Higgs. Broken symmetries and the masses of gauge bosons. *Phys. Rev. Lett.*, 13(16):508–509, Oct 1964.
- [6] G. Abbiendi et al. Search for the Standard Model Higgs boson at LEP. *Phys. Lett. B*, 565:61–75, July 2003. <http://arxiv.org/hep-ex/0306033>.
- [7] The LEP Electroweak Working Group. Status of Winter 2007. <http://lepewwg.web.cern.ch/LEPEWWG/>.
- [8] Stephen P. Martin. A supersymmetry primer, 1997. <http://arXiv.org/hep-ph/9709356>.
- [9] Daniel Schulte. *Study of Electromagnetic and Hadronic Background in the Interaction Region of the TESLA Collider*. PhD thesis, Universität Hamburg, 1996.
- [10] E. v.Oelsen, C. Grah, W. Lohmann, and M. Ohlerich. Fast beam diagnostics with energy measurements in the forward calorimeters of the ILC detector. EUROTeV Memo 2006-011, 2006. <http://www.eurotev.org/>.

- [11] Pisin Chen. Beamstrahlung and the QED, QCD backgrounds in linear colliders. SLAC-PUB-5914, Sep 1992. Presented at 9th International Workshop on Photon-Photon Collisions (PHOTON-PHOTON '92), San Diego, CA, Mar 1992.
- [12] Tor Raubenheimer. Suggested ILC beam parameter range, Feb 2005. Available on <http://www-project.slac.stanford.edu/ilc/acceldev/beampar/SuggestedILCBeamParameterSpace.pdf>.
- [13] P. Chen and V. I. Telnov. Coherent pair creation in linear colliders. *Phys. Rev. Lett.*, 63(17):1796–1799, Oct 1989.
- [14] C. Rimbault, P. Bambade, K. Mönig, and D. Schulte. Incoherent pair generation in a beam-beam interaction simulation. *Phys. Rev. ST Accel. Beams*, 9:034402, 2006.
- [15] LDC Working Group. Detector Outline Document for the Large Detector Concept, July 2006. <http://www.ilcldc.org/documents/dod/>.
- [16] International Linear Collider Reference Design Report. ILC Report 2007-001, 2007. <http://ilcdoc.linearcollider.org/record/6321/files/>.
- [17] Adrian Vogel. The coordinate system for LDC detector studies. LC note DET-2005-009, Oct 2005. <http://www-flc.desy.de/lcnotes/>.  
Christian Grah. Coordinate system for the 20 mrad crossing angle case of the ILC. Internal DESY note, Oct 2005. <http://www-zeuthen.desy.de/ILC/fcal/>.
- [18] J. E. Brau, A. A. Arodzero, and D. M. Strom. Calorimetry for the NLC detector. *ECONF*, C960625:DET077, 1996. Also in *New Directions for High-energy Physics: Proceedings*, pages 437–441, Stanford 1997.  
J.-C. Brient and H. Videau. The calorimetry at the future e+ e- linear collider. *ECONF*, C010630:E3047, 2001. Also in *Proceedings of APS / DPF / DPB Summer Study on the Future of Particle Physics*, Snowmass, Colorado, 2001.  
Mark A. Thomson. Particle flow calorimetry at the ILC. In *Proceedings for the LCWS06*, Bangalore, Mar 2006. <http://arxiv.org/physics/0607261>.
- [19] P. Buzhan, B. Dolgoshein, et al. The advanced study of silicon photomultiplier. ICFA Instrumentation Bulletin, 2001. <http://www.slac.stanford.edu/pubs/icfa/fall101/paper3/paper3a.html>.  
P. Buzhan, B. Dolgoshein, et al. Silicon photomultiplier and its possible applications. *Nuclear Instruments and Methods in Physics Research A*, 504(1–3):48–52, May 2003.
- [20] H. Abramowicz, D. Drachenberg, W. Lohmann, et al. Instrumentation of the very forward region of a linear collider detector. *IEEE Transactions on Nuclear Science*, 51(6):2983–2989, Dec 2004.
- [21] Vladimir Drugakov. Private communication.

- [22] B. Parker and A. Seryi. Compensation of the effects of a detector solenoid on the vertical beam orbit in a linear collider. *Phys. Rev. ST Accel. Beams*, 8(4):041001, Apr 2005.
- [23] C. Grah and A. Saproinov. Fast luminosity measurement and beam parameter determination. EUROTeV Report 2007-006, 2007. <http://www.eurotev.org/>.
- [24] R. Brinkmann, K. Flöttmann, J. Rossbach, P. Schmüser, N. Walker, and H. Weise, editors. *TESLA Technical Design Report, Part II The Accelerator*. DESY 2001-011, ECFA 2001-209, 2001.
- [25] S. Agostinelli et al. [GEANT 4 Collaboration]. GEANT 4 — a simulation toolkit. *Nuclear Instruments and Methods in Physics Research A*, 506(3):250–303, July 2003. SLAC-PUB-9350.  
Geant 4 – A Toolkit for the Simulation of the Passage of Particles through Matter. <http://geant4.web.cern.ch/geant4/>.
- [26] Ekaterina Kuznetsova. *Design Studies and Sensor Tests for the Beam Calorimeter of the ILC Detector*. PhD thesis, Humboldt-Universität zu Berlin, 2006.
- [27] Christian Grah. Private communication.
- [28] C. Grah, R. Schmidt, et al. Polycrystalline CVD diamonds for the beam calorimeter of the ILC. In *Nuclear Science Symposium Conference Record*, volume 2, pages 721–724, San Diego, CA, USA, Oct 2006. IEEE.
- [29] MySQL AB. <http://www.mysql.com/>.
- [30] ROOT – An Object-Oriented Data Analysis Framework. <http://root.cern.ch/>.
- [31] Adrian Vogel. Private communication.



# Acknowledgements

At first place, I would like to thank Dr. Wolfgang Lohmann for the offer to work on this topic, for the guidance and the support that accompanied my work, and for the patience. I am deeply grateful to him for being a wonderful supervisor and mentor.

Many thanks are given to Prof. Dr. Jürgen Reif for the supervision from the side of the Brandenburgische Technische Universität Cottbus. This comprises the administrative support as well as the thorough perusal of this thesis.

I am also very thankful to Dr. Karsten Büßer for pointing to important topics and for reading this work very attentively.

In particular, I have to express my gratitude to Adrian Vogel, whose simulated event samples I was allowed to analyse for this work. I am very grateful to him, to Martin Ohlerich, to Dr. Christian Grah, to Dr. Ekaterina Kuznetsova, and to Dr. Andreas Schälicke for countless advices and support in physical, technical as well as organisational problems.

Them as well as the entire working groups—the LC group at DESY Zeuthen and the FLC group at DESY Hamburg—I would like to thank for a really convenient working atmosphere full of interest, sympathy and nonchalance.

Ich danke innigst meinen Eltern, die mir im weitesten Sinne das Physikstudium ermöglicht haben und mein Gemüt währenddessen immer ertrugen. Es war nie beabsichtigt, daß ich Euch so wenig an meinem Leben teilhaben ließ.

Bele und ihrer Familie möchte ich dafür danken, daß sie mich stets einbezogen und mich umsorgten, wenn ich selbst dies vergaß.

The most heartfelt gratitude is directed to Andrea, because nothing could have happened without this mental and creative power, the source of which is her.